High Order Numerical Models for High Amplitude Ultrasonic Wave Propagation

Jeffrey Leadbetter

Mechanical Engineering
McGill University, Montreal

October 2011

A thesis submitted to McGill University in partial fulfillment of the requirements of the degree of Masters in Engineering

Contents

List of Figures

List of Tables

Abstract

The application of high-order numerical modeling to nonlinear ultrasonic wave propagation in fluids is discussed. This work is motivated by ongoing developments with Wave Phase Conjugating (WPC) transducers, which are able to greatly amplify and re-emit incident acoustic energy back to a source location. As a result of the high amplification factors, conjugate wave magnitudes may exceed linear acoustic thresholds, leading to progressive nonlinear distortion and shock wave formation. In this work, a numerical model is formulated and coded for the simulation of the high amplitude nonlinear wave-fields produced by WPC transducers. At ultrasonic frequencies (> 1 MHz) wavelengths are short relative to propagation distances, making accurate numerical methods a requirement. The implemented numerical scheme uses high-order Weighted Essentially Non-Oscillatory (WENO) techniques. Novel analysis is presented on the WENO schemes' spectral accuracy and on their capability to model progressive wave distortion. Details on the integration of a WPC transducer model into the numerical framework are also provided. This combination of modeling capabilities offers a new advancement in the simulation of WPC transducers and the high amplitude sound fields they produce. Using a simplified one-dimensional representation, the numerical model is applied and preliminary results investigating the influence of nonlinear acoustic response in ultrasonic WPC are presented.

Résumé

L'application de schémas numériques d'ordre supérieur à la propagation d'ondes ultrasonores non-linéaires dans les fluides sera discutée. Cette recherche est motivée par les développements continus relatifs à de la conjugaison de phase acoustique, procédé qui permet d'amplifier et de renvoyer l'énergie acoustique incidente vers son lieu d'émission. Pour cette raison, les amplitudes des ondes conjuguées peuvent dépasser les seuils de validité de l'acoustique linéaire, conduisant à une distorsion non-linéaire progressive et à la formation d'ondes de choc. Dans ce travail, un modèle numérique a été élaboré et codé pour simuler les champs induits par des ondes non-linéaires issues d'une conjugaison de phase acoustique. A des fréquences ultrasonores (> 1 MHz) les longueurs d'ondes sont courtes devant la distance de propagation, ce qui rend nécessaire l'usage de méthodes numériques précises. La modélisation numérique implémentée dans cette recherche utilise une technique de schémas d'ordre supérieur intitulée: “Weighted Essentially Non-Oscillatory”. Les analyses faites sur la précision spectrale des schémas seront confrontées aux résultats des calculs de propagation d' ondes ultrasonores. Les détails de l'intégration du modèle de fluide non-linéaire avec celui d'un transducteur à conjugaison de phase acoustique seront présentés ainsi que les résultats préliminaires sur le comportement de la conjugaison de phase en milieu non linéaire.

Acknowledgements

Primary acknowledgment is given to thesis supervisors Prof. Evgeny Timofeev (McGill University) and Prof. David Frost (McGill University) for their guidance and contributions that have made this work possible. Acknowledgment is also given for the substantial assistance provided by Prof. Alain Merlen (University of Lille) throughout the course of this work. Additional acknowledgments are given to Prof. Andrew Higgins (McGill) for guidance during the preliminary stages of this work, and to Dr. Alireza Najafiyazdi (McGill) for several helpful discussions during the concluding months of this work. Financial support has been provided by Natural Science and Engineering Research Council of Canada (NSERC) through the Alexander Graham Bell Canada Graduate Scholarships (CGS) program. The French language abstract was prepared by Mr. Charles Brun and Ms. Laura Damecour. Finally, acknowledgment is given to Ms. Melissa Duffy, whose constant moral support has made it possible to overcome many challenges encountered during the preparation of this thesis.

1 Introduction

The development of the numerical model discussed in this thesis is primarily motivated by an emerging ultrasound imaging and measurement technique known as ultrasonic wave phase conjugation (WPC). Specifically, this work was conducted in collaboration with researchers, Merlen et al. [53], who are actively developing both physical WPC devices and numerical modeling capabilities. The primary attribute of ultrasonic WPC devices is their ability to greatly amplify and re-emit incident acoustic energy back to a source location [53]. This capability has the potential to improve aspects of conventional ultrasound imaging and microscopy [10], and has proposed applications for novel image generation methods [60]. Of particular interest is the development of ultrasonic WPC technology for use in diagnostic medical imaging.

The second topic considered in this thesis is the modeling of high-amplitude acoustic phenomena, which is also referred to as nonlinear acoustic phenomena. In general, nonlinear effects in ultrasonic sound waves can result from high amplitude initial waves, strong beam focusing, or the accumulation of small distortions over long propagation distances. Due to the large amplification of waves produced by the ultrasonic WPC process, prominent nonlinear effects may occur in the conjugate sound beams [13]. In this context the current work seeks to develop a numerical model that can accurately represent the ultrasonic WPC process and the propagation of nonlinear waves. The objective of this effort is to further the numerical modeling capability available to ongoing ultrasonic WPC research and development.

The developed numerical model uses a finite volume formulation to solve fluid mass and momentum conservation equations. Weighted-Essentially-Non-Oscillatory (WENO) techniques [70] are employed in the numerical model, and the attributes of this numerical scheme are examined in detail. WENO techniques were selected based on their history of application to nonlinear fluid dynamic phenomena, including the propagation of shock waves. Alternative numerical techniques are also discussed in this thesis and recommendations are made for the

extension of the current model using more accurate, but more complex, hybrid numerical schemes. In this regard the detailed analysis provided for the implemented WENO techniques provides new insight into the numerical modeling nonlinear wave propagation, as many of the more advance schemes available include some aspects of a WENO formulation.

Considering specifically the application of nonlinear sound beams in ultrasonic WPC, the model developed in this thesis differs from previous works in two main respects. Representative of the first group, the previous works [51, 52, 53, 76] have numerically modeled the physical WPC process but have opted to apply only linear acoustic models to the fluid domain. Representative of the second group, the previous works [12, 13, 14, 22 59, 60] have accounted for acoustic nonlinearity in fluid domain by using the Khokhlov-Zabolotskaya-Kuznetsov (KZK) beam equation [30, 42, 80], but have not modeled the physical process of ultrasonic WPC. Instead these works have relied upon prior knowledge from physical experiments to determine the amplitude of conjugate sound fields. In general, the KZK equation is a well established and efficient tool for high amplitude acoustic beam simulation, but it has limitations on allowable beam dispersion and is unable to easily accommodate material inclusions in the path of propagating waves. In practice this means that KZK based numerical models cannot be readily applied to biomedical imaging problems, where the presence of different tissues can cause reflection of waves off the main beam axis, and where the tissue material properties vary throughout the domain. The numerical model developed in this thesis offers a framework that overcomes these limitations, which with can enhance the study of applied ultrasonic WPC.

In the remainder of this introductory chapter some additional background is provided to give context to the discussions that follow. In Section 1.1 the relevant principles of nonlinear acoustic phenomena in biomedical ultrasound are introduced. In Section 1.2 an analytical solution to nonlinear plane wave propagation is presented to further illustrate key principles and to provide a benchmark solution against which the numerical model is evaluated. In Section 1.3 and Section 1.4 ultrasonic WPC is further introduced to highlight the potential

applications that provide the motivation for this thesis work. Concluding this introductory chapter in Sections 1.5 and 1.6 are concise statements on the thesis objectives and known limitations. In Chapter 2 the governing physical equations for the linear and nonlinear acoustic model are detailed. In Chapter 3 a review of relevant numerical methods is provided and spectral analysis of the model is conducted to determine its accuracy limits for wave propagation. In Chapter 4 the numerical model is verified and applied to high-amplitude plane wave propagation to evaluate its potential for application to practical problems. The development and verification of the ultrasonic WPC model is discussed in Chapter 5. Discussed in Section 5.5 are novel calculation results that illustrate potential nonlinear acoustic influences in conjugate sound beams. Chapter 6 concludes the thesis with a summary of findings and recommendations for future work.

1.1 Nonlinear Acoustics in Biomedical Ultrasound

It is now well known that nonlinear effects occur in almost all applications of biomedical ultrasound. These applications can be categorized as either diagnostic ultrasound for medical imaging, or therapeutic applications that use high intensity ultrasound to stimulate tissue healing, perform ultrasonic surgery, or to destroy internal stones using a process known as lithotripsy [15, 20].

In the context of ultrasound imaging, nonlinear effects are a byproduct of the intended linear acoustic behavior. Ultrasonic imaging is a process where high frequency sound beam is emitted and the intensity of received reflections caused by changes in acoustic impedance ($z = \rho c$, where ρ is density and c is sound speed) is recorded. When the emitted sound beam is swept through a region, a map of the acoustic impedance distribution is produced. The resolution of the resulting image is closely related to the emitted wavelength, thus higher frequencies have the potential to provide higher resolution images. For example, a 10 MHz wave in water has a wave length of 0.15 mm, and this is the best resolution that can be obtained in the resulting image.

A prominent nonlinear effect in ultrasonic imaging is the progressive distortion of

the initial pressure wave profile. This type of distortion is caused by high amplitude effects in the propagating wave. When considering the frequency spectra of the propagating wave this distortion is evident as the addition of harmonic content. It is now well known that the harmonic content in the reflected sound-spectra can be used to improve the quality of ultrasonic images [23]. This result is a product of the shorter wavelength associated with the higher frequency harmonics. Additionally, including harmonic information in ultrasonic images provides benefits beyond the reduction in wavelength. An important feature of ultrasonic beams is the spatial pattern of sound beam intensity produced by the phase interference of waves originating from different locations on the ultrasonic transducer. Shown in Figure 1 is the acoustic beam pattern produced by a simple 2 cm diameter flat circular piston radiating 1 MHz ultrasound into water. The analytical expression used to produce Figure 1 is provided in [40]. This example illustrates appearance of a main lobe of acoustic intensity along the piston axis, along with a series of smaller side lobes. In biomedical imaging it is the energy in the main lobe that is used to form the image, while reflections produced by side lobes cause image artifacts. In practical devices, curved transducer surfaces or multi-element beam forming arrays can be used to reduce the magnitude of side lobes, but their effect is qualitatively similar.

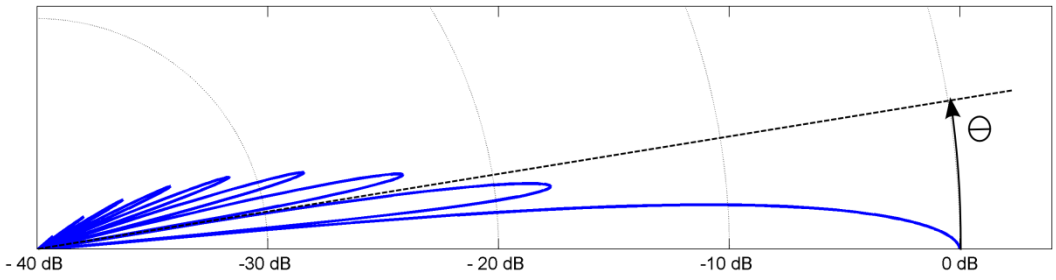

Figure 1: Beam function for a 2 cm cylinder radiating at 1 MHz into water. Solid line denotes relative intensity as a function of offset angle, θ, from the transducer axis.

When considering nonlinear effects for the beam shown in Figure 1 it can be stated that the main lobe, which features the highest intensity and a longest propagation path, produces a greater level of accumulated distortion than the side lobes. In practical devices with focused sound fields, nonlinear distortion and the

associated harmonics occur predominantly at the high intensity beam focus [23]. Elsewhere low levels of harmonic content are present, and the images produced from harmonics in the reflected pressure spectra have a corresponding reduction in side lobe artifacts. This phenomenon in conjunction with the shorter wavelengths of the harmonic frequencies allows for an overall increase in image quality. This improvement is well illustrated by a sample ultrasonic image of an in vivo human heart provided in [24] and reproduced here in Figure 2.

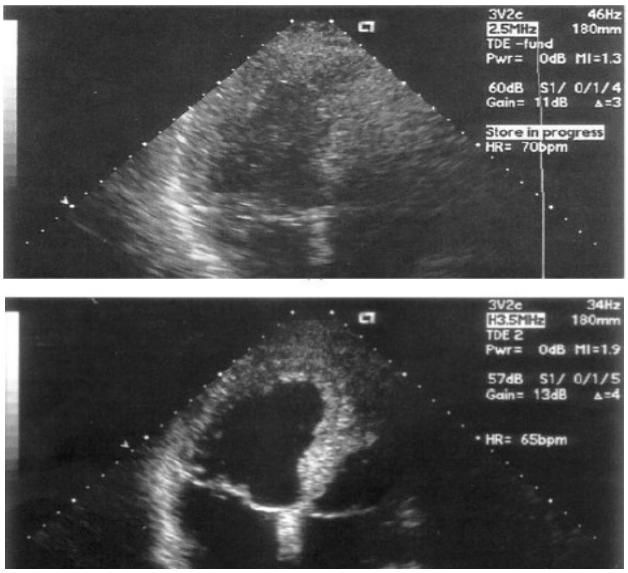

Figure 2: Conventional and harmonic images of a human heart. Upper frame shows conventional pulse ultrasound image, while the lower frame shows the image with second harmonic information included. Reproduced from [24].

Other applications of nonlinear acoustics effects in biomedical ultrasound are therapeutic in nature. At moderate beam intensities, tissue heating caused by acoustic dissipation at the beam focal location can help tissue healing [20]. When the beam intensity is of higher amplitude and applied for a sufficient duration, the localized heating can be used surgically to achieve cell death at the beam focal location [18, 37] which may for example, contain tumor tissue [38]. A third direct application of nonlinear acoustics in biomedical ultrasound is a process known as lithotripsy. This procedure uses highly focused acoustic pulses to form shock waves of up to 100 MPa peak pressure at the focal location [15]. When kidney stones or gall bladder stones are located at the focal point the impact of the shockwave (and subsequent rarefaction within the stone) leads to the

disintegration of the stone into pieces small enough to be evacuated naturally without the need for surgery [15].

The nonlinearity of a biological tissue is often quantified using the *B/A* parameter [7, 8]. Mathematical grounds for *B/A* stem from the Taylor series relating the acoustic values of perturbed pressure, p', to perturbed density, ρ':

$$p' = A\left(\frac{\rho'}{\rho_o}\right) + \frac{B}{2!}\left(\frac{\rho'}{\rho_o}\right)^2 + \frac{C}{3!}\left(\frac{\rho'}{\rho_o}\right)^3 + \cdots$$

$$A = \rho_o\left[\left(\frac{\partial p}{\partial \rho}\right)_s\right]_{\rho_o, s_o} = \rho_o c_o^2 \tag{1.1}$$

$$B = \rho_o^2\left[\left(\frac{\partial^2 p}{\partial \rho^2}\right)_s\right]_{\rho_o, s_o}$$

where a reference state is defined by a density value, ρ_o, and a constant entropy, $s = s_o$, and the coefficients A, B, and C are magnitudes for each term in the Taylor expansion. For the first order linear coefficient, A, the general definition for sound speed, $(\partial p/\partial \rho)_s = {c_o}^2$, can be used to show that, $A = \rho_o {c_o}^2$. The coefficients B and C apply to square and cubic terms in the expansion and represent nonlinearity in the fluid response. Values for A, B, and C can be determined experimentally using several techniques [8, 44, 64]. It is also possible to determine these values analytically when a suitable equation of state, such as the Tait-Kirkwood equation in Section 2.1, is known.

For the majority of problems in nonlinear acoustics the first two terms of this expansion are sufficient to represent the range of pressure perturbations encountered [8]. By factoring $A = \rho_o {c_o}^2$ from both terms in the truncated series the parameter *B/A* and its physical relevance become apparent:

$$p' = \rho' c_o^2\left[1 + \frac{1}{2}\frac{B}{A}\left(\frac{\rho'}{\rho_o}\right)\right] \tag{1.2}$$

This expression shows that the ratio *B/A* quantifies the relative influence of the first order linear acoustic response and the second order nonlinearity in the local

pressure perturbation for a given state, ρ' / ρ_o. Similarly, it can be shown that the parameter *B/A* quantifies the variation of local sound speed as a function of perturbed density according to [8]:

$$c = c_o \left[1 + \frac{1}{2} \frac{B}{A} \left(\frac{\rho'}{\rho_o} \right) \right] \tag{1.3}$$

In the context of biomedical ultrasound, the parameter *B/A* has particular significance as the range of values associated with different tissues is quite large. In general, fatty tissues have higher values of *B/A* than non-fatty tissues. Other factors include the tissues water content, cell to cell adhesive forces, and individual cellular structures [24]. Stemming from these principles, there now exists some research efforts on the use of *B/A* to characterize pathological changes in tissues [54]. As an illustrative example Table 1 compares the linear and nonlinear properties for water, liver tissue, and fat tissue.

Table 1: Comparison of nonlinear acoustic properties for biological tissues.

Material	***B/A***	Source
Water	5	[8]
Hemoglobin (20%)	6.5	[8]
Liver	7.6	[64]
Fat	9.9	[64]
Collagen	4.3	[8]

Motivated by this variation in tissue nonlinearity some techniques to produce images of *B/A* using conventional ultrasound technologies have been investigated. The most successful current approach uses two sound beams, one at lower frequency to modulate the compressed state of the tissue and a second higher frequency imaging beam. As further described in [24], the phase interaction between these two beams produces information that can be used to image *B/A*, although, as noted in [24], the resulting image quality is still relatively poor.

1.2 Analytical Solution to Nonlinear Plane Wave Propagation

To more quantitatively introduce nonlinear wave phenomena, the case of an initially sinusoidal plane wave with velocity amplitude of u_o and a fundamental angular frequency of ω is considered. For the simple wave propagation, the resulting behavior can be described as a progressive wave [4], governed by the nonlinear differential equation:

$$\frac{\partial u}{dt} + (c_o + \beta u)\frac{\partial u}{\partial x} = 0 \tag{1.4}$$

where u is the fluid velocity, t is the time variable, c_o is the fluid sound speed, β is the coefficient of nonlinearity, and x is the position variable. From characteristic analysis of the progressive wave equation it is known the wave apexes propagate with a velocity of approximately (c_o + βu_o), while the equilibrium points propagate with a velocity of c_o. At some position, $\bar{x}$, this progressive deformation results in the formation of an acoustic shock wave. In Figure 3 this progressive distortion is depicted along with associated characteristic wave speeds.

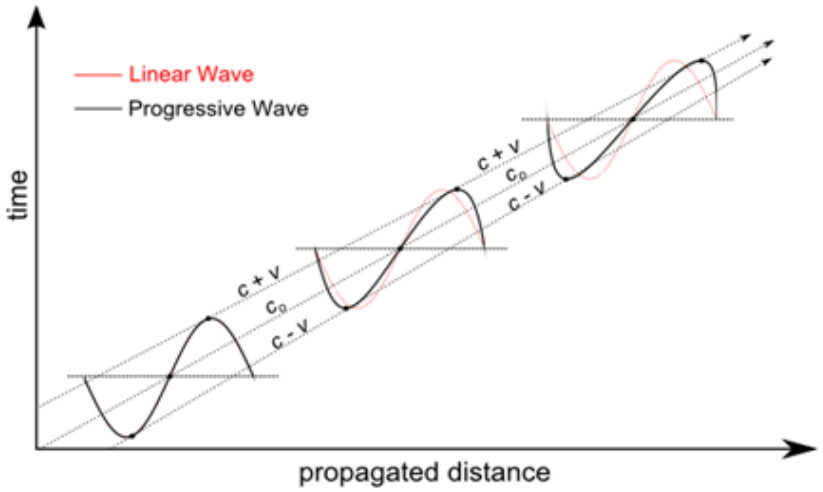

Figure 3: Distortion of a progressive wave.

Fourier analysis of the deformed wave reveals the presence of new spectral content with integer harmonics of the original frequency, ω. A classic solution to this harmonic profile is often termed the *Fay-Fubini solution* [3]. Details on this solution are given here to illustrate some relevant behavior of the progressive

wave, and to provide the analytical values used to evaluate the developed numerical model. For all regions of the domain, the wave solution is [25]:

$$\frac{u}{u_o} = \sum_{n=1}^{\infty} B_n(\sigma) \sin(n\omega\tau) \tag{1.5 a}$$

with:

$$\sigma = x/\bar{x}\,, \qquad \bar{x} = \frac{c_o^2}{u_o \omega \beta}\,, \qquad \tau = t - x/c \tag{1.5 b}$$

where n is the integer harmonic number, B_n is the amplitude coefficient for particular harmonic, and σ is the position variable normalized by the initial shock location. For brevity, only the simplified solutions for $B_n(\sigma)$ are provided here. For regions before the initial shock location ($\sigma < 1$) the harmonic profile is [25]:

$$B_n(\sigma) = \frac{2u_o}{n\sigma} J_n(n\sigma) \tag{1.6}$$

where J_n is the Bessel function of the first kind. For regions beyond the initial shock location ($\sigma \geq 1$) the solution becomes more complex as it must include an implicit expression for the shock amplitude, V_s. Including this consideration the harmonic profile becomes [25]:

$$B_n(\sigma) = \frac{2}{n\pi} V_s + \frac{2}{n\pi\sigma} \int_{\xi_{min}}^{\pi} \cos n(\xi - \sigma \sin \xi)\, d\xi \tag{1.7 a}$$

where:

$$V_s = \sin(\sigma V_s)\,, \qquad \xi_{min} = \sigma V_s \tag{1.7 b}$$

For $\sigma \gg 1$ the integral term becomes negligible and the expression simplifies to some degree. For intermediate regions the solution can be found by numerically evaluating the integral term. Examining both expressions for B_n it can be seen that the solution is self-similar for any particular value of σ. From this self-similarity it is evident that the coefficient of nonlinearity, β, has a direct influence on the rate of harmonic generation.

It is this influence of β on the harmonic generation rate that is of particular interest in the current study. For many applications of nonlinear acoustics it is more

conventional to specify nonlinear properties using the previously discussed parameter of nonlinearity, *B/A*. The coefficient β is related to the parameter *B/A* by [8]:

$$\beta = 1 + \frac{1}{2}\frac{B}{A} \tag{1.8}$$

As it has been established that different tissues possess different values of *B/A*, this dependence illustrates that the measured harmonic content in an ultrasonic wave can be used to infer information about the value of *B/A*. Referring to Section 1.1, it was discussed that the parameter *B/A* relates to tissue properties; therefore, measurements of harmonic content can indirectly provide additional information about tissue properties for biomedical diagnostic purposes.

1.3 Acoustic Wave Phase Conjugation

The development of ultrasonic WPC devices is of interest for two primary reasons: their ability to greatly amplify and re-emit incident wave energy, and their ability to retro-focus this energy as conjugate waves back to an initial source location according to the principles of time-reversed wave propagation [27]. In practice this effect is achieved using a cylindrical conjugating transducer that consists of a magnetostrictive material core wrapped in an electrical coil solenoid. Application of oscillating current to the solenoid results in oscillation of the internal magnetic field, which in turn produces a modulation of up to 4% in the materials bulk modulus and sound speed [52, 53]. When waves enter the magnetostrictive transducer, this modulation interacts with the stresses induced by the forward propagating wave to produce a backwards propagating conjugate wave. In general, conjugate waves are produced as a result of momentum conservation within the magnetostrictive transducer [52]. Furthermore, the production of conjugate waves is dependent on a resonant interaction where modulation in the transducer is double the frequency of the incident wave [52]. Importantly, the phase properties of the incident waves are maintained, thus the conjugate waves are able to propagate along their original path to the initial source location. In Chapter 5 this process is described in greater detail.

Practical ultrasonic WPC systems rely on both the magnetostrictive conjugator and a standard focusing ultrasound transducer to produce the incident wave pulse and to record the conjugate waves. Figure 4 shows a simplified schematic for an axially aligned focusing transducer and magnetostrictive conjugator, while Figure 5 shows experimental images of incident and conjugate beams produced from this configuration.

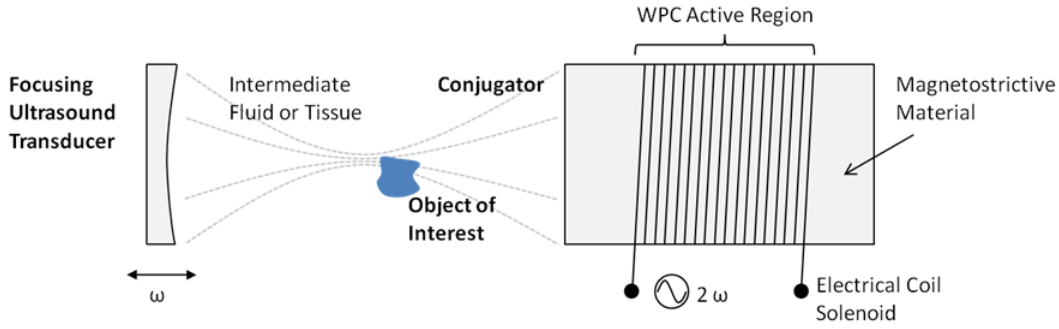

Figure 4: Schematic depiction of an acoustic WPC device.

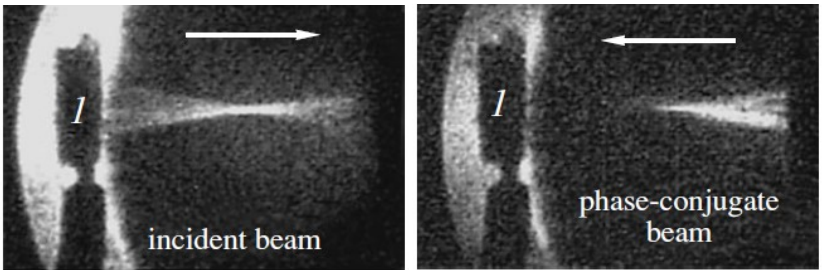

Figure 5: Experimental images of incident and conjugate ultrasound beams. Reproduced from [10].

Using this setup, WPC systems are readily applied to perform ultrasonic microscopy, where by shifting the focus of the incident beam relative to an object of interest, the intensity of received conjugate beam is used to produce an image [10]. By using a WPC system the image quality is improved by the conjugate waves ability to compensate for wave front distortions produced by inhomogeneities in the intermediate material [11, 13, 41, 59, 61].

Two important distinctions exist between magnetostrictive WPC and the more general acoustic time reversal mirror (TRM) principles described in [27]. First, magnetostrictive WPC devices produce conjugate beams that are amplified by up

to 80 dB [13], while acoustic TRM generally produces an equal amplitude conjugate beam. Secondly, magnetostrictive WPC devices are highly frequency selective [41], while acoustic TRM is used to produce broadband conjugate waveforms [22]. As will be further discussed in Chapter 5, these attributes of magnetostrictive WPC are a result of the physical amplification process within the conjugator.

1.4 Nonlinearity in Conjugate Sound Fields

Due to the large amplifications achieved by magnetostrictive conjugators it is fully possible to produce conjugate sound beams with sufficient magnitude for nonlinear effects to occur, including the formation of shockwaves in the conjugate beam. The consideration of nonlinear effects in conjugate beams falls into two general categories: applications where the incident beam is essentially a linear acoustic beam, and applications where the incident beam is strong enough to contain nonlinear harmonics.

The first scenario of a relatively low amplitude and linear acoustic incident beam is primarily related to applications in acoustic microscopy [10]. As previously discussed in Section 1.3, in this application the primary benefit of ultrasonic WPC is the ability to compensate for wave front distortion caused by inhomogeneities of the linear acoustic parameters in the analysis domain [11, 13, 41, 59, 61]. As discussed in Section 1.1, it is well known from conventional ultrasound imaging that the inclusion of second harmonic information can improve image resolution by providing a narrower focal region and by reducing side lobes. There is now evidence to demonstrate that the harmonics generated in conjugate beams are phase coherent with the fundamental frequency, thus providing the benefit of wave front distortion compensation in addition to narrower focal resolution [13]. Some questions remain about imaging resolution at amplifications sufficient to form shock waves in the conjugate beam. In this case the acoustic beam is no longer lossless and the principles of time-reversed acoustics are violated [73]. However, some experimental and numerical work has shown that even in the presence of acoustic shocks the conjugate beam adequately reproduces the focal

properties of an initial beam [22]. It was found that the greatest limitation to the focal properties of acoustic WPC is not nonlinear irreversibility, but beam diffraction effects related to the aperture of the conjugator [22].

The second category of acoustic WPC applications involves incident beams of sufficient amplitude to generate harmonic content. Under these circumstances there are potential extensions of acoustic microscopy capabilities, and emerging applications in imaging the nonlinear parameter, *B/A*, through the analysis domain. With regard to microscopy, nonlinearity in the incident beam can be exploited by conjugating with the second (or higher) harmonic [12]. The motivation for this approach is the improved lateral resolution offered by the second harmonic in the incident beam. For homogeneous domains analytical and experimental works have shown that the conjugation of the second harmonic reproduces the focal qualities of the incident beam due to the coherent phase relation between the fundamental frequency and harmonics in the incident beam [12]. Furthermore, in homogeneous domains it has been found that this approach produces conjugate beams with better focal properties compared to the beams produced by conjugating at the fundamental frequency [14]. However, current results in applied microscopy do not report similar improvements in image quality, particularly when wave front distortion occurs in the incident beam [12]. In these circumstances the ability of the conjugate beam to account for phase aberration appears to be reduced, and images of similar or better quality may be obtained by conjugating the fundamental frequency and performing analysis on the received second harmonic.

As discussed in Section 1.1, imaging of the nonlinear parameter *B/A* has the potential to identify pathological changes to tissues that may not be apparent in the linear acoustic properties [59]. This is still a relatively unsuccessful technique when using conventional ultrasound technologies [23], and the use of WPC systems may offers a viable alternative [60]. Consider the co-axial arrangement shown in Figure 4, where now the inclusion has similar linear acoustic properties but a different *B/A* parameter. In this configuration, the amount harmonic content incident on the magnetostrictive transducer changes when the focus of the initial

beam is coincident with the *B/A* inclusion. *B/A* images are produced by conjugating the second harmonic of the incident beams and by recording the magnitude of the conjugate beams for different focal locations. Theoretical analysis conducted in [60] using a technique known as *nonlinear geometrical acoustics* has shown that the amplitude of the conjugate beam varies on the same order as changes in the nonlinear parameter at the beam focus. Importantly, this result remains valid even when the size of the inclusion is small relative to the total beam path length. Furthermore, if the harmonic content of the conjugate beam is analyzed as well then this effect is substantially more pronounced.

1.5 Thesis Objectives

Considering the information presented in Sections 1.1 through 1.4, it becomes evident that there is substantial potential for the application of WPC systems in ultrasonic imaging and biomedical diagnostics. As previously stated, the general objective of the current work is to develop a numerical model that can accurately represent the physical WPC process as described in Merlen et al. [53], and that can model the propagation of nonlinear waves including shockwave formation. This objective has been selected with the intention to further the numerical modeling capability available to ongoing ultrasonic WPC research and development.

More specifically, the model development has been guided by several practical requirements. The models governing equation set must be suitable for nonlinear wave propagation in fluids and should be consistent with established principles in the field of nonlinear acoustics. The model may assume that wave strengths are relatively low (fluid velocity is small compared to sound speed), but the physical equations should accurately represent the propagation of acoustic shocks. Finally, the governing equation set should be compatible with the WPC model developed by Merlen et al. [53] so that it can be included without substantial modification.

There are additional guiding requirements in regard to the numerical aspects of the developed model. The selected numerical scheme should be known for attributes of low numerical error and for the stable representation of solution

discontinuities such as shock waves. Additionally, the numerical formulation should be capable of representing inhomogeneous domains, where the variation may occur in the linear or nonlinear properties of the material. By meeting these requirements the developed model offers a novel combination of capabilities that can be used to study applied ultrasonic WPC in more detail than was previously possible.

In addition to the development work conducted for this thesis, several objectives were also set for practical findings. First, the developed model should be verified against analytical benchmarks so that additional results can be interpreted with confidence. Second, analysis and calculation results should be presented to quantify the accuracy of the developed numerical model and to make recommendations on the resolution required to represent ultrasonic WPC. Third, calculation results from the model should be used to quantify the influence of fluid nonlinearity on the amplification rates in magnetostrictive WPC transducers.

1.6 Known Limitations

In the current work there are two substantial effects which are not considered. The first of these is the dissipation or attenuation of sound beams by viscous losses and relaxation process. In the current work it has been assumed that these effects can be neglected. In general this assumption is not valid for biomedical ultrasound, and the exclusion is based largely on the complexity and challenges in numerical modeling of these dissipative process. For a simple approximation of attenuation many acoustic models use a thermoviscous dissipative term that is similar to the Navier-Stokes equations. This approach produces acoustic attenuation that increases with frequency squared, ω^2. Many biological tissues exhibit a frequency dependence that is better described by ω^b, where $(1 < b < 2)$ [15, 45]. Therefore, if simple thermoviscous attenuation is applied to nonlinear waves in biological tissues, the absorption of higher harmonics is over predicted and the overall quality of the solution is degraded. Three techniques that overcome this limitation are empirically based multiple-relaxation models [19], time domain convolution to produce ω^b attenuation dependence for any vale of b

[45], and the use of fractional derivates in the governing equations [56]. These three approaches are not trivial to implement into a numerical model, so they are beyond the scope of this thesis.

Despite this limitation, for sufficient beam strength or for a weakly attenuating tissue, the lossless assumption is entirely valid and the developed model can be safely applied. The balance between nonlinear wave steepening and dissipation is given by the Gol'dberg number [4]:

$$\Gamma = \frac{\omega p_o \beta}{\rho_o c_o^3 \alpha_\omega} \tag{1.9}$$

where p_o is the initial pressure amplitude, and α_ω is the attenuation coefficient at angular frequency ω. For $\Gamma \gg 1$ nonlinear wave steepening dominates and attenuating process can be safely neglected. Importantly, as Γ is directly proportional to wave amplitude, the lossless assumption becomes more valid for increasing wave amplitudes. Considering that high amplitude conjugate waves are of primary interest in this thesis, the assumption of a non-attenuating fluid model is well justified.

The second effect not included in the model is that of acoustic cavitation; however, some brief discussion on the topic is given here to aid with interpretation of certain numerical results. The analysis contained within this thesis typically considers fluid pressures in the range of 1 to 5 MPa, but in one instance reports results with pressure up to 80 MPa to illustrate a particular numerical phenomena. At these extreme pressures fluid cavitation during the negative phase of propagating waves is a strong possibility. Referring to [34], the limit to negative acoustic pressure sustained by purified degassed water is in the range of 20 MPa to 25 MPa. In practical applications this threshold is rarely realized as fluids or biological tissues are likely to contain small scale heterogeneities around which cavitation bubbles can form. Under these circumstances analysis of cavitation threshold is highly material dependent, making generalizations challenging. For one example, the experimental work in [2] generally observed cavitation from pulsed ultrasound in the realm of 1.5 MPa,

with some variation depending on the pulse duration. With conventionally focused ultrasound beams negative phase pressures are regularly reported in the range of 4 MPa [14, 15]. In the context of acoustic WPC, focal pressure amplitudes of 8 MPa have been reported [14] without mentioning cavitation effects. Based on this finding the value of 8 MPa was considered as the threshold to safely assume a fluid response free of cavitation effects in the current work.

2 Governing Equations for Nonlinear Acoustic Waves in Fluids

The governing equations used in this thesis are based on well established methods in linear and nonlinear acoustics. As the development of linear acoustic equations is quite simple and extremely well known, the discussion in this section is focused on giving context to the nonlinear governing equations. Historically, many equations have been developed for the representation of nonlinear acoustic wave propagation, where the term *nonlinear* encompasses both high amplitude and dissipative effects. Almost universally, the study of nonlinear acoustics has been conducted using second order wave equations, where the distinction *second order* is the result of applying a second order pressure density relation similar to Equation (1.2) given in Section 1.1. A general second order wave equation is given in [30], and well known form of this is the Kuznetsov equation [26, 42]. As summarized in [72], well known simplifications these general second order wave equations are the Westervelt equation [30, 72], Burgers' equation [26], and the Khokhlov-Zabolotskaya-Kuznetsov (KZK) equation [30, 42, 80] previously discussed in Chapter 1.

The governing equation set used in this thesis differs from the more widely known second order wave equations in several important regards. Most fundamentally, second order wave equations typically solve for a single unknown variable, such a pressure or acoustic potential, and are expressed using a single second order differential equation. As detailed in Section 2.1, the equations used in this thesis solve for perturbed density, ρ', and fluid velocity, $\vec{v}$, in a system of first order differential equations. This approach allows for relatively straight forward integration of additional physics such as the ultrasonic WPC model described in Chapter 5. Furthermore, this approach lends itself well to the use of shockwave capturing numerical methods needed for the simulation of highly distorted ultrasound wave fields. The second important distinction between the equations sets is that most second order wave equations are based on the Navier-Stokes equations to include the thermoviscous dissipative terms, while the equations presented in this thesis are based on the inviscid Euler equations.

An equation set available in the literature that most closely matches those presented here is the *full wave* model described in [29]. Comparing the equations used in [29] and in this thesis there are several minor differences, but the formulations are fundamentally similar.

2.1 Conservations Laws for Weakly Nonlinear Waves

The governing equation set is derived from the inviscid Euler equations, excluding the energy equation as an isentropic and irrotational wave field is assumed. Justification for the use of an inviscid equation set is discussed in Section 1.6. Additionally, for the modeling of wave propagation in an initially static medium, such as biological tissues, there is no physical basis to include rotational fluid effects.

In general, the linearization of the Euler equations to obtain an acoustic equation set in perturbed state variables is a well known procedure. For the nonlinear acoustic equations used in this work the reduction to acoustic variables is conducted in a similar manner; however, instead of linear approximations a second order Taylor expansion for the perturbed state values are used. In general, this approach is valid under the assumptions that ρ'/ρo $\ll$ 1 and $|\vec{v}|/c_o \ll 1$, which qualifies the wave as being weakly nonlinear. In an integral conservative form the governing equations for a control volume, *V*, bounded by surface, *S*, with normal vector, $\vec{n}$, are:

$$\frac{\partial}{\partial t}\oint_V \boldsymbol{U} dV = -\oint_S \boldsymbol{F} dS \tag{2.1 a}$$

$$\boldsymbol{U} = \begin{bmatrix} \rho' \\ v_x \\ v_y \end{bmatrix} \tag{2.1 b}$$

$$\boldsymbol{F} = \begin{bmatrix} \rho_o \vec{v} \cdot \vec{n} \\ c_o^2 \left(\frac{\rho'}{\rho_o}\right) n_x \\ c_o^2 \left(\frac{\rho'}{\rho_o}\right) n_y \end{bmatrix}_{linear} \tag{2.1 c}$$

$$\boldsymbol{F} = \begin{bmatrix} (\rho_o + \rho')\vec{v} \cdot \vec{n} \\ \left(\frac{1}{2}(v_x^2+v_y^2)+c_o^2\left(\frac{\rho'}{\rho_o}\right)+c_o^2\frac{(\gamma-2)}{2}\left(\frac{\rho'}{\rho_o}\right)^2\right)n_x \\ \left(\frac{1}{2}(v_x^2+v_y^2)+c_o^2\left(\frac{\rho'}{\rho_o}\right)+c_o^2\frac{(\gamma-2)}{2}\left(\frac{\rho'}{\rho_o}\right)^2\right)n_x \end{bmatrix}_{nonlinear} \tag{2.1 d}$$

where $\boldsymbol{U}$ is the conservative solution vector, $\boldsymbol{F}$ is the flux vector, $\rho = \rho_o + \rho'$ is fluid density defined in terms of an ambient (ρ_o) and perturbed (ρ') component, $\vec{v}$ is the velocity vector with subscripts x and y denoting Cartesian components, c_o is the ambient sound-speed. When using the linear flux vector (designated by the subscript *linear*) the governing equations are equivalent to the linear acoustic equations. When using the nonlinear flux vector (designated by the subscript *nonlinear*) the state perturbation values to the order of $O(\rho'^2)$ are retained allowing for applications to weakly nonlinear wave problems. For additional reference the derivation used to produce Equation (2.1) is carried out in full in Appendix A.

To accomplish the closed form of the nonlinear equations the Tait-Kirkwood EOS is was used in the system derivation. The exact EOS expression is given by Equation (2.2 a), while the $O(\rho'^2)$ representation used by the nonlinear system is given by Equation (2.2 b):

$$\frac{p + D}{p_o + D} = \left(\frac{\rho}{\rho_o}\right)^{\gamma} \tag{2.2 a}$$

$$P' = \rho_o c_o^2 \left(\frac{\rho'}{\rho_o}\right) + \rho_o c_o^2 \left(\frac{\gamma - 1}{2}\right)\left(\frac{\rho'}{\rho_o}\right)^2 \tag{2.2 b}$$

where p_o is a reference pressure and D is a material coefficient related to c_o and ρ_o. From the Tait-Kirkwood EOS the power coefficient, γ, in Equation (2.1) is related to the parameter B/A commonly used in nonlinear acoustics according to [8]:

$$\frac{B}{A} = \gamma - 1 \tag{2.3}$$

To further quantify the applicability of this equation set it is useful to consider the range validity inferred by the *weakly nonlinear* wave assumption. In [17] it was

found that second order wave equations tend to over predict the rate of wave distortion when used with inappropriately high Mach number waves, $M = |\vec{v}|/c_o$. Fortunately, for all wave amplitudes of practical significance to this thesis the weakly nonlinear assumption is valid. In the discussions of [50] and [78], it is suggested that the Kuznetsov equation is valid for $M < 0.1$. Based on the similar properties of second order waves equations and the equations used in this thesis some preliminary conclusions can be drawn. First, in Section 1.6 on cavitation thresholds it was noted that 25 MPa is the upper bound of permissible wave amplitudes. Using the linear acoustic impedance of water as a rough estimate this pressure corresponds to only $M = 0.01$. When considering applications such as medical Lithroscopy peak positive pressures up to 100 MPa are also possible [15]. Once again, from the linear acoustic impedance of water this pressure corresponds to $M = 0.04$, for which second order wave equations can be safely applied.

2.1.1 System Flux Jacobian

As will be show in Chapter 3, high order evaluation of spatial operators in the governing equations requires a transformation of the governing equations into a characteristic form. As the first step in this procedure the flux Jacobian matrices $\boldsymbol{A}$, are needed; the general forms of the linear and nonlinear Jacobians are as follows:

$$A_{i,j} = \frac{\partial F_i}{\partial U_j} \tag{2.4 a}$$

$$\boldsymbol{A} = \begin{bmatrix} 0 & \rho_o n_x & \rho_o n_y \\ \frac{c_o^2}{\rho_o} n_x & 0 & 0 \\ \frac{c_o^2}{\rho_o} n_y & 0 & 0 \end{bmatrix}_{linear} \tag{2.4 b}$$

$$\boldsymbol{A} = \begin{bmatrix} \vec{v}\cdot\vec{n} & (\rho_o+\rho')n_x & (\rho_o+\rho')n_y \\ \frac{c_o^2}{\rho_o}\left(1+(\gamma-2)\frac{\rho'}{\rho_o}\right)n_x & v_x n_x & v_y n_x \\ \frac{c_o^2}{\rho_o}\left(1+(\gamma-2)\frac{\rho'}{\rho_o}\right)n_y & v_x n_y & v_y n_y \end{bmatrix}_{nonlinear} \quad (2.4\text{ c})$$

As the decomposition to characteristic variables will always be for a specified normal direction, a simpler representation of the Jacobians can be used, where $n_x = 1$ and $n_y = 0$, is assumed. The simplified Jacobians are as follows:

$$\boldsymbol{A_x} = \begin{bmatrix} 0 & \rho_o & 0 \\ \frac{c_o^2}{\rho_o} & 0 & 0 \\ 0 & 0 & 0 \end{bmatrix}_{linear} \quad (2.5\text{ a})$$

$$\boldsymbol{A_x} = \begin{bmatrix} v_x & \rho_o+\rho' & 0 \\ \frac{c_o^2}{\rho_o}\left(1+(\gamma-2)\frac{\rho'}{\rho_o}\right) & v_x & v_y \\ 0 & 0 & 0 \end{bmatrix}_{nonlinear} \quad (2.5\text{ b})$$

To apply these simplified relations to other normal orientations the fluid state must first be translated to a local coordinate system, (ρ', v_η, v_ϵ), where $n_\eta = 1$ and $n_\epsilon = 0$.

2.1.2 System Eigenvalues

It is well known that the eigenvalues of the flux Jacobian are representative of physical wave speeds for the linear and nonlinear governing equations [43]. As this analysis is conducted using the simplified Jacobian, $\boldsymbol{A_x}$, the resulting waves speeds are for the *x*-axially aligned normal direction. From the characteristic equation, $|\boldsymbol{A_x} - \lambda\boldsymbol{I}| = 0$, the eigenvalues are:

<u>*Linear System*</u>: $\lambda^- = -c_o\,, \qquad \lambda^+ = c_o, \qquad \lambda^0 = 0 \qquad (2.6\text{ a})$

<u>*Nonlinear System*</u>: $\lambda^- = v_x - c^*, \qquad \lambda^+ = v_x + c^*, \qquad \lambda^0 = 0 \qquad (2.6\text{ b})$

$$c^* = c_o\sqrt{1+(\gamma-1)\frac{\rho'}{\rho_o}+(\gamma-2)\left(\frac{\rho'}{\rho_o}\right)^2} \quad (2.6\text{ c})$$

For both the linear and nonlinear systems, the wave speed λ^0 is a product of the two-dimensional system. It indicates that the associated characteristic variable,

which is simply transverse velocity, v_y, is not propagated by wave motion. When a one-dimension system is considered only the two wave speeds, $\lambda = \pm c_o$, or $\lambda = v_x \pm c^*$, are present.

2.1.3 System Eigenvectors

To transform the governing equations to characteristic form the operation $\boldsymbol{\alpha} = \boldsymbol{LU}$ is applied, where the aggregate left eigenvector matrix, $\boldsymbol{L}$, is determined from the flux Jacobian according to:

$$\boldsymbol{l_i A_x} = \lambda_i \boldsymbol{l_i}$$

$$\boldsymbol{L} = \begin{bmatrix} \boldsymbol{l}_{\lambda^-} \\ \boldsymbol{l}_{\lambda^+} \\ \boldsymbol{l}_{\lambda^0} \end{bmatrix} \tag{2.7 a}$$

and the resulting eigenvectors are:

$$\boldsymbol{L} = \frac{1}{2} \begin{bmatrix} 1 & -\dfrac{\rho_o}{c_o} & 0 \\ 1 & \dfrac{\rho_o}{c_o} & 0 \\ 0 & 0 & 1 \end{bmatrix}_{linear} \tag{2.7 b}$$

$$\boldsymbol{L} = \frac{1}{2} \begin{bmatrix} 1 & -\dfrac{\rho' + \rho_o}{c^*} & \dfrac{(\rho_o + \rho')v_y^2}{(c^* - v_x)c^*} \\ 1 & \dfrac{\rho' + \rho_o}{c^*} & \dfrac{(\rho_o + \rho')v_y^2}{(c^* + v_x)c^*} \\ 0 & 0 & 1 \end{bmatrix}_{nonlinear} \tag{2.7 c}$$

To transform the reconstructed solution back to state variables, the operation $\boldsymbol{U} = \boldsymbol{R\alpha}$ is applied, which requires a set of corresponding right eigenvectors, $\boldsymbol{R} = \boldsymbol{L}^{-1}$. These were obtained analytically using Gaussian inversion of the left eigenvectors, with the end result being:

$$\boldsymbol{R} = \begin{bmatrix} \boldsymbol{r}_{\lambda^-} \\ \boldsymbol{r}_{\lambda^+} \\ \boldsymbol{r}_{\lambda^0} \end{bmatrix}^T \tag{2.8 a}$$

$$\boldsymbol{R} = \begin{bmatrix} 1 & 1 & 0 \\ -\frac{c_o}{\rho_o} & \frac{c_o}{\rho_o} & 0 \\ 0 & 0 & 2 \end{bmatrix}_{linear} \tag{2.8 b}$$

$$\boldsymbol{R} = \begin{bmatrix} 1 & 1 & -2\frac{(\rho_o + \rho')v_y}{c^{*2} - v_x^2} \\ \frac{-c^*}{\rho_o + \rho'} & \frac{c^*}{\rho_o + \rho'} & 2\frac{(\rho_o + \rho')v_y}{c^{*2} - v_x^2} \\ 0 & 0 & 2 \end{bmatrix}_{nonlinear} \tag{2.8 c}$$

2.1.4 Simplification to One-Dimensional System

To maintain generality for future development of the numerical model, the preceding governing equations were presented for domains with two spatial dimensions. In the present work only calculations in one spatial dimension are performed and the equation set can be reduced. When simplifying to a one-dimensional system, v_y can be neglected, the system eigenvalues no longer include λ^0, and the third column and row can be eliminated from each of the flux Jacobian and aggregate eigenvector matrices. For completeness these equations are included in Appendix B.

3 Development of the Numerical Model

The numerical methods used to evaluate the governing equations given in the preceding section are implemented using a reconstruction-evolution finite volume framework. This method is applied to solve the integral form conservation laws given in Equation (2.1). In the developed one-dimensional numerical model nodes are identified by index, i, while faces are identified by indices of, $i \pm ½$. This spatial discretization is depicted in Figure 6.

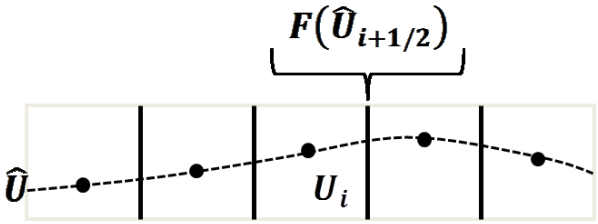

Figure 6: Schematic of one-dimensional finite volume discretization. Discrete points represent cell averaged values, dashed lines represent the true continuous values.

At each stage of the solution continuous state values, $\hat{\boldsymbol{U}}$, are reconstructed and calculated at cell faces from the cell average node values. Numerical fluxes are evaluated at each face from the reconstructed face values. The fluxes are summed for each cell to give a discrete value of the flux surface integral in Equation (2.1). Using these discrete values the solution can be evolved using a variety of time-discretization algorithms. This general technique is well known in computational fluid dynamics and is often termed as a Godunov-type method [43]. A simple first order, one-dimensional implementation of this method is as follows:

$$\boldsymbol{U}^{n+1} = \boldsymbol{U}^n + \Delta t \boldsymbol{L}^n \tag{3.1}$$

$$\boldsymbol{L} = \frac{1}{\Delta x}\left(\hat{\boldsymbol{F}}_{\boldsymbol{i+1/2}} - \hat{\boldsymbol{F}}_{\boldsymbol{i-1/2}}\right) \tag{3.2}$$

$$\hat{\boldsymbol{F}}_{i+1/2} = \boldsymbol{F}\left(\boldsymbol{U}^-_{i+1/2}, \boldsymbol{U}^+_{i+1/2}\right) \tag{3.3}$$

where $\hat{\boldsymbol{F}}$ is the numerical flux that is a function of $\boldsymbol{U}^+$ and $\boldsymbol{U}^-$, which are the reconstructed state values at each side of face, $i + ½$. To accurately compute wave propagation over hundreds of wave-lengths both high-order spatial reconstruction

and high-order time integration are required. When insufficiently accurate methods are used computed solutions can contain excessive dissipative and dispersive error. Dissipative error leads to the attenuation of propagating waves. Dispersive error is a frequency dependent change in wave velocity that can lead to unphysical distortions in multi-frequency waveforms.

In the following sections three aspects of the numerical method are discussed in detail: the high-order spatial reconstruction of state values to cell faces, the evaluations of fluxes from reconstructed the values, and the high-order time discretization algorithm.

3.1 Spatial Reconstruction

Spatial reconstruction of the solution from cell averages is accomplished using piecewise-polynomials. For each in the computational domain a polynomial fit is determined from the cell average values and from the average values of several neighboring cells. By increasing the number of neighbor cells included in the polynomial fit, the order of the polynomial increases and more accurate reconstructions can be obtained. However, a well-known limitation of high-order polynomial reconstruction is the Gibbs phenomena [43], which is the appearance of non-physical oscillations in the numerical solution near a discontinuity. To accommodate the need for high order reconstruction polynomials while also allowing for the oscillation-free representation of discontinuous acoustic shocks, the developed numerical model uses a Weighted Essentially Non-oscillatory (WENO) reconstruction technique [70]. WENO techniques were selected based on their established history of application to nonlinear fluid flows. In this section some historical developments of WENO methods are presented and the particular implementation is discussed in detail. At the conclusion of this chapter there is additional discussion on alternative methods, justifications for the implemented WENO scheme, and recommendations for future work.

3.1.1 Introduction to Essentially Non-Oscillatory Methods

To concisely illustrate Gibb's phenomena, Figure 7 plots a 6th order polynomial fit to data in a reconstruction stencil that includes a discrete jump in value, but is otherwise smooth. In Figure 7 the *Reconstruction Region* represents a single computational cell, while the other points used in the polynomial fit represent neighboring cells.

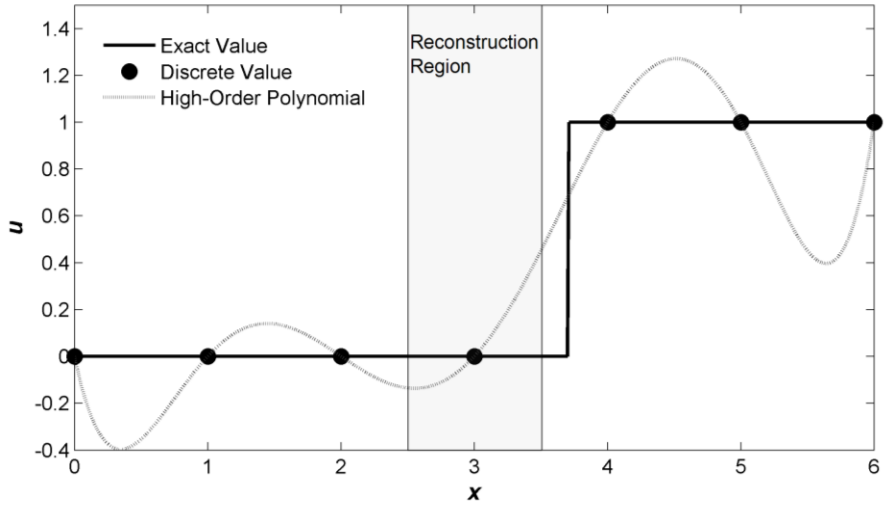

Figure 7: Spatial oscillations in a high order reconstruction polynomial.

As can be seen in Figure 7, the resulting polynomial contains spatial oscillations; when incorporated into a finite volume scheme this reconstruction produces similar oscillations in the computed solution. To overcome the problem of Gibb's phenomena a class of techniques referred to as *Essentially Non Oscillatory (ENO)* ones were established by Harten et al. [32] and subsequently underwent significant developments by Shu and Osher [69, 71]. The fundamental principle of ENO reconstructions is the selective use of several lower-order candidate polynomials contained within the original high-order stencil. Considering Figure 8, which contains the same data and total stencil size as Figure 7, it can be seen that several lower-order polynomials can be placed within the original higher-order stencil. By choosing a lower-order candidate that does not include the discontinuity (Candidate 1 in Figure 8) the resulting reconstruction would be free of oscillations.

As a result of choosing just once candidate stencil, the maximum order of the spatial reconstruction scheme is limited to $O(\Delta x^r)$, where r is the number of cells in a candidate polynomial ($r = 4$ in Figure 8). In smooth regions, where there is no need to exclude cells from the reconstruction polynomial, this solution is not ideal as there are $2r$-1 points within the total stencil that can be used to produce a $O(\Delta x^{2r-1})$ spatial reconstruction.

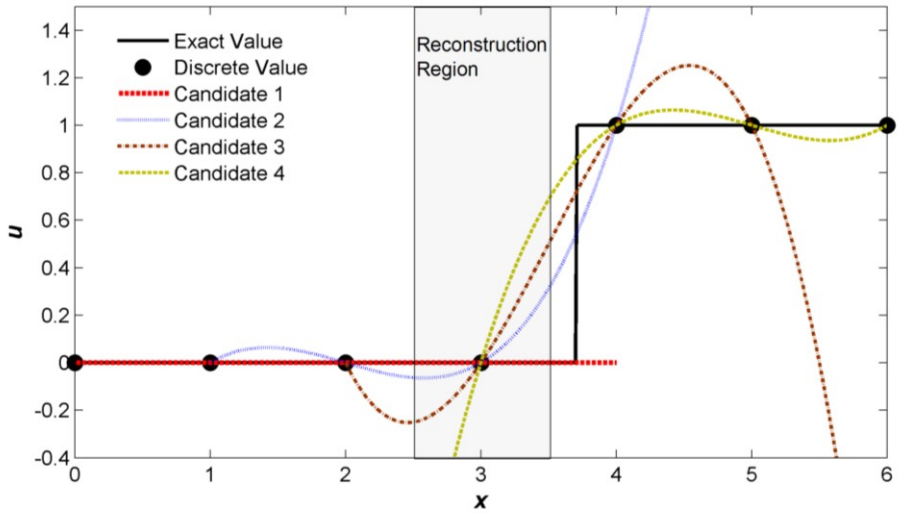

Figure 8: Candidate stencil reconstruction polynomials.

To address this limitation the Weighted Essentially Non Oscillatory (WENO) reconstruction technique was introduced by Liu et al. [48]. The guiding principle of WENO reconstruction is to combine all candidate stencils in such a way that each stencil is weighted according to a smoothness coefficient. This allows the contribution of non-smooth candidate stencils containing strong gradients or discontinuities to be minimized, thus reducing the incidence of non-physical numerical oscillations. At the same time, in smooth regions candidates can be weighted more ideally. This trait is the primary benefit of WENO reconstructions, as it allows for a higher order of accuracy throughout most of the domain.

The seminal work by Liu et al. [48] applied WENO reconstructions to scalar equations and to characteristic variables in systems of equations using a finite volume framework. After this work a substantial development was made by Jiang

and Shu [36] who applied WENO techniques in a conservative finite-difference framework. In their finite-difference approach, fluxes are first decomposed into upwind components at the cell nodes, and then the WENO reconstruction is applied to these flux values. For one dimensional models, such as the one developed in this work, differences between the finite-volume and finite-difference implementations of WENO methods are not substantial [70]. The differences become more substantial for multi-dimensional models. For multi-dimensional finite volume schemes the determination of the multi-dimensional polynomials and the evaluation of polynomial smoothness becomes complicated. In comparison, multi-dimensional finite-difference WENO schemes can evaluate each dimension independently at a much lower computational cost. The greatest limitation of the finite-difference WENO schemes is the requirement for a uniform spatial discretization, which is required to guarantee a conservative solution [70].

For the developed numerical model the use of a finite-difference WENO scheme would present additional difficulties related to nonlinear acoustic wave propagation in heterogeneous domains. In the finite-difference WENO schemes a combination of upwind fluxes is used to evolve the solution. As a result, this approach would not inherently accommodate wave reflections at material interfaces. As discussed in Section 3.2, a relatively intuitive solution to the problem of wave reflection at interfaces exists when using finite-volume WENO schemes, and it is for this reason the developed numerical model uses a finite volume formulation. If future development of the discussed numerical model should remain within the finite volume framework, some literature exists on simplifying the extension to multi-dimensional cases [68, 74]. Otherwise, if future development uses a finite-difference WENO scheme then additional methods for treating wave reflections at material interfaces would be required. One such technique based on the immersed boundary concept is developed for one dimensional domains in [55], and for two-dimensional domains in [49].

3.1.2 Overview of the Implemented WENO Scheme

Referring to the previous discussion on the evolution of ENO methods, the implemented scheme is consistent with the definition of a *characteristic-wise finite volume reconstruction* given in [70]. The reconstruction scheme can be broken down into three basic components: transformation to and from characteristic variables, evaluation of reconstruction polynomials, and evaluation of reconstruction smoothness. Throughout this section all necessary information is given for the implemented $r = 2$ (3^{rd} order) WENO scheme, the $r = 3$ (5^{th} order) WENO scheme, and the $r = 4$ (7^{th} order) WENO scheme, where r is the number of cells to the edge of the global stencil (including the reconstruction cell). For clarity, Figure 9 shows an example of the conventions used for indexing cells within the global and candidate stencils during the WENO reconstruction procedure.

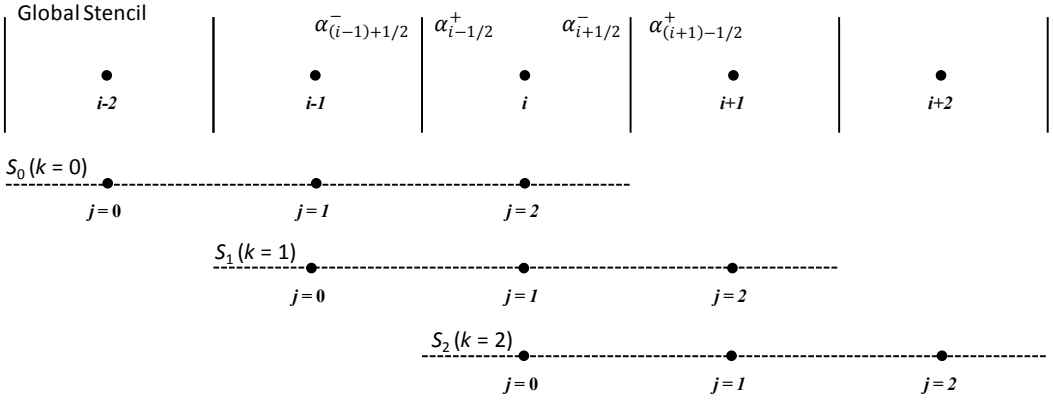

Figure 9: Stencil indexing conventions for the $r = 3$ WENO scheme.

3.1.3 Transformation to Characteristic Variables

The first stage in the finite volume WENO reconstruction is the transformation of state variables into their characteristic form. This transformation produces a system of independent scalar variables, and is required for stability of the high-order numerical schemes [32]. In the characteristic reconstruction procedure used in [32, 44, 70], the values in each reconstruction stencil are transformed using a single representative eigenvector $\boldsymbol{L}$. Each cell in internal regions of the numerical

domain belongs to *2r*-1 different stencils. This approach causes the total number of transformations applied to increases with the order of the reconstruction.

For the linearized acoustic equations the eigenvectors in matrix $\boldsymbol{L}$ are functions of only material properties and are constant throughout a homogeneous domain. As a result, each cells variables need to be transformed only once, and the resulting characteristic variables can be used in all applicable stencils. With the nonlinear acoustic equations the deviation from linearized eigenvectors is expected to be small. From this it has been assumed that the transformation to characteristic variables can be performed similarly, using just one inversion per computation cell using the local eigenvectors, $\boldsymbol{L}_i$. For the one-dimensional domain the characteristic variables are:

$$\boldsymbol{\alpha}_i = \boldsymbol{L}_i \boldsymbol{U}_i = \begin{bmatrix} \alpha_0 \\ \alpha_1 \end{bmatrix}_i = \frac{1}{2} \begin{bmatrix} \rho' - v_x \dfrac{(\rho' + \rho_o)}{c^*} \\ \rho' + v_x \dfrac{(\rho' + \rho_o)}{c^*} \end{bmatrix}_i \tag{3.4}$$

where the subscript *i* designates the use of local node values. This simplified approach has produced stable results all of the calculations performed during this work; however, no formal comparison with the more rigorous transformation method was made.

The right eigenvectors, $\boldsymbol{R}$, are obtained by noting that the value of ρ' can be uniquely identified using, $\rho' = \alpha_0 + \alpha_1$, and that $c^* = c^*(\rho')$. Considering a one-dimensional domain, the conservative variables are obtained using:

$$\boldsymbol{U}_{i+1/2} = \boldsymbol{R}_{i+1/2} \boldsymbol{\alpha}_{i+1/2} = \begin{bmatrix} 1 & 1 \\ \dfrac{-c^*}{(\rho' + \rho_o)} & \dfrac{c^*}{(\rho' + \rho_o)} \end{bmatrix}_{i+1/2} \begin{bmatrix} \alpha_0 \\ \alpha_1 \end{bmatrix}_{i+1/2} \tag{3.5}$$

where the index $i \pm ½$ designates the use of local values at each face.

3.1.4 Adaptive Reconstruction Polynomials

After transformation to characteristic variables, each component may be reconstructed as an independent scalar variable. This reconstruction procedure is described below for the one-dimensional reconstruction of $\alpha^{-}_{i+1/2}$, which is the characteristic variable on the left of cell face i + ½, as denoted by the '-' superscript. For reconstructing $\alpha^{+}_{i-1/2}$ the procedure is symmetric with respect to x_i. For additional clarity on this notation convention refer to Figure 9.

First, a group of lower order reconstruction polynomials, q^r_k, is calculated for the candidate stencils, S_k, to produce a series of O(Δx^r) accurate approximations for $\alpha^{-}_{i+1/2}$ [36]:

$$\alpha^{-}_{i+1/2} = q^r_k(\alpha_{i+k-r+1}, \dots, \alpha_{i+k}) + O(\Delta x^r) \tag{3.6}$$

where r is the maximum stencil radius, k is the candidate stencil index, and in general k = [*0*, …, *r-1*]. As the node values, α_i, represent integrated cell averages the candidate polynomials are found according to the following equation [48]:

$$\int_{x_{i-1/2}}^{x_{i+1/2}} q^r_k(x)dx = \alpha_i \tag{3.7}$$

Evaluation of Equation (3.7) to produce the corresponding polynomials is well described in [43]; however, when evaluating reconstructed values at a particular location, such as i + ½, the high-order polynomial expression for q^r_k can be simplified to a linear combination of node values within the candidate stencil [36]:

$$q^r_k(\alpha_0, \dots, \alpha_{r-1}) = \sum_{j=0}^{r-1} c^k_j \, \alpha_j \tag{3.8}$$

where the linear coefficients c^k_j are functions only of the grid geometry. For uniform grids the coefficients c^k_j are widely available in the literature. These values are summarized in Table 2 from [36] for the 3rd order r = 2 scheme and for the 5th order r = 3 scheme, and from [5] for the 7th order r = 4 scheme:

Table 2: Summary of WENO reconstruction coefficients.

		c_j^k			
k	d_k	$j = 0$	$j = 1$	$j = 2$	$j = 3$
$r = 2$					
0	1/3	-1/2	3/2		
1	2/3	1/2	1/2		
$r = 3$					
0	1/10	1/3	-7/6	11/6	
1	6/10	-1/6	5/6	1/3	
2	3/10	1/3	5/6	-1/6	
$r = 4$					
0	1/35	-1/4	13/12	-23/12	25/12
1	12/35	1/12	-5/12	13/12	3/12
2	18/35	-1/12	7/12	7/12	-1/12
3	4/35	1/4	13/12	-5/12	1/12

For non-uniform grids the coefficients can be computed during solver initialization and stored for reuse using the algorithm provided in [70].

From the lower-order candidate polynomials the higher order combination is made according to:

$$Q^{2r-1}(\alpha_{i-r+1}, \dots, \alpha_{i+r-1}) = \sum_{k=0}^{r-1} \widehat{\omega}_k \, q_k^r(\alpha_{i+k-r+1}, \dots, \alpha_{i+k}) \tag{3.9}$$

$$\widehat{\omega}_k = \frac{\omega_k}{\sum \omega_k}, \qquad \omega_k = \frac{d_k}{(IS_k + \epsilon)^p} \tag{3.10}$$

where $\widehat{\omega}_k$ is the candidate weighting, ω_k is the non-normalized candidate weight, d_k is the optimal weight value, IS_k is the candidate smoothness measure. Discussion on the evaluation of IS_k is left to the next section. The variable ϵ is required to prevent division by zero and is taken to have a value of $\epsilon = 10^{-40}$. The parameter, p, affects the sensitivity of the WENO scheme to changes in smoothness. High values of p reduce the presence of numerical oscillations in the solution, but also tend to add dissipative error that attenuates propagating waves. Most often a value of $p = 2$ is recommended [5, 36, 70], and unless otherwise noted all calculations presented in this thesis follow this recommendation. The optimal values, d_k, in Equation (3.10) are chosen to allow for a $O(\Delta x^{2r-1})$

reconstruction when all candidates are equally smooth:

$$\alpha^{-}_{i+1/2} = Q^{2r-1}(\alpha_{i-r+1}, \dots, \alpha_{i+r-1}) + O(\Delta x^{2r-1}) \tag{3.11}$$

Similar to the candidate stencil coefficients c_j^k, values for d_k are widely available in the literature for uniform grids. Table 2 provides the values from [36] for the 3rd order $r = 2$ scheme and the 5th order $r = 3$ scheme, and from [5] for the 7th order $r = 4$ scheme.

3.1.5 WENO Smoothness Measures

An important aspect of the WENO reconstruction schemes is the measure used to evaluate the smoothness of each candidate stencil, IS_k. In this context smoothness is essentially the severity of spatial gradients in the solution. The original WENO smoothness measure proposed in [48] has largely been superseded by more recent works. The most widely adopted smoothness measure was first described by Jiang and Shu [36]. This measure quantifies smoothness as the integrated L_2 norm of all spatial derivatives produced by the reconstruction polynomials. The formal expression for this evaluation is given by:

$$IS_k = \sum_{l=1}^{r-1} \int_{x_R}^{x_L} \Delta x^{2l-1} \left(\frac{\partial^l q_k}{\partial x^l} \right)^2 dx \tag{3.12}$$

For uniform grids this smoothness measure integral can be evaluated, resulting in simplified algebraic expressions. This evaluation is carried out in the literature, and the results are presented here so that the formulation of the numerical model would be complete.

Smoothness measure for the r = 2 WENO scheme [36]:

$$\begin{aligned} IS_0 &= (\alpha_i - \alpha_{i-1})^2 \\ IS_1 &= (\alpha_{i+1} - \alpha_i)^2 \end{aligned} \tag{3.13}$$

Smoothness measure for the r = 3 WENO scheme [36]:

$$IS_0 = \frac{13}{12}(\alpha_{i-2} - 2\alpha_{i-1} + \alpha_i)^2 + \frac{1}{4}(\alpha_{i-2} - 4\alpha_{i-1} + 3\alpha_i)^2$$

$$IS_1 = \frac{13}{12}(\alpha_{i-1} - 2\alpha_i + \alpha_{i+1})^2 + \frac{1}{4}(\alpha_{i-1} - \alpha_{i+1})^2 \tag{3.14}$$

$$IS_0 = \frac{13}{12}(\alpha_i - 2\alpha_{i+1} + \alpha_{i+2})^2 + \frac{1}{4}(3\alpha_i - 4\alpha_{i+1} + \alpha_{i+2})^2$$

Smoothness measure for the r = 4 WENO scheme [5]:

$$\begin{aligned}
IS_0 &= \alpha_{i-3}(547\alpha_{i-3} - 3882\alpha_{i-2} + 4642\alpha_{i-1} - 1854\alpha_i) + \\
&\alpha_{i-2}(7043\alpha_{i-2} - 17246\alpha_{i-1} + 7042\alpha_i) + \alpha_{i-1}(11003\alpha_{i-1} - \\
&9402\alpha_i) + 2107\alpha_i^2 \\
IS_1 &= \alpha_{i-2}(267\alpha_{i-2} - 1642\alpha_{i-1} + 1602\alpha_i - 494\alpha_{i+1}) + \\
&\alpha_{i-1}(2843\alpha_{i-1} - 5966\alpha_i + 1922\alpha_{i+1}) + \alpha_i(3443\alpha_i - \\
&2522\alpha_{i+1}) + 547\alpha_{i+1}^2 \\
IS_2 &= \alpha_{i-1}(547\alpha_{i-1} - 2522\alpha_i + 1922\alpha_{i+1} - 494\alpha_{i+2}) + \\
&\alpha_i(3443\alpha_i - 5966\alpha_{i+1} + 1602\alpha_{i+2}) + \alpha_{i+1}(2843\alpha_{i+1} - \\
&1642\alpha_{i+2}) + 267\alpha_{i+2}^2 \\
IS_3 &= \alpha_i(2107\alpha_i - 9402\alpha_{i+1} + 7042\alpha_{i+2} - 1854\alpha_{i+3}) + \\
&\alpha_{i+1}(11003\alpha_{i+1} - 17246\alpha_{i+2} + 4642\alpha_{i+3}) + \alpha_{i+2}(7043\alpha_{i+2} - \\
&3882\alpha_{i+3}) + 547\alpha_{i+3}^2
\end{aligned} \tag{3.15}$$

More recent works by Borges et al. [9] and Shen et al. [66] have proposed a modified smoothness measure to reduce the numerical dissipation incurred by WENO schemes. In their measure, which is termed WENO-Z, the smoothness value for each candidate stencil is normalized by the variation in the total stencil according to:

$$\begin{aligned}
\tau &= |IS_0 - IS_r| \\
IS_k^Z &= \frac{IS_k + \epsilon}{IS_k + \tau + \epsilon}
\end{aligned} \tag{3.16}$$

This normalization has the qualitative effect of slightly increasing the contribution of non-smooth stencils to reduce dissipation at discontinuities [9]. To implement

the modified smoothness measure Borges et al. [9] suggest applying the parameter τ directly to the weighting coefficient as follows:

$$\omega_k^Z = d_k \left(1 + \left(\frac{\tau}{IS_k + \epsilon}\right)^p\right) \tag{3.17}$$

In this modified weighting the coefficient p is equal to 1 to minimize numerical dissipation. However, in [9] it is also noted that in order to guarantee 5th order convergence the $r = 3$ WENO-Z scheme should use $p = 2$, while [66] notes that p > 4/3 is required to guarantee 7th order convergence of the $r = 4$ WENO-Z scheme. During preliminary calculations for this work it was observed that the use of $p < 2$ was not sufficient damp all numerical oscillations in shock wave propagation. For this reason $p = 2$ is used even with the WENO-Z schemes.

3.2 Flux Solvers and Riemann Solvers

As depicted in Figure 10, after completion of the high-order reconstruction stage each face in the computational domain is assigned two values of conservative variables (left and right). To evaluate the fluxes across the face many general flux-decomposition techniques are available to calculate a stable combination of upwind flux components [43]. Alternatively, the discontinuous jump in state values at each face can be approached as a classic Riemann problem from gasdynamics. As shown in Figure 10, a Riemann problem is the wave field and gas flow produced by two adjacent gas states with a discontinuous interface. With the Euler equations the Riemann problem has an exact but implicit solution that must be solved iteratively [43]. A more popular approach is to approximate the Riemann solution to avoid numerical iteration; this approach has successfully been used in many applications involving fluid flow and wave phenomena. As the linear and nonlinear acoustic equations provided in Chapter 2 are simplifications of the Euler equations, many of these existing approximate Riemann solvers are relevant to the developed numerical model.

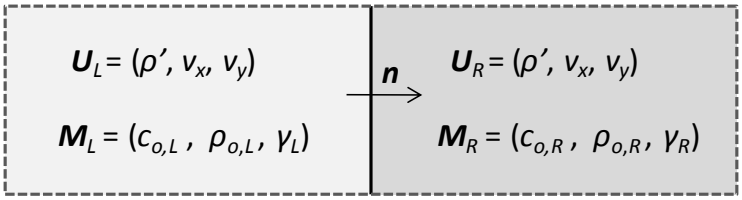

Figure 10: Schematic depiction of the Riemann problem.

For much of the computational domain material properties on the left and right of face, denoted $\boldsymbol{M}_L$ and $\boldsymbol{M}_R$, are the same and solution of the Riemann problem becomes simpler. At locations where a material interface occurs this is not the case and it is shown below that a non-conservative application of fluxes is needed to allow for proper wave transmission from one material to another.

It is also useful to note that the wave propagation problem scenarios applicable to the developed numerical model are of linear or weakly nonlinear wave propagation, where the wave strengths meet the requirements: $(\rho'/\rho_o) \ll 1$ and $(u/c_o) \ll 1$. Under these restrictions sonic or supersonic flow, where $u/c_o \geq 1$, does not occur and only sub-sonic flux and Riemann solutions need to be considered.

3.2.1 Conservative Solutions for Homogeneous Regions

In general, the Riemann problem between two cells containing identical materials can be evaluated using any of the techniques presented within this thesis. Presented in this section is the HLL approximate Riemann solver by Harten et al. [31]. In the numerical model the HLL solver is applied at all cell faces that do not represent a material interface. This is done to improve computational efficiency as the HLL algorithm is simpler than those needed to treat material interfaces. Additionally, in Subsection 3.2.5 is illustrated that the HLL solver is equivalent to the other implemented solvers for the homogeneous material case.

As depicted in Figure 11, the central idea to the HLL solver is to approximate the Riemann solution as a single averaged region bounded by the minimum and maximum wave speeds.

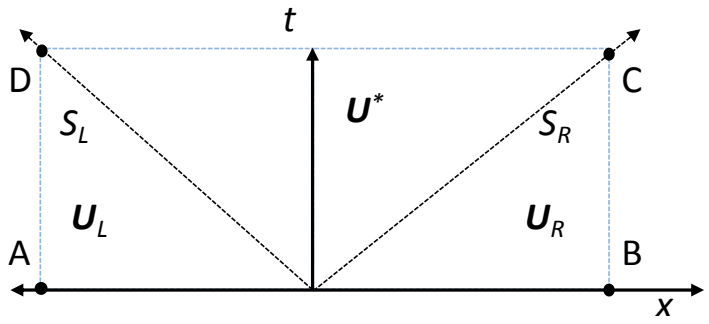

Figure 11: HLL approximation of the one-dimensional Riemann problem.

As succinctly demonstrated by Toro et al. [75], the evaluation of the one-dimensional conservation integral:

$$\oint(\boldsymbol{U}dx - \boldsymbol{F}dt) = 0 \tag{3.18}$$

over the region *ABCD* in Figure 11, produces a direct expression for the averaged contact state, $\boldsymbol{U}^*$, and the corresponding flux, $\boldsymbol{F}^*$:

$$\boldsymbol{U}^* = \frac{S_R\boldsymbol{U}_R - S_L\boldsymbol{U}_L + \boldsymbol{F}_L - \boldsymbol{F}_R}{S_R - S_L} \tag{3.19}$$

$$\boldsymbol{F}^* = \frac{S_R\boldsymbol{F}_L - S_L\boldsymbol{F}_R + S_LS_R(\boldsymbol{F}_L - \boldsymbol{F}_R)}{S_R - S_L} \tag{3.20}$$

When solving for the homogeneous linear acoustic equations the wave speeds are constant values of $S_L = -c_o$ and $S_R = +c_o$. Where solving for the homogeneous nonlinear acoustic equations the wave speeds are no longer constant and an accurate estimate is needed. This topic is discussed in greater detail in Section 3.2.6, and for now it is sufficient to give the initial estimates, which are chosen to be the eigenvalues from the left and right initial states, $S_L = \lambda_L^-$ and $S_R = \lambda_R^+$.

3.2.2 Non-Conservative Solutions for Material Interfaces

When used with the Euler equations the primary limitation of the HLL solver is its inability to represent density or material interfaces [75]. In conventional gasdynamics where the HLL solver is more commonly applied, the problem scenarios may contain multiple gasses that flow and mix throughout the domain.

The mixing of these gasses governed by physically based models; however, when two neighboring cells contain a large difference in density or material content, mixing also occurs as result of numerical error. The HLL solver, which produces high levels of mixing error, is therefore an inappropriate choice for treating material interfaces.

When considering acoustic equations the requirements for accommodating non-homogeneous domains are somewhat different. Underlying both the linear and nonlinear governing equations is an assumption that the domain can be represented using piecewise-continuous materials. Essentially this means that changes in materials are represented by discrete interfaces and these interfaces do not allow mixing (mass transfer) of the materials. Under this assumption any solver that represents or admits mixing, such as the HLL solver, introduces an error into the solution and degrades wave transmission properties at the interface. For this reason a forced prevention of material mixing is seen as an acceptable compromise, as wave propagation and reflection is of primary interest. Indeed, the development of a scheme that admits fluid flow, material mixing, and proper wave reflections at material interfaces is a more challenging problem that the one currently addressed.

After some review, the techniques developed by LeVeque [47] and furthered by Fogarty and LeVeque [28] were found to meet the requirement of producing correct wave transmission at material interfaces within the framework of a Godunov scheme. In the limit of acoustic wave strengths, it was found that Leveque's method is equivalent to a non-conservative application of the HLLC [75] approximate Riemann solution, which is the approach ultimately chosen for the developed numerical model.

3.2.3 Flux-Difference Splitting for Wave Transmission Properties

This subsection is presented to give relevant background and justification for the modified HLLC implementation that is used. Importantly, this subsection demonstrates an approximate Riemann solver that guarantees correct wave transmission properties, while is Subsection 3.2.3 and Subsection 3.2.5 the

modified HLLC solver is shown to posses these same properties. Although this *flux-differencing* solver is included in the developed model, all calculation results presented in this thesis have used the HLL and HLLC solvers.

In LeVeque [47] and in Fogarty and LeVeque [28], a *flux-differencing* scheme is presented for multidimensional hyperbolic systems. This approach is centered on evaluation of the Riemann problem using a series of discrete compression, rarefaction, or contact waves. To introduce the scheme we will first consider the case of a one-dimensional homogeneous acoustic system. For a system containing N_w waves – each corresponding to a system eigenvalue – a jump across the each wave, $\boldsymbol{W}^p$, is defined so that:

$$\boldsymbol{q}_r - \boldsymbol{q}_l = \sum_{p=1}^{N_w} \boldsymbol{W}^p \tag{3.21 a}$$

$$\boldsymbol{q} = \begin{bmatrix} p \\ v_x \end{bmatrix} \tag{3.21 b}$$

$$\boldsymbol{f}(\boldsymbol{q}) = \begin{bmatrix} v_x c_o^2 \rho_o \\ p/\rho_o \end{bmatrix} \tag{3.21 c}$$

where $\boldsymbol{q}$ is the state vector, p is the pressure perturbation, and $\boldsymbol{f}$ is the corresponding flux vector. As shown in Figure 12, the acoustic system produces just two waves at each face, one left-propagating and one right-propagating.

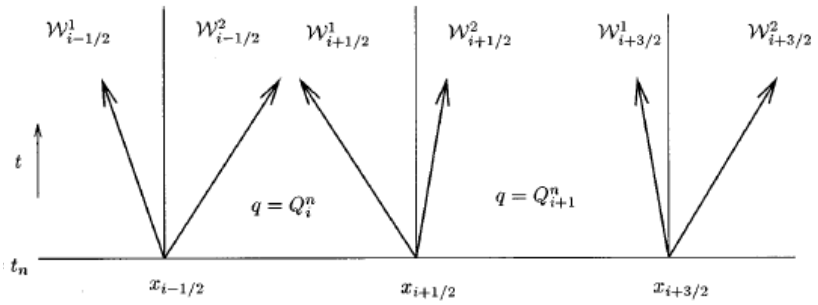

Figure 12: Wave field solved by flux-differencing scheme. Reproduced from [28].

For the one-dimensional system the jump across each wave leads to a consistent intermediate state, $\boldsymbol{q}^*$, which can be used to determine fluxes. Following a first-order Godunov method, solutions in each control volume could be evolved

according to:

$$\boldsymbol{q}_i^{n+1} = \boldsymbol{q}_i - \frac{\Delta t}{\Delta x}\left(\boldsymbol{f}\left(\boldsymbol{q}_{i+1/2}^*\right) - \boldsymbol{f}\left(\boldsymbol{q}_{i-1/2}^*\right)\right) \tag{3.22}$$

In contrast, a *flux-difference splitting* technique is used in [47], where *flux-differences* for the homogeneous acoustic system are defined as:

$$\begin{aligned} A^-\Delta\boldsymbol{q}_{\boldsymbol{i+1/2}} &= \lambda_i^-\boldsymbol{W}_i^- = \boldsymbol{f}\left(\boldsymbol{q}_{i+1/2}^*\right) - \boldsymbol{f}(\boldsymbol{q}_i) \\ A^+\Delta\boldsymbol{q}_{\boldsymbol{i-1/2}} &= \lambda_i^+\boldsymbol{W}_i^+ = \boldsymbol{f}(\boldsymbol{q}_i) - \boldsymbol{f}\left(\boldsymbol{q}_{i-1/2}^*\right) \end{aligned} \tag{3.23}$$

Then the first order solution is updated according to:

$$\boldsymbol{q}_i^{n+1} = \boldsymbol{q}_i^n - \frac{\Delta t}{\Delta x}\left(A^+\Delta\boldsymbol{q}_{i-1/2} + A^-\Delta\boldsymbol{q}_{i+1/2}\right) \tag{3.24}$$

The method is extended to non-conservative systems by using this *flux-difference splitting* approach. At a material interface the state $\boldsymbol{q}^*$ remains consistent due to the choice of state variables; however, as flux is a function of both the state and material properties it is now the case that the total *flux-difference* is not equal to the net change in the flux vector from the left to the right state [47]:

$$A^-\Delta\boldsymbol{q}_{\boldsymbol{i+1/2}} + A^+\Delta\boldsymbol{q}_{\boldsymbol{i-1/2}} \neq \boldsymbol{F}_R - \boldsymbol{F}_L \tag{3.25}$$

It is important to note that $A^{\pm}\Delta\boldsymbol{q}$ are functions of the initial states and the local material properties, but they are not governed by an overall conservation requirement. It is this set of principles that allow Leveque's *flux-differencing* techniques to produce the proper transmission of waves from one material to the next.

In order to complete the solution it is necessary to solve the jump conditions $W^{\pm}$. LeVeque [47] demonstrates the jump across each wave, defined by a system eigenvalue, is a scalar multiple, α, of the corresponding right eigenvector from the flux Jacobian. For the following equations provide these expressions in the context of the linear acoustic Riemann problem:

$$\boldsymbol{A}_K = \begin{bmatrix} 0 & c_o^2\rho_o \\ \frac{1}{\rho_o} & 0 \end{bmatrix}_K, \qquad K = (L, R) \tag{3.26 a}$$

$$\boldsymbol{W}^{-} = \alpha_L^{-}\boldsymbol{r}_L^{-}\,, \qquad \boldsymbol{r}_L^{-} = \boldsymbol{r}(\lambda_L^{-}) = \begin{bmatrix} -c_o \\ 1/\rho_o \end{bmatrix}_L \tag{3.26 b}$$

$$\boldsymbol{W}^{+} = \alpha_R^{+}\boldsymbol{r}_R^{+}\,, \qquad \boldsymbol{r}_R^{-} = \boldsymbol{r}(\lambda_R^{+}) = \begin{bmatrix} c_o \\ 1/\rho_o \end{bmatrix}_R \tag{3.26 c}$$

As a result the physical continuity conditions $(\boldsymbol{q}^*)_L = (\boldsymbol{q}^*)_R$, it is possible to equate the left and right intermediate state vectors to solve for the wave strengths, $\alpha^{\pm}$, by:

$$\boldsymbol{q}_L^* = \boldsymbol{q}_L + W^{-} \qquad\qquad \boldsymbol{q}_R^* = \boldsymbol{q}_R - W^{+} \tag{3.27 a}$$

and:

$$\boldsymbol{q}_L + \alpha_L^{-}\boldsymbol{r}_L^{-} = \boldsymbol{q}_R - \alpha_R^{+}\boldsymbol{r}_R^{+} \tag{3.27 b}$$

After some algebraic manipulations it can be shown that a matrix form solution to the wave strengths is:

$$\widehat{\boldsymbol{\alpha}} = \boldsymbol{R}^{-1}\Delta\boldsymbol{Q} \tag{3.28 a}$$

where:

$$\widehat{\boldsymbol{\alpha}} = \begin{bmatrix} \alpha_L^{-} \\ \alpha_R^{+} \end{bmatrix} \tag{3.28 b}$$

$$\Delta\boldsymbol{Q} = \boldsymbol{q}_R - \boldsymbol{q}_L \tag{3.28 c}$$

$$\boldsymbol{R} = [\boldsymbol{r}_L^{-} \quad \boldsymbol{r}_R^{+}] = \begin{bmatrix} -c_{o,L} & +c_{o,R} \\ 1/\rho_{o,L} & 1/\rho_{o,R} \end{bmatrix} \tag{3.28 d}$$

To apply these techniques to the governing equations in Chapter 2, two additional steps are required. Firstly, as the state variables $\boldsymbol{U} = (\rho', v_x)$ differ from those in the preceding derivation, $\boldsymbol{q} = (p, \mathrm{v_x})$, a transformation $\boldsymbol{U} = \boldsymbol{U}(\boldsymbol{q})$ is needed. For the linear acoustic equations this transformation is straightforward: $p' = c_o^2\rho'$. Secondly, the solution produced by the *flux-difference splitting* method must be adapted to the discrete spatial operator used with Runge-Kutta time integration. This is done by allowing two flux vectors, $\boldsymbol{F_L}$ and $\boldsymbol{F_R}$, to be assigned to each face, where each is a function of the respective initial state and jump condition:

$$\boldsymbol{F}_{\boldsymbol{L}}^{*} = A^{-}\Delta\boldsymbol{U}_{\boldsymbol{L}} = \boldsymbol{F}\big(\boldsymbol{U}(\boldsymbol{q}_L + \alpha_L^{-}\boldsymbol{r}_L^{-})\big) \tag{3.29 a}$$

$$\boldsymbol{F}_{\boldsymbol{R}}^{*} = A^{+}\Delta\boldsymbol{U}_{\boldsymbol{R}} = \boldsymbol{F}\left(\boldsymbol{U}(\boldsymbol{q}_R - \alpha_R^{+}\boldsymbol{r}_R^{+})\right) \tag{3.29 b}$$

In one spatial dimension the discrete spatial operator from Equation (3.2) can then be evaluated according to:

$$\boldsymbol{L}_i = \frac{\partial \boldsymbol{U}_i}{\partial t} = -\frac{1}{\Delta x}\left(\boldsymbol{F}_{\boldsymbol{L},i+1/2}^{*} - \boldsymbol{F}_{\boldsymbol{R},i-1/2}^{*}\right) \tag{3.30}$$

In general, the *flux-difference splitting* technique is extendable to nonlinear systems such as the Euler equations or the nonlinear acoustic equations. When solving these nonlinear systems a local linearization of the flux Jacobian and eigenvectors can be used and the solution may then proceed as previously described. For the Euler equations, Leveque [47] suggests the use of the Roe linearization [63] at each face. For the nonlinear acoustic equations presented in Chapter 2, the derivation of the Roe average Matrix has not been carried out (see the discussion in Subsection 3.2.7). Thus another method for capturing nonlinear wave reflections is required. To meet this requirement a modified HLLC approximate Riemann solver is presented in Subsection 3.2.4, while Subsection 3.2.5 provides justification for this choice.

3.2.4 HLLC Approximate Riemann Solver

In the previous section the fundamental principles of an acoustic wave propagating Riemann solver were presented. This section now describes a modified HLLC solver that is consistent with these principles. For all calculations presented in this these, it is this HLLC solver that is applied at material interfaces.

The HLLC approximate Riemann solver developed in [75] is an extension of the HLL technique that is capable of resolving the contact surface between the initial left and right states. When used with the Euler equations the HLLC solver is known to reduce numerical mixing of materials and to reduce degradation of contact surfaces. Similar to the principles of the HLL solver in Subsection 3.2.1, the HLLC solution is obtained by evaluating the one-dimensional conservation integrals given Equation (3.18) over the regions *ABCE* and *EFGH* (Figure 13).

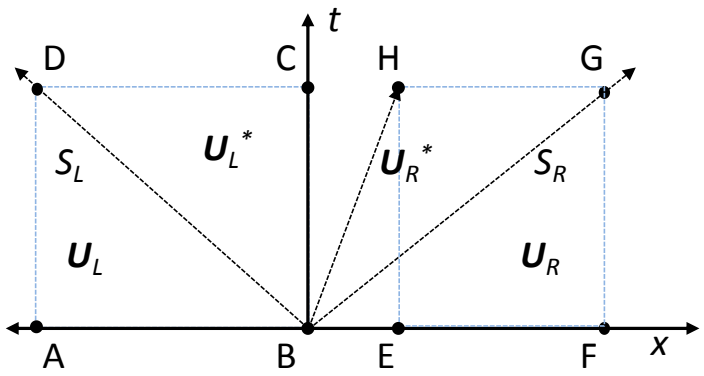

Figure 13: HLLC approximation of the one-dimensional Riemann problem.

The results of this evaluation are as follows:

$$S_K \boldsymbol{U}_K^* - \boldsymbol{F}_K^* = S_K \boldsymbol{U}_K - \boldsymbol{F}_K, \qquad K = (L, R) \tag{3.31}$$

Similar to the HLL solver, values of S_L and S_R are assumed to be known; for an initial estimate the eigenvalues from the left and right initial states, $S_L = \lambda_L^-$ and $S_R = \lambda_R^+$can be used, and then for improved estimates refer to Subsection 3.2.6. To solve the Riemann problem it is necessary to determine the contact velocity, v^*. For problems where n_x = 1 and n_y = 0, or alternatively when using a local coordinate system with n_η = 1 and n_ϵ = 0 the contact velocity is equivalent to the x-normal velocity of the left and right intermediate states. For the Euler equations the contact velocity is solved by simultaneous evaluation of Equation (3.31) for the left and right states to give [6]:

$$v^* = \frac{\rho_L v_L (S_L - v_L) - \rho_R v_R (S_R - v_R) + (p_R - p_L)}{\rho_L (S_L - v_L) - \rho_R (S_R - v_R)} \tag{3.32 a}$$

where the subscripts are dropped from u_x or u_η for convenience. Instead of carrying out a similar derivation for the linear acoustic and nonlinear acoustic equations, it is simpler to use the contact velocity from Equation (3.32 a), then retain only O(v_x/c_o) terms for use with linear acoustic systems, and retain only O$(v_x/c_o)^2$ terms for use with nonlinear acoustic systems. Using this approach the resulting expressions for contact velocity are:

$$v^*_{linear} = \frac{-\rho_{o,L} v_L c_{o,L} - \rho_{o,R} v_R c_{o,R} + (p_R - p_L)}{-\rho_{o,L} c_{o,L} - \rho_{o,R} c_{o,R}} \tag{3.32 b}$$

$$v^*_{nonlinear} = \frac{(\rho_{o,L} + \rho'_L) v_L (S_L - v_L) - (\rho_{o,R} + \rho'_R) v_R (S_R - v_R) + (p_R - p_L)}{(\rho_{o,L} + \rho'_L)(S_L - v_L) - (\rho_{o,L} + \rho'_L)(S_R - v_R)} \tag{3.32 c}$$

where p for the linear and nonlinear case are functions of ρ' defined in Chapter 2. To complete the HLLC solution intermediate state values for ρ' are needed. These can be obtained directly from Equation (3.31). The resulting expressions are:

$$\rho'^*_{K,linear} = \frac{\rho_{o,K}(u^* - v_{x,K}) + S_K \rho'_K}{S_K} \tag{3.33 a}$$

$$\rho'^*_{K,nonlinear} = \frac{\rho_{o,K}(u^* - v_{x,K}) + \rho'_K (S_K - v_{x,K})}{S_K} \tag{3.33 b}$$

To allow for proper wave transmission, fluxes corresponding to these fluid states are applied using a method that is consistent with the discussed *flux-difference splitting*. When applied to the HLLC Riemann solution this gives the following fluxes:

$$\boldsymbol{F}^*_{\boldsymbol{L}} = A^- \Delta \boldsymbol{U}_L = \boldsymbol{F}(\boldsymbol{U}^*_{L,HLLC}) \tag{3.34 a}$$

$$\boldsymbol{F}^*_{\boldsymbol{R}} = A^+ \Delta \boldsymbol{U}_R = \boldsymbol{F}(\boldsymbol{U}^*_{R,HLLC}) \tag{3.34 b}$$

3.2.5 Equivalence of HLLC and Flux-Difference Splitting

Before addressing flux solutions at a material interface the equivalence of HLL and HLLC solvers in homogeneous regions is considered. By applying the linear acoustic relation, $p' = c_o^2 \rho'$, to Equation (3.32 b) and by calculating the velocities, v_x, from Equation (3.19), it can be shown that the HLL and HLLC solvers produce equivalent contact state velocities for a homogeneous linear acoustic system. Similarly, the two solvers can be shown to produce equivalent contact states for a homogeneous nonlinear system provided the choices for wave speeds are the same.

Now let us consider the linear acoustic flux solution at a material interface. In Subsection 3.2.4 a method was given to apply HLLC fluxes in a manner

consistent with *flux-difference* method in Subsection 3.2.3. By comparing Equation (3.34) with Equation (3.29) it is evident that the solution produced by the non-conservative application of HLLC flux vectors is equivalent to *flux-difference splitting* if both methods predict the same contact state, i.e., if $\boldsymbol{U}^*_{L,HLLC} = \boldsymbol{U}(\boldsymbol{q}_L + \alpha_L^- \boldsymbol{r}_L^-)$. To demonstrate this property it is most convenient to start from the *flux-difference* result. From Equation (3.27) and Equation (3.28), the contact velocity predicted by the *flux-difference splitting* solver is:

$$v_x^* = v_{x,L} + \frac{\alpha_L^-}{\rho_{o,L}} \tag{3.35 a}$$

$$\alpha_L^- = \frac{1}{\left(c_{o,L}/\rho_{o,R} + c_{o,R}/\rho_{o,L}\right)}\left(\frac{P_L - P_R}{\rho_{o,R}} + c_{o,R}\left(v_{x,R} - v_{x,L}\right)\right) \tag{3.35 b}$$

which simplifies to:

$$v_x^* = \frac{(\rho_o c_o v_x)_L + (\rho_o c_o v_x)_R + (P_L - P_R)}{(\rho_o c_o)_L + (\rho_o c_o)_R} \tag{3.36}$$

This form of the contact velocity is equivalent to Equation (3.32 b) from the linearized HLLC solver. As a result of these findings two useful conclusions have been drawn. First, in the limit of acoustic wave strength a non-conservative application of fluxes from the HLLC Riemann solver is guaranteed to produce the correct wave transmission properties at a non-mixing material interface. Second, as the HLLC solver is more readily extended to the nonlinear acoustic equations its use is preferable over that of the *flux-difference splitting* technique.

A similar effort to show equivalence between the *flux-difference* solver and the HLLC solver was not carried out for the nonlinear acoustics equations. This is a result of the underlying difficulty in extending the *flux-difference* solver to the nonlinear acoustic equations. As previously discussed in Subsection 3.2.3, a Roe linearization is needed to extend the *flux*-difference solver. For the nonlinear acoustic equations determination of the Roe linearization is not straightforward. The causes of this difficulty are further discussed in Subsection 3.2.7.

3.2.6 Wave Speed Estimates for HLL and HLLC

To improve solver accuracy high quality estimates for S_L and S_R are used in the HLL and HLLC Riemann solvers. For the linear acoustic equations the S_L and S_R wave speeds are constant values as defined by the system eigenvalues:

$$S_{L,linear} = \lambda_L^- = -c_{o,L} \tag{3.37 a}$$

$$S_{R,linear} = \lambda_R^+ = c_{o,R} \tag{3.37 b}$$

For the nonlinear case Batten et al. [6] suggests wave speed selections as the minimum and maximum eigenvalues from the initial left, right, and Roe averaged contact state, $\boldsymbol{U}^*_{Roe}$.

$$S_{L,nonlinear} = \min[\lambda^-(\boldsymbol{U_L}), \lambda^-(\boldsymbol{U}^*_{Roe})] \tag{3.38 a}$$

$$S_{R,nonlinear} = \max[\lambda^+(\boldsymbol{U_R}), \lambda^+(\boldsymbol{U}^*_{Roe})] \tag{3.38 b}$$

For reasons discussed in Subsection 3.2.7, the Roe linearization algorithm has not been included in the numerical model, and an alternative method to estimate the contact state eigenvalues was required. For this purpose an earlier suggestion by Toro et al. [75] is used, where the intermediate state is initially estimated using the preliminary estimates of the wave speeds. To elaborate on this process, the preliminary wave speed estimates are:

$$S_L^{'} = \lambda_L^- = u_L - c_L \tag{3.38 a}$$

$$S_R^{'} = \lambda_R^+ = u_R + c_R \tag{3.38 b}$$

$$S_M^{'} = u^*_{HLLC}(\boldsymbol{U}_L, \boldsymbol{U}_R, S_L^{'}, S_R^{'}) \tag{3.38 c}$$

Using these estimates the approximate solution to contact state is:

$$\boldsymbol{U}^{*\prime} = \boldsymbol{U}^*_{HLLC}(\boldsymbol{U}_L, \boldsymbol{U}_R, S_L^{'}, S_R^{'}, S_M^{'}) \tag{3.39 a}$$

$$c_K^{*\prime} = c^*_{K,HLLC}(\boldsymbol{U}_K^{*\prime}) \tag{3.39 b}$$

Using the approximate contact state solution updated values for wave speeds are determined according to:

$$S_L = \min\left[(u_L - c_L), \left(u^{*'} - c_L^{*'}\right)\right] \quad (3.40\text{ a})$$

$$S_R = \max\left[(u_R + c_R), \left(u^{*'} + c_R^{*'}\right)\right] \quad (3.40\text{ b})$$

This procedure essentially requires two evaluations of the HLL or HLLC algorithms, adding to the computational requirements of the overall flux solution. As the nonlinearity of the problems considered is expected to be small the difference between S_K' and S_K is also expected to be small. In the present work this two stage solution has been used; however, if future applications are more computationally demanding it may be acceptable to use just the first stage wave speed estimates.

3.2.7 Roe Linearization at Material Interfaces

This subsection is presented as a brief discussion on the potential use of the Roe solver [63] for the nonlinear acoustic equations. After implementing the *flux-differencing* scheme for the linear acoustic equations, some considerations were given to extending the method with a Roe linearization for the nonlinear equations. Ultimately, this approach was abandoned in favor of the HLLC methods shown in Subsections 3.2.4 and 3.2.6. Unlike the HLLC, Roe's expressions derived from the Euler equations are not intuitively transferable to the nonlinear acoustic equations. In general the derivation of a Roe linearized Jacobian can be carried out for equations sets other than the Euler equations, but the results may not as simple. By examining the nonlinear acoustic equations in Chapter 2 it can be seen that they are not *homogeneous of order one,* in the sense that $\boldsymbol{F}(k\boldsymbol{U}) \neq k\boldsymbol{F}(\boldsymbol{U})$. As noted by Roe [63], much of the simplicity apparent in the linearization of the Euler equations stems from their *homogeneous of order one* property. For this reason, the Roe average Jacobian and eigenvectors may lack the simplicity to make Roe linearization an attractive option.

3.3 Spectral Properties of the Reconstruction and Flux Scheme

To better appreciate the influence of the WENO reconstruction and the two smoothness measures on wave propagation properties, analysis using the approximate dispersion relation (ADR) developed by Pirozzoli [58] has been conducted. The ADR analysis is similar to the analytical concept of a modified wave number used by Lele [46], but is more general to include schemes that cannot be evaluated analytically. This technique has previously been applied to the standard WENO schemes [58], but new analysis for the WENO-Z schemes is reported here. To perform the ADR analysis a sinusoidal wave is initialized on the computational grid and then the solution is advanced for a very short time, $\tau \ll 1$. By choosing a suitably small value of τ, the solution contains errors predominantly produced by the reconstruction and flux schemes. For the analysis conducted in this section the HLL flux was used. By comparing the Fourier coefficient of the initial wave, $\hat{u}_o(\phi_n)$, to the Fourier coefficient of the propagated wave, $\hat{u}(\phi_n, \tau)$, dissipative and dispersive properties of schemes can be approximated. From [58] the ADR is defined as:

$$\Phi(\phi_n) = \frac{i}{\sigma} \log\left(\frac{\hat{u}(\phi_n, \tau)}{\hat{u}_o(\phi_n)}\right) \tag{3.41 a}$$

$$\phi_n = \frac{2\pi}{N} \tag{3.41 b}$$

$$\sigma = c_o \tau / h \tag{3.41 c}$$

Where i is the complex value $\sqrt{-1}$, $\Phi(\phi_n)$ is the complex-valued ADR, ϕ_n is the numerical wave number, N is the number of points used to resolve the initial sinusoidal wave, and h is the spatial discretization increment. The real-valued component of the ADR is a measure of the dispersive (wave speed) error, while the imaginary-valued component is a measure of the dissipative error. As numerical error is cumulative over potentially hundreds of wave-lengths it is undesirable to have these error measures exceed a value of 0.005.

This analysis was first conducted for a fundamental resolution of $N = 24.25$, and subsequently for several integer harmonics. Analyses for higher resolutions are

not shown, as all of the schemes considered are spectrally accurate for N > 25. It is also notable that the ADR analysis is conducted using non-integer value resolutions. This is done to reduce any influence that initial position of the wave profile relative to the gird nodes might have. For integer value resolutions the grid alignment is the same for each wavelength, while for non-integer resolutions the alignment varies. For this purpose a completely arbitrary resolution is ideal; however, to obtain accurate results from the Fourier transform used in Equation (3.41 a) an integer number of wavelengths is needed in the analysis region. As a result the resolution of 24.25, which contains exactly 97 nodes in four wavelengths, was used as an acceptable compromise.

For all calculations the fluid properties were $c_o = 1.0$, $\rho_o = 1.0$. The grid resolution was $\Delta x = 0.01$, and ϕ_n was modified by increasing the frequency of the initial wave profile:

$$u_o(x_i) = \sin\left(\frac{\phi_n}{\Delta x}(x_i - x_o) - \theta\right) \tag{3.42}$$

where x_o is the left boundary of the analysis region and $\theta = \pi/6$. Figure 14 plots the real valued component of the ADR for the r =3 and r = *4* WENO schemes. Points that lie on the spectrally accurate line, $\mathrm{Re}[\Phi(\phi)] = \phi$, indicate the wave is well resolved and will propagate with the correct wave speed. Also included in Figure 14 for comparison is the analytically obtained ADR of a 7^{th} order polynomial fixed stencil scheme. As expected the WENO schemes are less accurate for high wave numbers (low resolutions) than their fixed stencil equivalent. In general it can also be seen the $r = 4$ schemes perform better than the $r = 3$ schemes. Importantly, Figure 14 shows the WENO-Z smoothness measure provides slightly better properties than the standard smoothness measure.

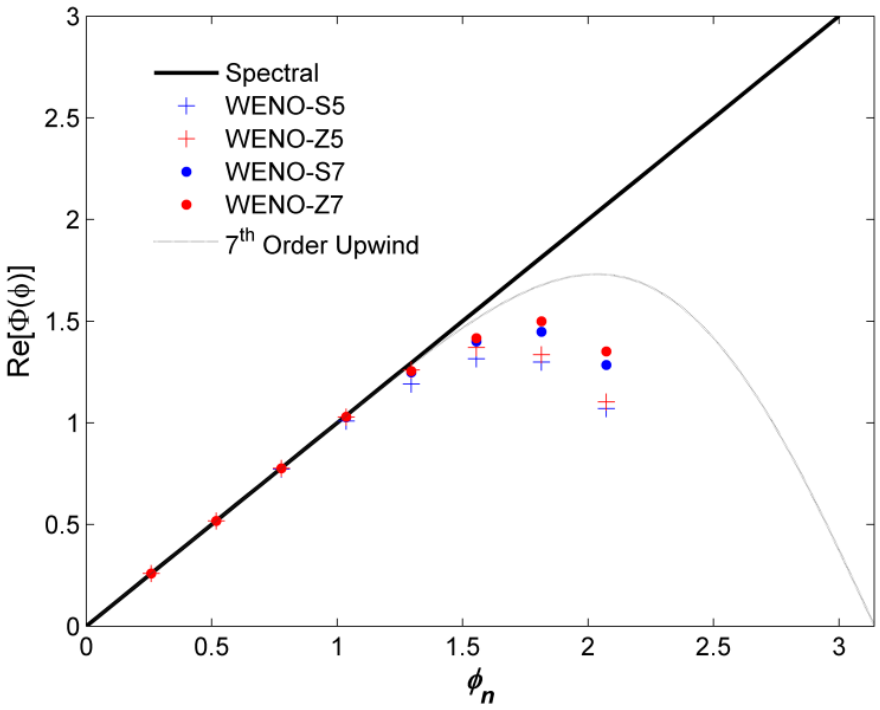

Figure 14: Wave speed as a function of frequency for several shock capturing numerical schemes. The schemes are denoted: WENO-S5 and S7 for the r =3 (5th order) and r = 4 (7th order) schemes using the smoothness measure from Jiang and Shu [36], WENO-Z5 and Z7 for the r =3 (5th order) and r = 4 (7th order) schemes using the modified smoothness measure of Borges and Carmona et al. [9].

While the results shown in Figure 14 give a good indication of general properties, it is the small deviations from spectral accuracy that are not visibly discernable that are most interesting. Table 3 summarizes the dispersive error of the WENO schemes, while Table 4 summarizes the dissipative error. Also included in this analysis for comparison are the ADR properties of a 2nd order TVD scheme using the van-Leer gradient limiter [43].

Table 3: Summarized wave speed error as a function of frequency for several shock capturing numerical schemes. Schemes designations are the same as in Figure 14, with the addition of U7 for the 7th order fixed stencil scheme, and TVD for the 2nd order TVD scheme.

		$\mathrm{Re}\{\Phi(\phi_n)\} - \phi_n$					
N	ϕ_n	TVD	U7	WENO-S5	WENO-S7	WENO-Z5	WENO-Z7
24.25	0.26	0.0014	0.0000	0.0000	0.0000	0.0000	0.0000
12.13	0.52	0.0090	0.0000	-0.0004	0.0000	-0.0001	0.0000
8.08	0.78	0.0189	-0.0001	-0.0048	-0.0010	-0.0012	-0.0003
6.06	1.04	0.0104	-0.0016	-0.0274	-0.0092	-0.0081	-0.0069
4.85	1.30	-0.0516	-0.0103	-0.1046	-0.0471	-0.0353	-0.0408
4.04	1.55	-0.2050	-0.0434	-0.2402	-0.1550	-0.1844	-0.1381
3.46	1.81	-0.4770	-0.1366	-0.5146	-0.3658	-0.4782	-0.3141
3.03	2.07	-0.8732	-0.3442	-1.0022	-0.7880	-0.9703	-0.7212

Table 4: Summarized dissipation error as a function of frequency for several shock capturing numerical schemes.

		$\mathrm{Im}\{\Phi(\phi_n)\}$					
N	ϕ_n	TVD	U7	WENO S5	WENO S7	WENO Z5	WENO Z7
24.25	0.26	-0.0006	0.0000	0.0000	0.0000	0.0000	0.0000
12.13	0.52	-0.0110	0.0000	-0.0015	-0.0001	-0.0003	0.0000
8.08	0.78	-0.0555	-0.0004	-0.0124	-0.0027	-0.0035	-0.0009
6.06	1.04	-0.1641	-0.0033	-0.0481	-0.0193	-0.0167	-0.0137
4.85	1.30	-0.3560	-0.0161	-0.1345	-0.0730	-0.0559	-0.0617
4.04	1.55	-0.6284	-0.0535	-0.3543	-0.1726	-0.2450	-0.1556
3.46	1.81	-0.9541	-0.1353	-0.6819	-0.3327	-0.6071	-0.2945
3.03	2.07	-1.2901	-0.2750	-1.0197	-0.6687	-0.9555	-0.5517

From the reported ADR values it can be seen the 5th order WENO-Z scheme provides better spectral accuracy than the 7th order standard WENO-S scheme for resolutions greater than N = 5. As expected the TVD scheme is the most dissipative, while the 7th order WENO-Z scheme is the least. When comparing the two smoothness measures, ADR properties produced by the WENO-Z schemes are at least a factor of three better for the first three harmonics analyzed. Specifying threshold of $|\mathrm{Re}\{\Phi(\phi_n)\} - \phi_n| \leq 0.005$ for well resolved waves, it can be seen that all of the WENO schemes potentially allow for the accurate representation of three harmonics when the fundamental frequency is resolved with $N = 24.25$.

When interpreting these results it is also important to recognize limitations of the ADR analysis. As discussed by Pirozzoli [58], complex wave profiles may contain multiple harmonic components. For linear schemes this does not influence the underlying spectral accuracy; however, for the profile dependent WENO schemes this is not the case. For this reason the ADR results provide an upper bound estimate on the performance capabilities of a particular scheme, and the achieved accuracy for nonlinear wave propagation is expected to be somewhat less.

A few additional comments are now provided on issues encountered when conducting this analysis. In the procedure discussed by Pirozzoli [49] it is recommended to use $\tau \ll 1$ to minimize the influence of time discretization error, but particular values for σ are not given. As the ADR the analysis advances the solution using a single step, it is effectively using 1st order time-integration. When this 1st order time-stepping is used with the implemented high-order upwind schemes and $\sigma = 10^{-4}$, the resulting numerical error includes small amounts of positive dissipation (amplification), indicating that the schemes may be unstable. It has been found that the dissipative error became negative for all evaluated schemes once time discretization error was further reduced by choosing $\sigma = 10^{-5}$, or by using the high-order Runge-Kutta time integration discussed in Section 3.4. This indicates that the observed amplification of well resolved waves is a product of the 1st order time-stepping, and that the implemented WENO schemes, when coupled with RK time integration, are both stable and dissipative.

3.4 Runge-Kutta Time Discretization

For the $r = 3$ and $r = 4$ WENO schemes a classic 4th order Runge-Kutta (RK) algorithm is used to evolve the solution. The particular RK implementation used applies an aggregate value, L^{RK4}, to update the global solution according to:

$$\boldsymbol{U}^{n+1} = \boldsymbol{U}^{n} + \Delta t \boldsymbol{L}^{RK4}$$

$$\boldsymbol{L}^{RK4} = \frac{1}{6}\boldsymbol{L}\left(\boldsymbol{U}^{(n)}\right) + \frac{1}{3}\boldsymbol{L}\left(\boldsymbol{U}^{(1)}\right) + \frac{1}{3}\boldsymbol{L}\left(\boldsymbol{U}^{(2)}\right) + \frac{1}{6}\boldsymbol{L}\left(\boldsymbol{U}^{(3)}\right)$$

$$\boldsymbol{U}^{(1)} = \boldsymbol{U}^{n} + \frac{1}{2}\Delta t \boldsymbol{L}(\boldsymbol{U}^{n}) \tag{3.43}$$

$$\boldsymbol{U}^{(2)} = \boldsymbol{U}^{n} + \frac{1}{2}\Delta t \boldsymbol{L}\left(\boldsymbol{U}^{(1)}\right)$$

$$\boldsymbol{U}^{(3)} = \boldsymbol{U}^{n} + \Delta t \boldsymbol{L}\left(\boldsymbol{U}^{(2)}\right)$$

Similar to the spectral properties of the reconstruction schemes, there is an important distinction between formal order of accuracy and spectral accuracy of the RK time discretization. The discussion to follow is based on the work by Hu et al. [35], which is strongly recommended as additional reading. Importantly, it is shown the allowable values for Δt are considerably smaller when numerical dissipation and dispersion are to be kept to a negligible amount.

Using a simplified notation, Runge-Kutta schemes can be formulated as [35]:

$$\boldsymbol{U}^{n+1} = \boldsymbol{U}^{n} + \Delta t \sum_{i=0}^{p-1} w_i L\left(U^{(i)}\right) \tag{3.44}$$

where p is the number of stages, and $w = [1/6,\ 1/3,\ 1/3,\ 1/6]$ and $p = 4$ for the classical RK4 scheme. By applying a spatial Fourier transform to $\boldsymbol{U}^{n}$ and $\boldsymbol{U}^{n+1}$, the spectral properties of solution advanced in time can be compared to the initial one [35]:

$$\widetilde{\boldsymbol{U}}_k^{n+1} = \widetilde{\boldsymbol{U}}_k^{n}\left(1 + \sum_{j=1}^{p} c_j(-\boldsymbol{i}c_o k^{*}\Delta t)^{j}\right) \tag{3.45 a}$$

$$r = \frac{\widetilde{\boldsymbol{U}}_k^{n+1}}{\widetilde{\boldsymbol{U}}_k^n} = 1 + \sum_{j=1}^{p} c_j(-\boldsymbol{i}c_o k^* \Delta t)^j \tag{3.45 b}$$

$$r_e = e^{-ick^*\Delta t} \tag{3.45 c}$$

where $\widetilde{\boldsymbol{U}}_k^n$ is the k frequency of the Fourier transform of $\boldsymbol{U}^n$, and the coefficients c_j = [1, ½! , $^1/_{3!}$, ¼!] are related to w_i in Equation (3.44). The value k^* is the effective wave-number produced by the spatial discretization. For the adaptive WENO schemes this value cannot be analytically determined, but it can be estimated using the approximate dispersion relation (ADR) discussed in Section 3.3, where and relation between k^* and $\boldsymbol{\phi}_n$ is simply:

$$k^* = \frac{\phi_n^*}{\Delta x} \tag{3.46}$$

In Equation (3.45) the quantity r is the *numerical amplification factor*, as it represents the total change in amplitude or phase of a particular frequency in the solution. The exact amplification factor, r_e, includes only errors induced by the spatial discretization. To specify the spectral accuracy of a particular Runge-Kutta scheme, the ratio r/r_e, can be numerically evaluated to produce the aggregate values:

$$\frac{r}{r_e} = |r|e^{-\boldsymbol{i}\delta} \tag{3.47 a}$$

$$|r| = \sqrt{\mathrm{Re}\{{}^r/_{r_e}\}^2 + \mathrm{Im}\{{}^r/_{r_e}\}^2} \tag{3.47 b}$$

$$\tan\delta = \left(\frac{\mathrm{Im}\{{}^r/_{r_e}\}}{\mathrm{Re}\{{}^r/_{r_e}\}}\right) \tag{3.47 c}$$

For accurate wave propagation the magnitude error, $|r|$, should be within a small tolerance of 1.0, and the phase error, δ, should be within a small tolerance of 0.0. Hu et al. [35] choose $|\delta| > 0.001$ as the limit for accurate wave propagation. From Figure 15, which plots $|r|$ and δ for the classic RK4 scheme, it can be seen that the phase error is only below this threshold for $c_o k^* \Delta t \leq 0.67$.

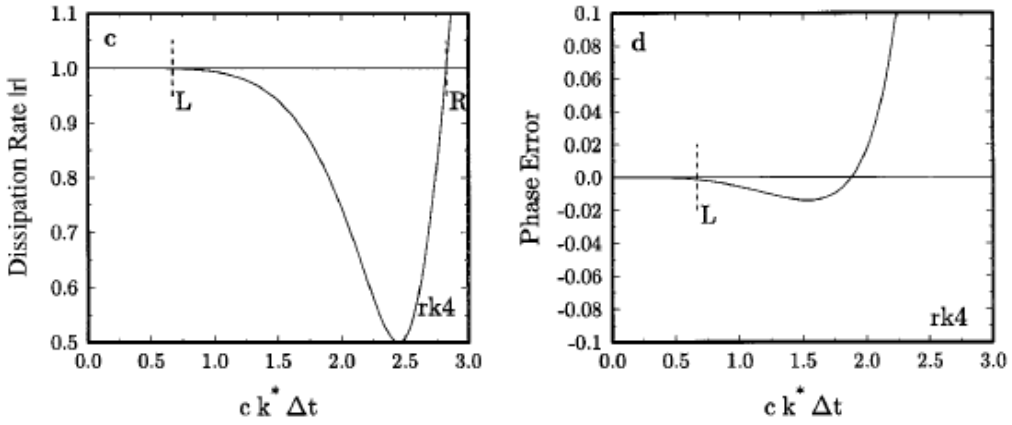

Figure 15: Dissipation and phase error of the four-stage Runge-Kutta scheme. Reproduced from [35].

From the analysis shown in Figure 15 it can be seen that the spectral resolution is related to both the time step, Δt, and the effective wave number, k^*. For a scheme with good spectral properties k^* should be within close tolerance of the true wave number, k. For this tolerance Hu et at. [35] specify a deviation of less than 0.005. From the data presented in Table 3, it is estimated that the threshold, $|\mathrm{Re}\{\Phi(\phi_n)\} - \phi_n| \leq 0.005$, is exceeded for $\phi_n > 1.0$ with both the r =3 and r = 4 WENO schemes. By using Equation (3.46) to translate ϕ_n into equivalent k^* values, the time steps needed for good spectral accuracy are determined according to:

$$c_o k_c^* \Delta t \leq 0.67 \tag{3.48}$$

where $k_c^* = 1.0$ for the discussed WENO schemes.

To produce a RK scheme with better spectral accuracy properties Hu et al. [35] optimize the values of c_j in Equation (3.45) to increase the error thresholds shown in Figure 15. This procedure produces schemes that have higher accuracy limits but lower formal orders of accuracy. The spectrally optimized four-step algorithm has a better accuracy limit of, $ck^*\Delta t < 0.85$; however, the scheme has only second order formal accuracy. If 4th order accuracy is to be maintained, the optimized six-stage scheme can be used, which also allows for a much higher accuracy limit of $ck^*\Delta t < 1.75$. Unless otherwise noted, the classic four-step RK scheme has been used with suitably small values of Δt for all calculations in this thesis. At present the six-step algorithm has not been implemented, as the calculations performed do not demonstrate the need for larger allowable time steps. In future works when the

model is applied to scenarios that are more computationally demanding, the six-step procedure is worth considering as it may give a 40% reduction in the total number of required operations for similar spectral accuracy.

3.5 Boundary Conditions

For the one-dimensional wave propagation problems currently studied there is only one boundary condition of practical interest to discuss. This is the *periodic driven boundary* used to introduce sinusoidal waves into the domain for both the linear and non-linear models. As analytical solutions are primarily specified using fluid velocity, the numerical boundary condition is defined as:

$$u_o = \sin\left(\omega\left(\frac{x - x_o}{c_o} - t\right) + \phi\right) \tag{3.49}$$

where the location x_o is taken to be the boundary face of the domain, and unless otherwise noted x_o = 0.0. This simple boundary condition is intended only to introduce incoming waves, and is not intended to interact with outgoing waves in a physically accurate manner. From the linear acoustic plane wave condition the fluid density is set according to:

$$\rho' = u_o \frac{\rho_o}{c_o} \tag{3.50}$$

These conditions are applied to an external boundary cell and to the associated boundary face. Although no formal efforts to quantify the order of accuracy of this method are made here, it can be stated that the first internal cell can use at most the r = 2 WENO scheme for reconstruction. As the cumulative error of long propagation is of primary interest in this study, this simplified approach to the boundary condition is deemed an acceptable approximation.

3.6 Discussion

Having described in detail the use of finite volume WENO spatial reconstructions, it is worthwhile to note the use of WENO methods is not typical for many applications in acoustics. As discussed, the WENO reconstruction scheme can be

categorized as an upwind method [70], and as a result the numerical error contains both dissipative and dispersive components [58]. In linear acoustics central finite difference schemes are more often used as they produce only dispersive errors [46]; thus adequately resolved waves can be propagated without dissipation over long distances. For nonlinear acoustic problems central finite difference methods are also popular when the physical solution is known a priori to not contain shocks or discontinuities.

Centered finite-difference methods can also be used for nonlinear ultrasound, such as in the work by Ginter et al. [29], when used with spectral filtering and sufficient resolution to allow shock waves to be smoothly represented in the numerical domain. One of the primary challenges in the current work is to reduce the resolution required to propagate the shocked saw-tooth wave profile. Resolving waves with several hundred cells (allowing shocks to be approximated as steep but smooth gradients) is not a practical option when considering the eventual need for three-dimensional simulations containing hundreds or thousands of wavelengths in the domain. It is for this reason the present work is centered on the use of WENO methods which allow for the oscillation free inclusion of shock waves in the solution while using reasonably low spatial resolutions.

A valid criticism on the use of explicit polynomial WENO methods in the current work is the availability of shock-capturing schemes based on the implicit polynomial methods made popular by Lele [46]. The implicit polynomials used in these methods are known to possess much better wave propagation properties than explicit polynomial of equivalent order. However, the simple implicit spatial schemes are not suitable for problems containing discontinuities, and extra considerations are needed to obtain shock-capturing capability. A brief review of shock-capturing implicit polynomial methods reveals that these schemes may rely on TVD limiters [21], or hybrid algorithms that incorporate ENO or WENO methods, [16, 57, 62, 65, 67], to achieve shock capturing capability. Implicit polynomial methods that use artificial viscosity to prevent numerical oscillations also exist, but were not further investigated. Referring to [58], it can be shown that the spectral properties of the compact scheme incorporating a TVD limiter

[21] are not better than those of the explicit WENO schemes.

When considering hybrid schemes that include some aspects of ENO or WENO methodology, the algorithm complexity and development time are increased considerably over the use of a single methodology. Hybrid schemes typically included all aspects of both underlying schemes as well as additional algorithms to determine when each is applied. It is this added complexity of hybrid methods that primarily limits the current work's focus to the basic WENO schemes. It is likely the available hybrid methods offer improved wave propagation accuracy in smooth regions, and may also offer improved accuracy for the important post shock region. However, the thorough understanding of the WENO schemes resolving capabilities for nonlinear acoustic wave propagation provided by the current work, in particular the influence of different smoothness measures, is a valuable result that will remain relevant to possible hybrid scheme developments. Furthermore, as is shown later, the basic WENO scheme is capable of capturing many of the phenomena of interest at reasonably low resolutions, thus the added complexity and development may not be required. If future applications of the developed model would reveal limitations of its capabilities, a recommended starting point is to use the *Conservative Hybrid Compact-WENO Scheme* developed in [57], or to use the recent *Generalized Finite Compact Difference Scheme* by Shen and Zha [67] which incorporates a 5^{th} order WENO algorithm.

4 Verification of the Numerical Model

In this chapter numerical results are presented to verify the implemented numerical model and to evaluate its accuracy. Calculations performed with the linear acoustic governing equations are used to verify the scheme by demonstrating grid convergence to an analytical wave propagation solution. Calculations with the linear acoustic equations are also used to verify that the modified HLLC Riemann solver discussed in Subsection 3.2.4 correctly represents wave transmission and reflection at material interfaces. Furthermore, performance of the numerical model is demonstrated using a series of nonlinear plane wave calculations. From these calculations the models accuracy is thoroughly evaluated with 25 and 50 point resolutions for the fundamental wavelength. The models accurately captures the fundamental and second harmonic propagation, but the model fails to capture third and higher harmonics for the resolutions considered. In all discussions to follow the $r = 3$ and $r = 4$ schemes using the standard smoothness measure [36] are designated WENO-S5 and WENO-S7, while the $r = 3$ and $r = 4$ schemes using the low-dissipation smoothness measure [9] are designated WENO-Z5 and WENO-Z7.

4.1 Grid Convergence for the Linear Acoustic Model

To verify grid convergence of the numerical model a simple linear wave propagation test has been used. For each calculation performed the initial condition and analytical solution are:

$$u_o(x) = \sin\left(2\pi f \frac{x}{c_o}\right) \tag{4.1}$$

$$u_{exact} = \sin\left(2\pi f \left[t - \frac{x}{c_o}\right]\right) \tag{4.2}$$

where f is the analysis frequency the fluid properties are $c_o = 1.0$, $\rho_o = 1.0$, and the perturbed density is set according to the linear relation $\rho' = u_o \rho_o / c_o$. In the calculations shown below $f = 0.5$ s^{-1} is used to give a wavelength of 1.0 on the computational domain, which contains twenty wavelengths in total. Analysis of the numerical solution is conducted using ten wavelengths from an internal region

of the domain to avoid boundary effects. Additionally, the analysis is conducted at time t = 1.0, which corresponds to a propagation distance of 1/π wavelengths. From the numerical models solution the L_1 and L_{inf} error norms are calculated as:

$$L_1 = \frac{1}{N}\sum_{i=1}^{N}\|u_i - u_{exact}(x_i)\| \tag{4.3}$$

$$L_{inf} = \max\|u_i - u_{exact}(x_i)\| \tag{4.4}$$

The order of grid convergence for each increment in resolution is then defined according to:

$$R = \frac{\log(L(N_b)/L(N_a))}{\log(\Delta x_b/\Delta x_a)} \tag{4.5}$$

where $L(N_a)$ and $L(N_b)$ are the error norms at the resolutions N_a and N_b, and Δx_a and Δx_a are the spatial discretization increments at the resolutions N_a and N_b. When evaluating the convergence rate between two resolutions values are specified for $N_b > N_a$. For all calculations a CFL condition of 0.5 is used to ensure good spectral accuracy with the RK4 time integration. For reference an additional calculation series is also conducted using the low-dispersion and low-dissipation RK algorithm introduced in Section 3.4.

Results from all test series are plotted in Figure 16, while Table 5 through Table 9 gives the numerical values. The following discussion focuses on the L_1 error norm results but the L_{inf} results are also available in the tables. In general, all of the schemes achieve 5th order grid convergence, and the WENO-Z smoothness measure provides notably lower error magnitudes compared to the WENO-S results. Both the WENO-S5 and the WENO-Z5 schemes show consistent 5th order convergence. As the RK time integration algorithm is only 4th order accurate, the observed 5th order convergence rates are possible due to the near spectral accuracy produced by the CFL = 0.5 condition. Results from the low-dissipation RK4 algorithm show similar 5th order convergence rates for low resolutions when spatial discretization error dominates. For higher resolutions spatial error is reduced and the underlying second order convergence of the time discretization becomes evident.

The lowest error magnitudes and highest convergence rates were achieved using the r = 4 WENO schemes (WENO-S7 and WENO-Z7). For the WENO-S7 scheme a relatively consistent 6^{th} order grid convergence is observed. This gird convergence, which is less than the theoretical 7^{th} order permitted by the r = 4 stencil, can be attributed to the weighting mechanism in the WENO-S7 scheme. The WENO-Z7 scheme initially displays 7^{th} convergence, and then displays 8^{th} hyper-convergence between the resolutions 20 and 40 points per wave. The appearance of hyper-convergent behavior is not further investigated here, but some discussion on the topic is available in [9]. For high resolutions (> 40 points per wavelength) the WENO-Z7 scheme is reduced to 4^{th} order accuracy as the time discretization error from the RK4 scheme begins to dominate.

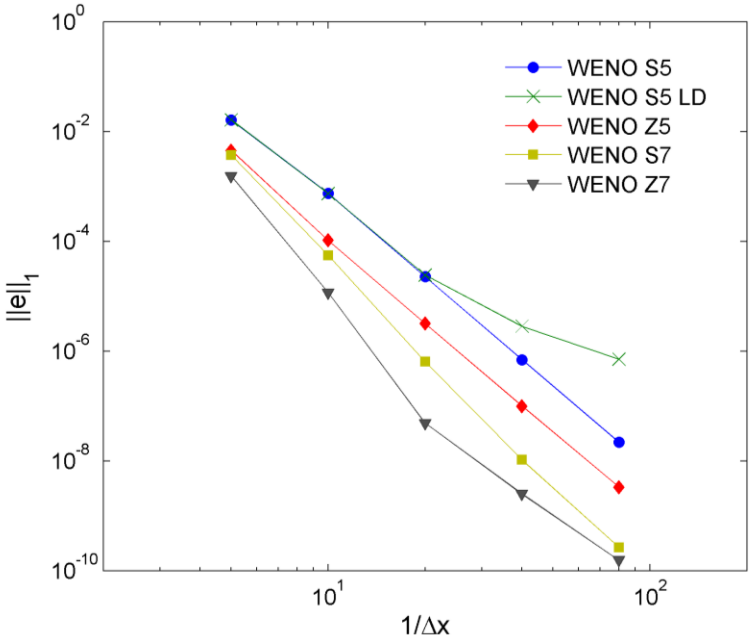

Figure 16: L_1 error norms for schemes in the developed numerical model. Designations in the legend are consistent with those in the text, with the addition of *LD* to designate used of the low-dissipation RK4 algorithm from [35].

Table 5: Grid convergence for WENO-S5 reconstruction with HLL flux and RK4 time integration.

N	L_1	R_1	L_{inf}	R_{inf}
10	1.61E-02		2.51E-02	
20	7.44E-04	4.44	1.33E-03	4.24
40	2.26E-05	5.04	4.77E-05	4.80
80	6.98E-07	5.02	1.43E-06	5.06
160	2.18E-08	5.00	4.41E-08	5.02

Table 6: Grid convergence for WENO-S5 reconstruction with HLL flux and low-dispersion low-dissipation RK4 time integration.

N	L_1	R_1	L_{inf}	R_{inf}
10	1.62E-02		2.50E-02	
20	7.39E-04	4.45	1.38E-03	4.18
40	2.42E-05	4.93	5.41E-05	4.67
80	2.84E-06	3.09	4.53E-06	3.58
160	7.07E-07	2.00	1.11E-06	2.03

Table 7: Grid convergence for WENO-Z5 reconstruction with HLL flux and RK4 time integration.

N	L_1	R_1	L_{inf}	R_{inf}
10	4.51E-03		1.23E-02	
20	1.04E-04	5.44	1.56E-04	6.30
40	3.18E-06	5.03	4.99E-06	4.96
80	9.97E-08	4.99	1.57E-07	4.99
160	3.31E-09	4.91	1.06E-08	3.89

Table 8: Grid convergence for WENO-S7 reconstruction with HLL flux and RK4 time integration.

N	L_1	R_1	L_{inf}	R_{inf}
10	3.69E-03		1.17E-02	
20	5.47E-05	6.08	1.32E-04	6.47
40	6.41E-07	6.41	3.13E-06	5.40
80	1.04E-08	5.95	8.52E-08	5.20
160	2.67E-10	5.29	2.38E-09	5.16

Table 9: Grid convergence for WENO Z7 reconstruction with HLL flux and RK4 time integration.

N	L_1	R_1	L_{inf}	R_{inf}
10	1.53E-03		1.01E-02	
20	1.15E-05	7.06	9.80E-05	6.68
40	4.85E-08	7.89	1.82E-07	9.08
80	2.49E-09	4.28	3.91E-09	5.54
160	1.55E-10	4.01	2.43E-10	4.01

4.2 Verification of Acoustic Wave Reflection

To demonstrate the ability of the HLLC scheme to correctly solve wave reflection and transmission at a material interface, a test calculation identical to the one used in [47] has been carried out. As shown in the upper plot of Figure 17 the problem uses an initially stationary pressure disturbance to generate both left-moving and right-moving waves. The initial profile is given by [47]:

$$p_o(x) = \begin{cases} \bar{p}\sqrt{1-\left(\frac{x-x_o}{\bar{x}}\right)^2} & \text{if } |x-x_o| < \bar{x} \\ 0 & \text{otherwise} \end{cases} \tag{4.6}$$

where x_o = 0.4, $\bar{x} = 0.075$, and $\bar{p} = 0.2$. From this initial profile, the right propagating eventually interacts with a material discontinuity located at x = 0.6, producing a reflected and a transmitted wave. At the discontinuity the linear acoustic material properties changes from ($c_{o,L}$ = 1.0, $\rho_{o,L}$ = 1.0) to ($c_{o,R}$ = 0.5, $\rho_{o,R}$ = 4.0) for an impedance ratio of 2.0.

Along with the modified HLLC flux solver the computational model uses WENO-Z5 spatial reconstruction and the standard 4th order Runge-Kutta time discretization with a CFL condition of 0.70. A computational grid resolution of Δx = 0.05 is equivalent to that in the calculation [47].

The lower left and right plots of Figure 17 show the computational results (discrete points) against the analytical solution (solid lines). From the quality of agreement it is evident the wave reflection and transmission is properly reproduced by the implemented HLLC solver.

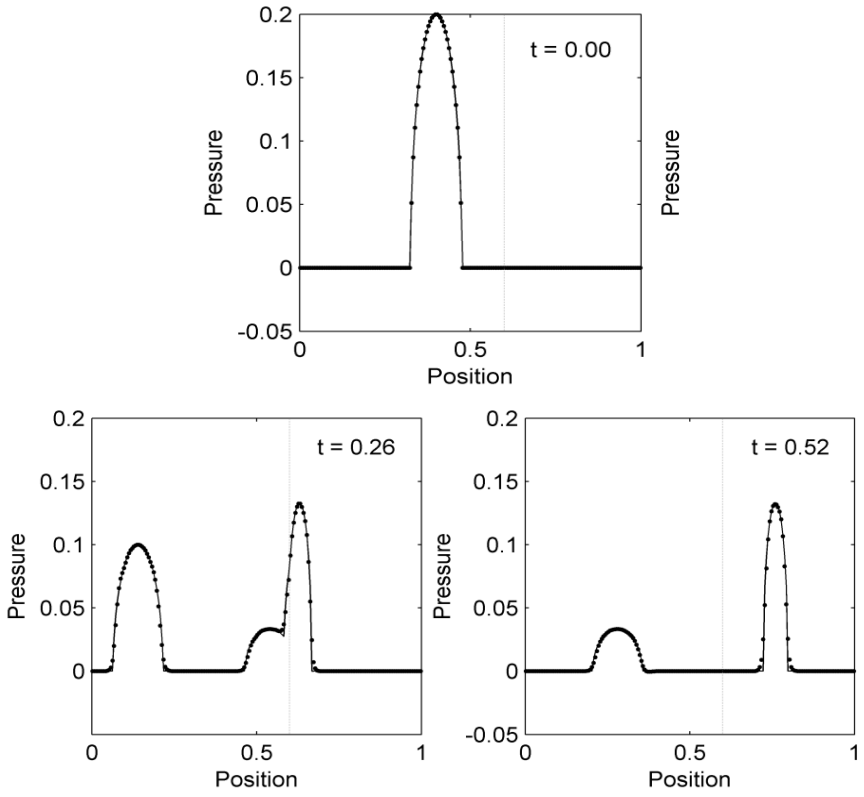

Figure 17: Verification of acoustic wave reflection. Analytical solution given by solid line, computed solution shown by discrete points.

4.3 Harmonic Generation for Nonlinear Wave Propagation

To evaluate the developed numerical models ability to accurately calculate the harmonic profiles of nonlinear ultrasonic beams a series of plane wave calculations are conducted. Although practical applications in biomedical ultrasound require two or three dimensional analysis, the fundamental resolving properties of the numerical model are well illustrated using this simplified approach. Importantly, the presented numerical results presented include regions of the domain before and after the initial shock formation. The accurate propagation of shock wave fronts is a more significant challenge than capturing of the early stage wave distortion, and accurate representation of this behavior is critically important for the simulation of WPC microscopy and harmonic imaging. This importance is best realized when considering the co-focal WPC scenario depicted in Figure 4. In this configuration shocks are most readily developed at

the focal location of the conjugate beam. Their distortion or excessive damping during propagation back to the initial transducer could diminish the predictive capability for harmonic content in conjugate beams.

4.3.1 Acoustic Shock at 10 Wavelengths

The first test scenario uses a relatively strong plane wave with the velocity amplitude chosen to achieve shock formation after ten wavelengths. The analytical solution to this scenario is obtained using the method of characteristics with the progressive wave equation given in Section 1.2. For simplicity, a driving frequency of $\omega = 10$ is used with normalized fluid properties of, $c_o = 1.0$, $\rho_o = 1.0$. The quantity of $\gamma = 6.0$ was chosen to correspond to distilled water at 20^oC [8]. For all calculations a CFL condition of 0.5 is specified. In the numerical model waves are introduced into the domain using the periodic boundary condition described in Section 3.5; otherwise the domain is initially at an ambient state.

A spatial resolution of 50 points per wave is used. With this relatively high fundamental resolution applied to such a short propagation distance the model is expected to perform well. Accordingly, these results are presented primarily to demonstrate that the nonlinear numerical model is fully capable of producing results consistent with the analytical solution.

As a point of reference, numerical results for standard 1^{st} and 2^{nd} order methods are also shown. The 2^{nd} order scheme utilizes a Van-Leer Non-Smooth gradient limiter for total variation diminishing (TVD) properties and 2^{nd} order Runge-Kutta time integration. Figure 18 plots the results obtained using the described WENO-Z5 schemes against these points of reference. From these results it can be seen that the WENO-Z5 scheme resolves the distorted wave profile extremely well, while the lower-order schemes are too dissipative to produce accurate results. Although not shown, results for this test with the WENO-S5 scheme are slightly more dissipative, while results obtained with the WENO-S7 and WENO-Z7 schemes have slightly improve accuracy.

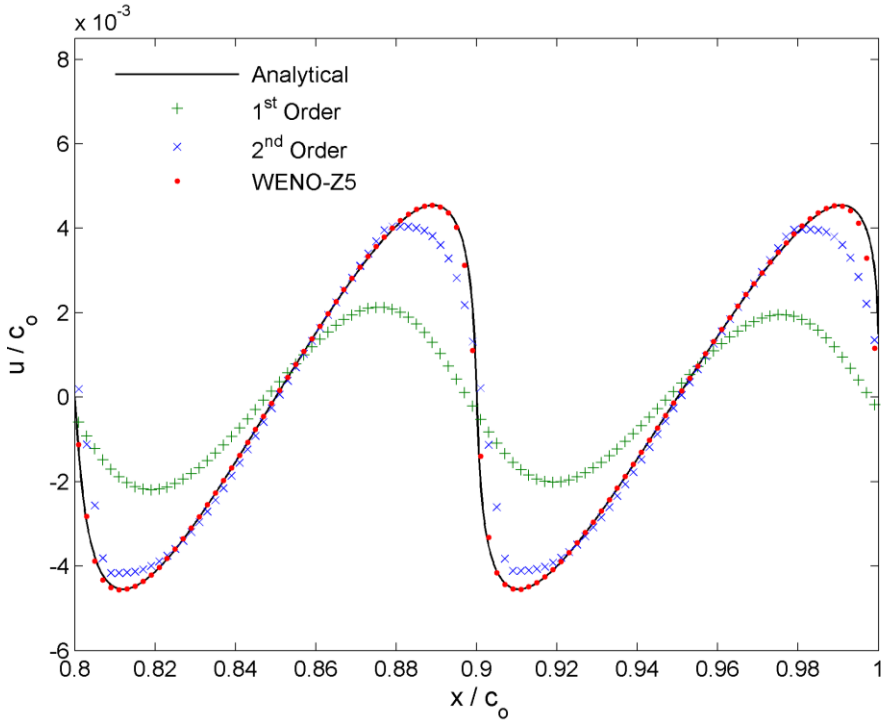

Figure 18: Nonlinear wave profiles from three numerical schemes. Shock formation occurs at ten wavelengths, $x/c_o = 1.0$.

4.3.2 Acoustic Shock at 50 Wavelengths

The second test scenario represents a 1 MHz wave propagating into a fluid with the properties of distilled water at 20°C. This test scenario is used to evaluate the evolution of the harmonic profile over an intermediate propagation distance, where the initial wave amplitude is selected to achieve shock formation at 50 wavelengths. At a frequency of 1 MHz this corresponds to a distance of 15 cm. If instead a frequency of 10 MHz is considered, such as is the case in many application of acoustic WPC, this distance would become 15 mm. While this distance is not representative of full analysis domains, it is consistent with the size of high intensity focal regions in conjugate beams [13], thus the numerical results are relevant to applied ultrasonic WPC.

Calculations are performed at the resolutions of 50 and 25 cells per fundamental wavelength. At 50 cell fundamental resolution there are 25 points for the 2nd harmonic, 17 points for the 3rd harmonic, 12.5 points per 4th harmonic, and five points for the 5th harmonic. Recalling that for well resolved waves the dispersive

error should be, $|\mathrm{Re}\{\Phi(\phi_n)\} - \phi_n| \leq 0.005$, and the dissipative error should be, $\mathrm{Im}\{\Phi(\phi_n)\} \leq 0.005$, the ADR analysis shown in Table 3 gives estimates of which harmonics in a distorting wave profile will be resolved. In Table 3 it is shown that the WENO-S7, WENO-Z5 and WENO-Z7 schemes will resolve waves that have more than eight points of resolution. This value corresponds to four resolved harmonics when the fundamental resolution is 50 points. Similar consideration is given to waves with 25 cells in the fundamental wavelength to show that up to three resolved harmonics are possible in the second calculation series.

Once again, a 2^{nd} order TVD scheme result is also presented as reference to evaluate the WENO schemes performance. Additionally, at the 25 cell resolution a fixed-stencil 7^{th} order spatial reconstruction scheme is used to provide a benchmark result for the performance of conventional high order schemes. To give a fair comparison in the post shock region, unsupported harmonics were dampened from the high order result using the spatial filter described in [29].

Analysis is conducted by comparing Fourier coefficients from numerical results against the analytical *Fay-Fubini* solution given in Chapter 1. Fourier analysis of the numerical results is performed using ten periods of time history data from each of the discrete locations shown in Figure 19 and Figure 20. Results for the 50 cell resolution calculations are plotted Figure 19.

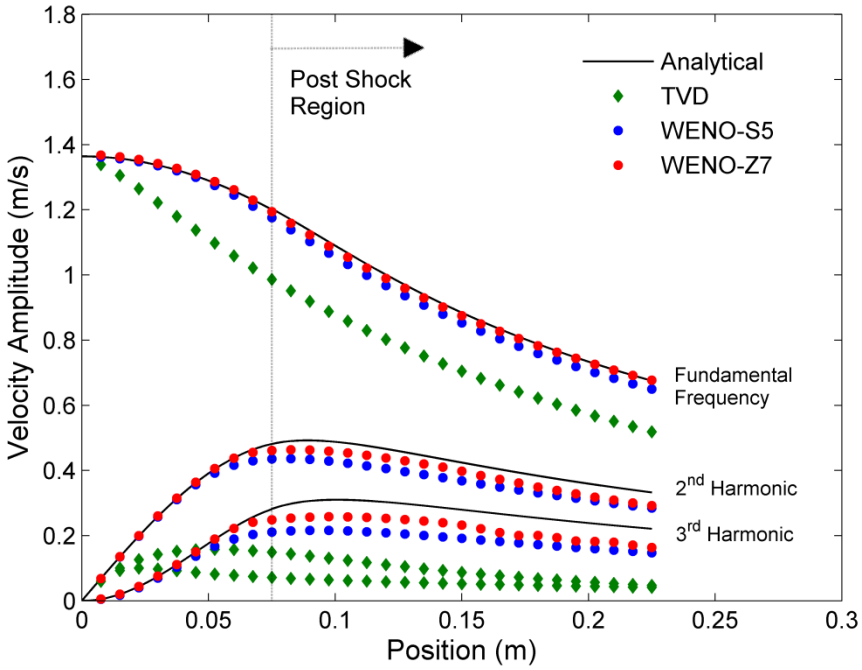

Figure 19: Harmonic profiles before and after acoustic shock formation. Shock formation at 50 wavelengths, grid resolution of 50 points per wave.

At the 50 cell resolution all of the WENO schemes are capable of resolving the harmonic profile of the distorting wave. As expected the the 2nd order TVD scheme produces results that are far more dissipative that the WENO schemes. Specifically shown in Figure 19 are the least accurate WENO-S5 result and the most accurate WENO-Z7 result. As the WENO-Z7 result does not appreciably improve the numerical results it is concluded the WENO-S5 or WENO-Z5 schemes are sufficient when 50 cells per fundamental wavelength are used.

In Figure 20, the results for the 25 cell per fundamental wavelength resolution are presented. The best numerical result in this scenario is obtained using the WENO-S7 scheme. Although not shown, the WENO-Z7 scheme admitted slight numerical oscillation into the solution, and for this reason it is not preferable to the WENO-S7 scheme when a fundamental resolution of 25 points per wave is used. As also shown in Figure 20, the WENO-S5 scheme moderately under predicts the extent of waveform steepening, resulting in and under prediction of harmonic content. Similar results are obtained using the WENO-Z5 scheme.

As expected, the 2nd order TVD scheme is highly dissipative and does not produce suitable results. Examining the results from the fixed-stencil high-order scheme

with spectral filtering, it can be seen the quality of agreement to analytical values actually exceeds the WENO results prior to the shock formation. However, after the onset of the initial shock the second and third harmonics demonstrate unphysical growth as a result of numerical oscillations originating from the shocked wave fronts. This result serves as the best justification for the use of shock capturing WENO schemes, as the conventional high-order scheme is clearly insufficient even when unsupported wave numbers are filtered using numerical dissipation.

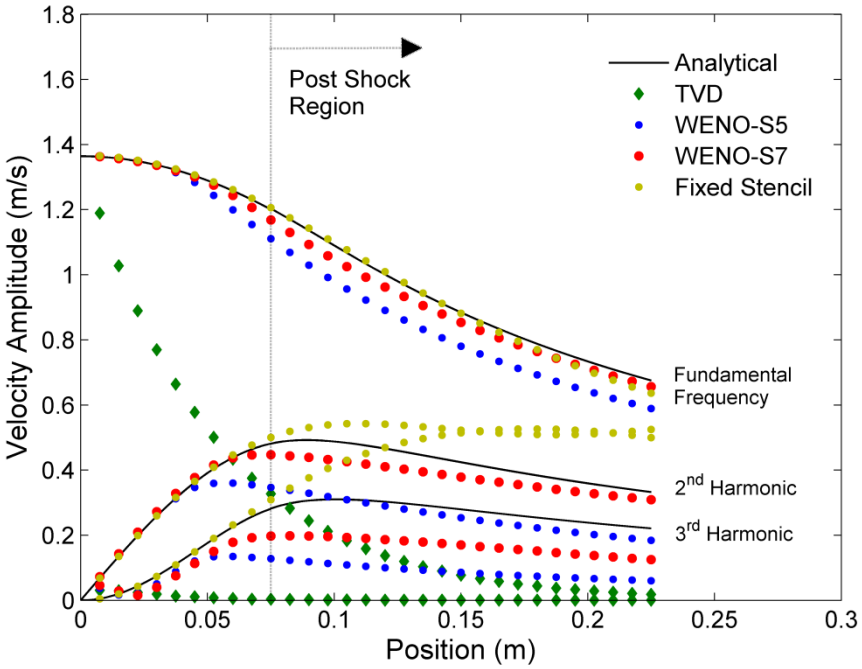

Figure 20: Harmonic profiles before and after acoustic shock formation. Shock formation at 50 wavelengths, grid resolution of 25 points per wave.

4.3.3 Acoustic Shock at 100 Wavelengths

The third test scenario uses a setup similar to the second one, but considers only the 25 cells per wave resolution, and reduces the initial amplitude to achieve shock formation at 100 wavelengths. These conditions are intended to present a more severe test of the numerical model in order to identify its functional limits. Similar to the previous test case a benchmark result was obtained using a 7^{th} order fixed-stencil reconstruction polynomial with better ADR properties.

Shown in Figure 21 are the best results, which are obtained using the WENO-S7

reconstruction scheme. Not shown are the results for the 5th order WENO schemes, which proved to be too dissipative, and the WENO-Z7 scheme, which admitted some numerical oscillation into the solution.

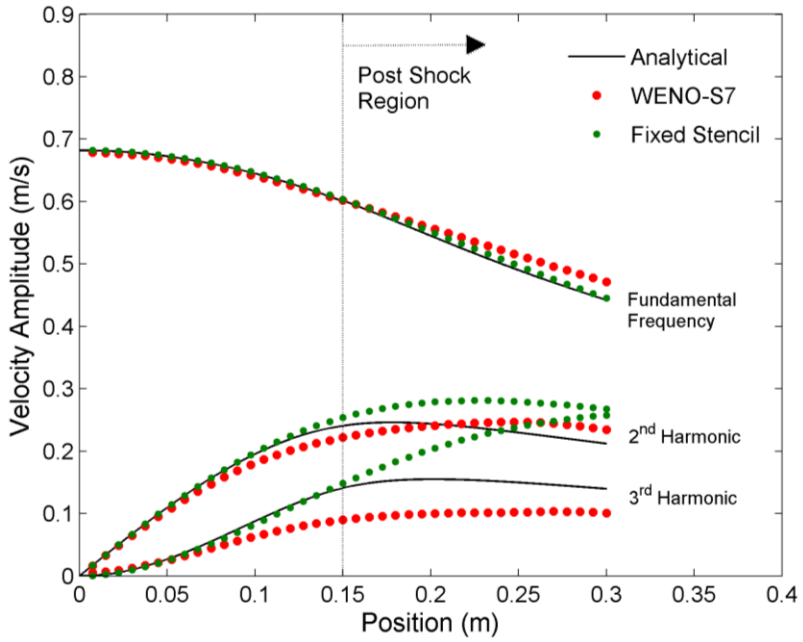

Figure 21: Harmonic profile before and after acoustic shock formation. Shock formation at 100 wavelengths, grid resolution of 25 points per wave.

From Figure 21 it can be seen the WENO-S7 scheme is able to give a reasonable representation of the fundamental frequency and the generated 2nd harmonic, but becomes slightly dissipative for the generated 3rd harmonic. It is also evident that this underrepresentation of the third harmonic produces slightly over represented fundamental and second harmonic component. Similar to the previous test case the fixed-stencil scheme outperforms the WENO-S7 scheme prior to the shock location. After the initial shock location numerical oscillations pollute the harmonic profile calculated by the fixed-stencil scheme, while the WENO-S7 result remains oscillation free. This result further demonstrates the need for the high-order WENO schemes when calculating high-amplitude sound beams containing shock wave profiles.

5 Acoustic Wave Phase Conjugation

For a general introduction to acoustic Wave Phase Conjugation (WPC) processes refer to Section 1.3. For a review of nonlinear effects in acoustic WPC refer to Section 1.4. In this chapter the physical process and governing equations of acoustic WPC are further explained. A simplified analytical solution to the conjugate wave amplification rate is also presented. Importantly, details are given on the integration of a WPC model into the developed nonlinear acoustic model. Numerical results are presented to verify the numerical implementation against the known analytical solution. Concluding the chapter is a brief investigation on the potential influence of nonlinearity in the conjugate sound beam.

5.1 Governing Equations for Paraxial WPC Conjugators

For a relatively narrow conjugator with normal incident waves the device can be modeled using a paraxial (one-dimensional) approximation. Under this assumption only longitudinal stress waves are permitted, and an analytical solution of the resonant response in the active region is available from Merlen et al. [52, 53]. The linear elastic equations within the WPC active region are:

$$\frac{\partial v}{\partial t} + c\frac{\partial \theta}{\partial x} = 0 \tag{5.1}$$

$$\frac{\partial \theta}{\partial t} + c\frac{\partial v}{\partial x} = \frac{\theta}{c}\frac{\partial c}{\partial t} \tag{5.2}$$

where v is the displacement velocity, $\theta = -\sigma_{xx}/\rho_o c$ is a normalized stress variable, and c is the longitudinal linear elastic sound speed. The right hand side of Equation (5.2) gives the source term responsible for the WPC effect in the active region. From [53] modulation of c by the externally applied magnetic field takes the form of:

$$c^2 = c_o^2[1 + m\cos(\Omega t + \phi)] \tag{5.3 a}$$

$$c = c_o\left[1 + \tfrac{1}{2}m\cos(\Omega t + \phi)\right] + O(m^2) \tag{5.3 b}$$

where Ω and ϕ are the radial frequency and phase of the magnetic field

oscillations. Equation (5.3a) most closely represents the physical process, while Equation (5.3b) is a first order approximation that can be used in the numerical model. As demonstrated through the more thorough derivation given in Appendix C, Equation (5.3a) can be used to provide an approximate form of governing Equation (5.2). The resulting expression gives the form of the stress equation that is used in the analytical solution:

$$\frac{\partial \theta}{\partial t} + c\frac{\partial v}{\partial x} = m\frac{\Omega\theta}{2}\sin(\Omega t + \phi) \tag{5.4}$$

To achieve conjugation and amplification of an incident wave, the pumping or oscillation frequency, Ω, must be double the incident wave frequency, ω [52, 53]. It is this property that allows ultrasonic WPC to be highly frequency selective. For example, by oscillating the magnetic field at a particular frequency it is possible to conjugate a particular harmonic of an incoming wave.

5.2 Partial Review of Analytical Solutions

The complete analytical solution to paraxial acoustic WPC is described in the work by Merlen and Zhang [52] and furthered by Merlen et al. [53]. The complete general solution to paraxial WPC is extensive as a variety of solution types exist depending on physical parameters and initial conditions. As a result an exhaustive presentation of the general solution is beyond the scope of this thesis. Instead, only aspects of the analytical solution relevant to calculations discussed in the present work are discusses, and the additional review of [53] is highly recommended. It is also important to note that the presented analytical solution assumes linear response in the conjugator and in the neighboring fluid. As a result, consideration of nonlinear response in the fluid is left for numerical analysis in subsequent sections.

The large physical amplification of waves achieved by WPC processes is dependent on establishing a resonant condition within the WPC active region. Analytical solutions to the WPC process are applicable for this resonant condition. Furthermore, in the analytical solution this resonant condition is defined only when the active region length is an integer multiple of a quarter

wavelength of the amplified wave. It has however, been demonstrated experimentally and numerically that resonant amplification is possible at non-integer active region lengths. With these caveats in mind, the solution variables are defined as follows:

$$w_1 = v + \theta = -Ae^{\Gamma t}\left(\sin\left(\frac{k\alpha}{4}x + \zeta_1\right)\sin\left(-\frac{k}{2}x + \frac{\Omega}{2}t + \phi_1\right) + mf_1(+x,t)\right) \quad (5.5\text{ a})$$

$$w_2 = v - \theta = Ae^{\Gamma t}\left(\sin\left(\frac{k\alpha}{4}x + \zeta_2\right)\sin\left(\frac{k}{2}x + \frac{\Omega}{2}t + \phi_2\right) - mf_1(-x,t)\right) \quad (5.5\text{ b})$$

$$\Gamma = \frac{\Omega}{8}\sqrt{m^2 + 4\alpha^2} \quad (5.6)$$

where θ is the normalized stress variable, and w_1, w_2 are characteristic variables representative of left and right moving waves. The key variables to be solved are α the standing wave length scale, and ζ the standing wave phase variable. All other variable definitions are consistent with those given in Table 11 below.

This general solution contains an exponential growth term, $Ae^{\Gamma t}$, a standing wave pattern, $\sin(\frac{1}{4}k\alpha x + \zeta_1)$ and a travelling wave term, $\sin(-\frac{1}{2}kx + \frac{1}{2}\Omega t + \phi_1)$. The relative phases of the standing wave pattern and the travelling waves are given by ζ and ϕ, respectively. The final term $mf_1(x, t)$ is of the order O(m), where $m \ll 1$, and may be neglected for approximate solutions.

In general, solutions depend on the length of the active region relative to the wavelength of the amplified waves. *Even* solutions, as defined in [53], have an even number of quarter wavelengths in the active region. This is equivalent to stating that stress oscillations at the active region boundaries are in phase or 180° out of phase. *Odd* solutions, as defined in [53], are specified to have an odd number of quarter wavelengths in the active region. This is equivalent to stating stress oscillations at the active region boundaries are 90° or 270° out of phase. Within the group of solutions belonging to the *even* type, additional distinctions are made according to the selection of:

$$\cos\left(-\frac{kL}{2} + \phi_1 - \phi_2\right) = \pm 1 \quad (5.7\text{ a})$$

$$\cos\left(\frac{kL}{2}+\phi_1-\phi_2\right)=\pm 1 \tag{5.7 b}$$

In Equation (5.7), selection of -1 leads to a *solution of the first kind*, while the selection of +1 leads to a *solution of the second kind*. The relations stem from enforcing wave reflection conditions at the boundaries of the active region. In [53] it is shown that solutions of the *first* and *second* kind differ in their intermediate stages, but they produce equivalent physical solutions. For this reason, only the *solution of the first kind* is given here. First, the key parameter, α, is solved implicitly from the following equations:

$$G(\alpha)=\frac{\sqrt{m^2-4\alpha^2}}{2\alpha}-\cot(2\arctan G_o(\alpha)) \tag{5.8 a}$$

$$G_o(\alpha)=\frac{(\tau_l+\tau_r)\cot\left(\frac{k\alpha L}{4}\right)\pm\sqrt{\left((\tau_l+\tau_r)\cot\left(\frac{k\alpha L}{4}\right)\right)^2+4\tau_l\tau_r}}{2} \tag{5.8 b}$$

which also produces two solutions for α depending on the choice of + or – in $G_o(\alpha)$, referred to as $G_o^+(\alpha)$ and $G_o^-(\alpha)$. The correct value of α is the minimum of the two solutions as this produces the dominant amplification rate. The phase of the standing waves, ζ_1 and ζ_2, depend on the previous selection of $G_o(\alpha)$. The procedure for obtaining ζ_1 and ζ_2 is as follows:

if the dominant solution stems from $G_o^+(\alpha)$: $\quad \sin(\gamma)=\frac{2\alpha}{m}, \quad \gamma\in[0,\pi/2]$ (5.9 a)

if the dominant solution stems from $G_o^-(\alpha)$: $\quad \sin(\gamma)=-\frac{2\alpha}{m}, \quad \gamma\in[\pi,3\pi/2]$ (5.9 b)

where γ is the difference between the two phases $\gamma=\zeta_2-\zeta_1$. From this, ζ_1 can be solved using the boundary conditions of the active region, arranged to give:

$$\zeta_1=\frac{k\alpha L}{8}+\tan^{-1}\left\{\frac{1}{\sin(\gamma)}\left[\left(\frac{1+\tau_l}{1-\tau_l}\right)-\cos(\gamma)\right]\right\} \tag{5.10 a}$$

$$\zeta_2=\zeta_1+\gamma \tag{5.10 b}$$

Referring to Equation (5.5), the remaining two aspects of the analytical solution are the amplitude scale, A, and the phases of the traveling waves, ϕ_1 and ϕ_2. Both of these variables depend on the initial conditions in the active region, thus a

single solution cannot be given. For the amplitude scale, A, no analytical solution is available, as for most practical applications the active region does not initially contain a resonant wave. Therefore, to obtain the amplitude scale an external reference – such as the result from a high resolution numerical simulation – must be used. Similarly, the travelling wave phases depend on the initial condition; however, once the active region resonant condition is achieved only four possible solutions are available [53], and these are given in Table 10:

Table 10: Phases of the travelling waves in analytical WPC even solutions of the first kind.

Type	ϕ_1	ϕ_2
(a)	+1/4 π	+5/4 π
(b)	-1/4 π	+7/4 π
(c)	-3/4 π	+9/4 π
(d)	-5/4 π	+11/4 π

As previously mentioned, the large amplification of conjugate waves is dependent on the establishment of a resonant condition. Physically, waves incident on an active region do not instantaneously produce conjugate waves, but instead an exponential growth process takes place where both forward propagating and conjugate waves are continuously amplified. The resonant condition is achieved only when modulation of c_o is greater than a value known as the super-critical threshold [52]:

Super-critical threshold even case:

$$m_{o,even} = \frac{8}{kL}\cot^{-1}\left(\frac{|1-\tau_l\tau_r|}{\tau_l+\tau_r}\right) \tag{5.11 a}$$

Super-critical threshold odd case:

$$m_{o,odd} = \frac{8}{kL}\cot^{-1}\left(\frac{|1-\tau_l\tau_r|}{1+\tau_l\tau_r}\right) \tag{5.11 b}$$

Although the *odd* length analytical is not discussed in this section, the supercritical threshold for *odd* length active regions is give here for use with numerical calculations. In general the *even* and *odd* solutions are qualitatively similar, differing primarily in their amplitude growth rates. Importantly, odd length conjugators have higher supercritical threshold values, thus calculations

performed with odd length conjugators must use a larger modulation depths. In both cases these thresholds represent the balance between energy input to the system and wave energy propagating out of the active region; when the rate of energy input exceeds output exponential amplitude growth occurs.

For additional clarity Figure 22 plots the WPC process from incidence of the original wave, to initial transient growth, and finally to establishment of the resonant amplification process. For modulation depths below the super-critical threshold the third state of resonant amplification does not occur.

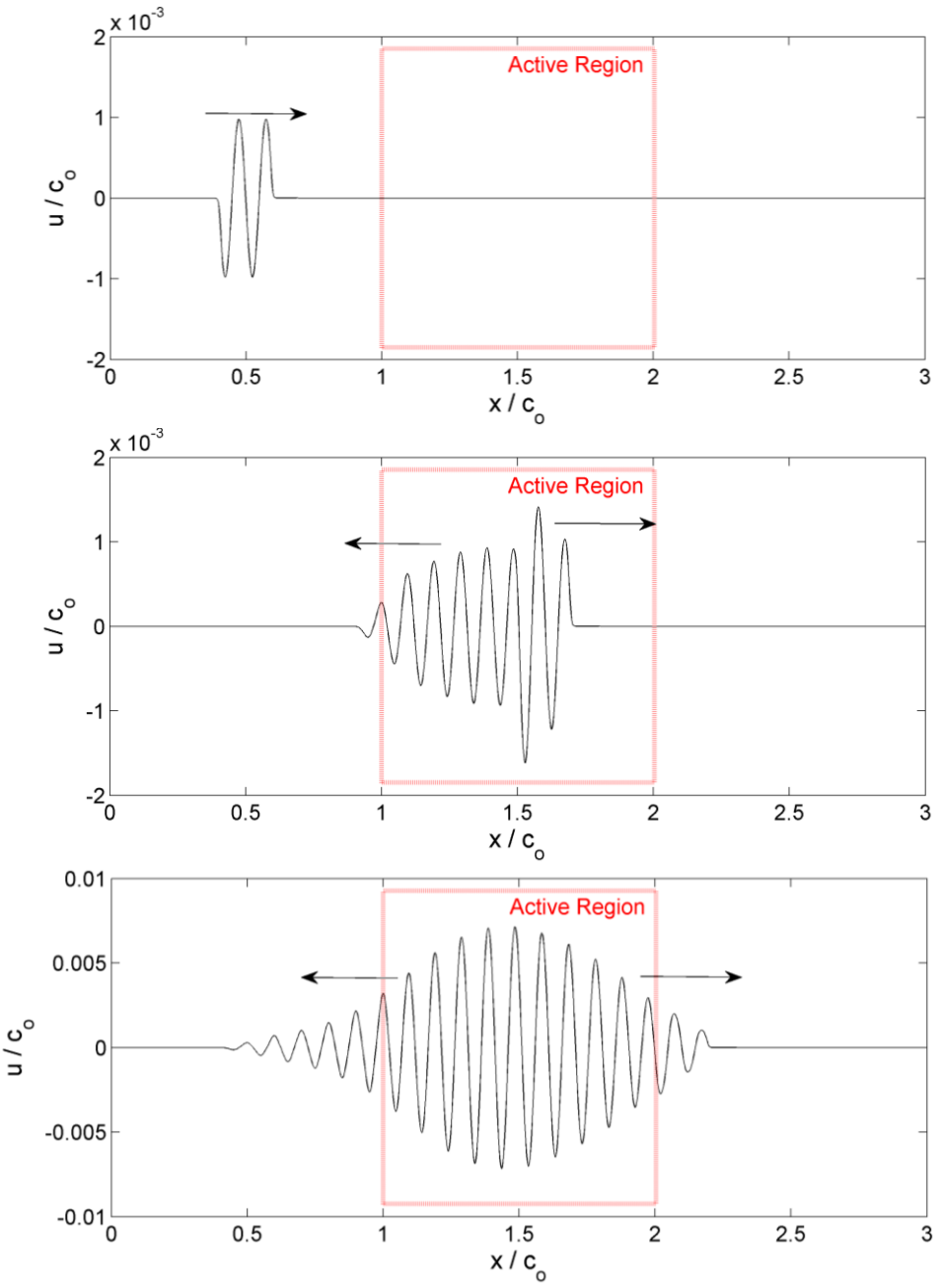

Figure 22: Production of a one-dimensional conjugate wave. Frame 1 shows the incident wave, frame 2 shows initial growth of the conjugate wave, and frame 3 show the fully formed resonant condition and transmission of the conjugate wave back into the passive fluid.

5.3 Integration of WPC in the Nonlinear Fluid Model

As discussed in Chapter 3 the developed numerical model uses a high order reconstruction-evolution finite volume scheme. Within the active region and throughout homogeneous regions of external fluid, the spatial reconstruction is performed according to Section 3.1, and fluxes are calculated using the HLL approximate Riemann solver described in Subsection 3.2.2.

To produce the WPC effect in the active region of a numerical model it is only necessary to modulate c_o according to Equation (5.3 a) or (5.3 b). This simplicity is a result of choosing perturbed density as a conservative variable. In contrast, the previous numerical models [52, 53] that have chosen pressure as a conservative variable require an additional source term to produce the WPC effect. This difference is further illustrated by the derivation shown in Appendix C.

To integrate a WPC processes into the numerical model the coupling of the active region to the neighboring fluid is also considered. First, a large jump in acoustic impedance $\tau = \rho_o c_o$ exists across the interface with most fluids. Conveniently, the modified HLLC Riemann solver described in Subsection 3.2.4 ensures the proper transmission of acoustic waves across the interface. Second, the applicable governing equations differ between the active region (linear) and the neighboring fluid (nonlinear). Under these circumstances the problem arises of how to further modify the HLLC Riemann solver and how to apply the numerical flux. To address these issues a mixed solution is presented here that is consistent with the HLLC conservation integral, Equation (3.31). From the general HLLC expression for contact velocity, Equation (3.32 a), the terms corresponding to the linear elastic active region are linearized, while the terms corresponding to the nonlinear fluid maintain nonlinearity to the second order. The following equations give results of this procedure when the nonlinear fluid is respectively on the left and right of the interface:

$$u^*_{mixed} = \frac{\left[(\rho_{o,L} + \rho'_L)u_L(S_L - u_L) - p_L\right]_{nonlinear} - \left[\rho_R u_R S_R - p_R\right]_{linear}}{\left[(\rho_{o,L} + \rho'_L)(S_L - u_L)\right]_{nonlinear} - \left[\rho_R S_R\right]_{linear}} \qquad (5.12\text{ a})$$

$$u^*_{mixed} = \frac{\left[\rho_{o,L} u_L S_L - p_L\right]_{linear} - \left[(\rho_{o,R} + \rho'_R) u_R (S_R - u_R) - p_R\right]_{nonlinear}}{\left[\rho_{o,L} S_L\right]_{linear} - \left[(\rho_{o,R} + \rho'_R)(S_R - u_R)\right]_{nonlinear}} \qquad (5.12\ b)$$

In Equations (5.12) values for p are solved using the linear and nonlinear relations given in Chapter 1, and ρ' is solved using Equation (3.33). Numerical fluxes are then applied according to the respective definitions of $\boldsymbol{F}_{linear}$ and $\boldsymbol{F}_{nonlinear}$. For sufficiently weak waves this modified HLLC solver reduces to the linear acoustic solution, while increasing wave strength causes the solution to deviate.

5.4 Validation of the Linear Acoustic WPC Model

The test case used for validation of the linear acoustic WPC model is identical to the one shown in Figure 4 of Merlen et al. [53]. For this test case an active region is bounded by two passive mediums of differing acoustic impedance as shown in Figure 23. The following equations define the initial conditions for the numerical model as three wavelengths of amplitude, A_o = 1000 Pa in the leftmost portion of the active region:

$$P_o = -A_o \sin\left(k_\omega (x - x_l)\right), \qquad v_o = \frac{P_o}{\rho_o c_o}, \qquad x_l < x < (x_l + 3\lambda) \qquad (5.13)$$

Sound speed modulation in the active region begins at the start of the calculation, t = 0, and has a duration of 19 μs, which corresponds to the physical pumping duration in current devices. All parameters used for the analytical and numerical models are given in Table 11, for additional information refer to [53].

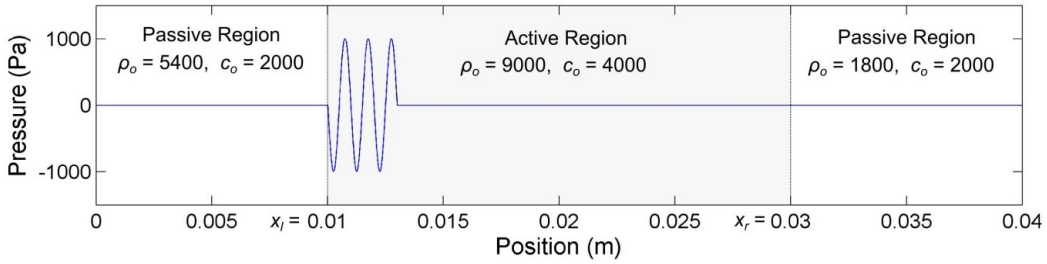

Figure 23: Initial wave profile for WPC validation calculation.

The numerical model uses the WENO-Z5 spatial reconstruction scheme in conjunction with RK4 time integration and a CFL number of 0.8. Calculations were performed with grid resolutions of 12.5, 25, 50, 100, and 200 computational cells per wavelength in the active region.

Table 11: WPC verification calculation parameters.

Parameter	*Value*	*Definition*
m	0.10	Sound speed modulation depth
Ω	$1.6\ \pi\ 10^7$ (rad/s)	Modulation frequency
$\omega = \Omega/2$	$8.0\ \pi\ 10^6$ (rad/s)	Wave frequency (rad/s)
$k_\Omega = \Omega/c_o$	$4000\ \pi$	Pumping frequency wave number
$k_\omega = \omega/c_o$	$2000\ \pi$	Standard wave number
t_{max}	19 μs	Active region modulation duration
$k_\Omega L$	80π	Normalized active region length
L	2.0 cm	Length of active region
c_o	4000 (m/s)	Active region natural sound speed
ρ_o	9000 (kg/m^3)	Active region density
τ_l	0.3	Left acoustic impedance ratio
$c_{o,l}$	2000 (m/s)	Sound speed, left region
ρ_l	5400 (kg/m^3)	Density, left region
τ_r	0.1	Right acoustic impedance ratio
$c_{o,r}$	2000 (m/s)	Sound speed, right region
ρ_r	1800 (kg/m^3)	Density, right region

As previously noted the amplitude term, A, in the analytical solution does not have a known value for arbitrary initial conditions; therefore, to set the reference amplitude, a value was selected to match the maximum amplitude in the numerical solution at the 200 cells per wave resolution level.

Figure 24 plots the pressure profile at 19 μs (end of the pumping duration) as calculated using the analytical solution and the numerical model with 25 cells per wavelength resolution. Agreement between the two solutions appears to be quite good, and this agreement improves with higher resolutions. Careful inspection of Figure 25, which plots the L_1 norms of the deviation between the resonant analytical solution and the transient numerical solution, shows the numerical solution is fully resonant after 18 μs. This confirms the viability of using the 19 μs time profile as a basis for comparison to the analytical solution.

Figure 26 plots the stress (pressure) at the left boundary of the active region and provides a visual measure for the exponential growth of the conjugate wave. Specifically, Figure 26 plots the analytical solution (Equation 5.6) against the numerical result obtained using 25 cells per wavelength resolution. Comparing these two stress histories it is evident very good agreement is achieved after the initial transient is overtaken by the resonant solution. Although not shown, the

agreement obtained at higher resolutions is consistent with the plotted data.

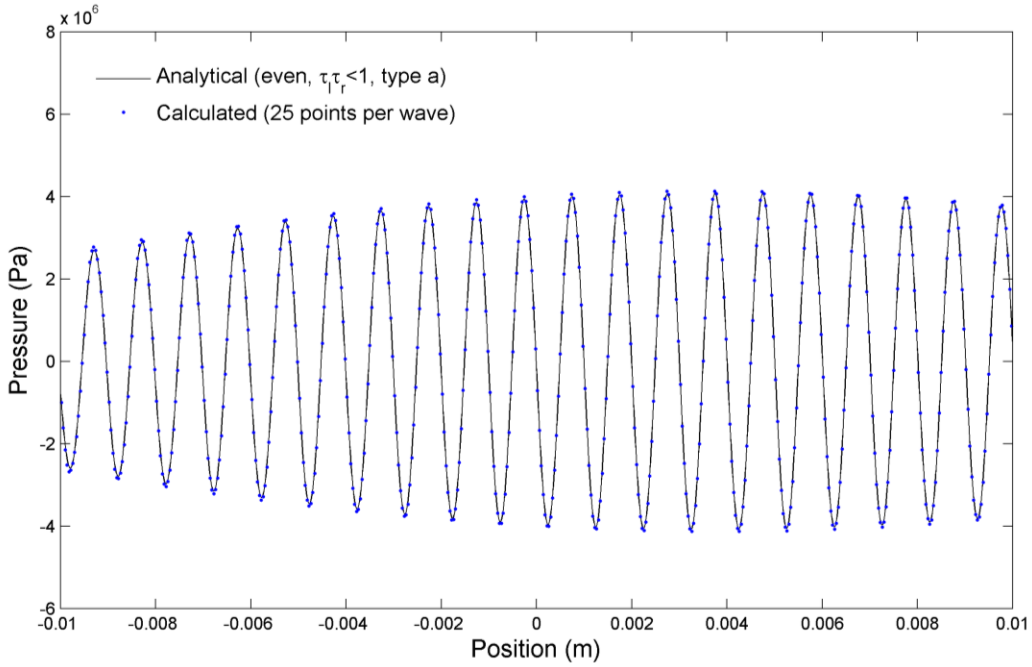

Figure 24: Numerical and analytical wave profiles in the WPC active region at t = 19 µs.

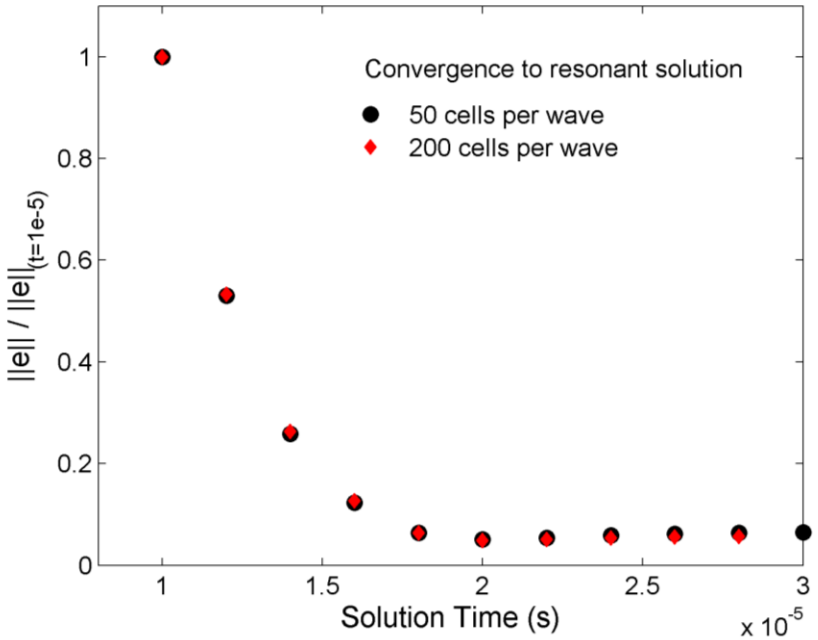

Figure 25: Numerical convergence to the analytical resonant WPC solution. Decreasing error is related to decreasing magnitude of transient waves originating from initial conditions in the numerical model.

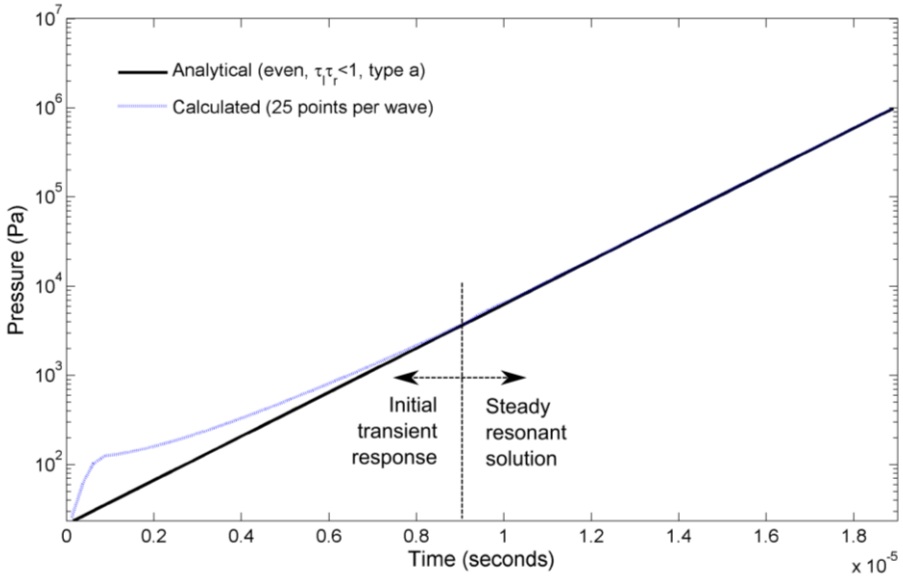

Figure 26: Maximum stress (pressure) at the left boundary of the WPC active region.

More formal error analysis is given in Table 12 and Table 13, where L_1 error norms are shown relative to the analytical solution and relative to the 200 cell per wave numerical solution. Additionally, Figure 27 plots the L_1 norms to illustrate the solution convergence behavior, from which several notable results are evident. First, the numerical solution does not continue to converge appreciably to the analytical solution when resolution is increased beyond 50 cells per wave. As shown in Table 13, this behavior is not consistent with the purely numerical results, where the solution continues to converge at a reasonably similar rate up to the 200 cell per wave reference. There are several possible causes for this discrepancy. First, there are slight underlying differences between the governing equation set used for the analytical solution and developed numerical model. This if further illustrated in the derivation shown in Appendix C. Second, in the analytical solutions used here the O(m) term, $mf(x,t)$, was neglected. Finally, it is possible that improper intermediate solution times from the Rung-Kutta scheme where used when setting $c_o(t)$. The susceptibility of Rung-Kutta type schemes to produce error with time dependent boundaries and source terms is a well known issue [1].

It is worthwhile to note that the error magnitude – as opposed to the order of convergence – is quite good. When normalized by the average wave amplitude,

the L_1 error at the 25 cell resolution is 0.025, while the normalized L_1 error at the 50 and 100 cell resolutions are less than 0.01. While addressing issues identified as potential sources of discrepancy between the numerical and analytical solutions may improve this accuracy somewhat, the current results indicate that the numerical model is capable of reproducing the WPC effect and can be used for investigations into the fundamental behavior of the phenomena.

Table 12: Solution convergence to analytical values in the WPC active region. Resolution in cells per wave, error norms calculated using fluid pressure.

Resolution	Δx (mm)	L_1 / (1.0E+05)	L_1 / $L_{1,max}$	L_1/σ_{rms}	R_1
12.5	8.0E-05	5.005	1.000	0.212	
25.0	4.0E-05	0.589	0.118	0.025	3.09
50.0	2.0E-05	0.205	0.041	0.009	1.52
100.0	1.0E-05	0.130	0.026	0.006	0.66
200.0	5.0E-06	0.121	0.024	0.005	0.10

Table 13: Solution convergence to numerical reference (Δx = 0.5E-05) in the WPC active region. Resolution in cells per wave, error norms calculated using fluid pressure.

Resolution	Δx (mm)	L_1 / (1.0E+05)	L_1 / $L_{1,max}$	L_1/σ_{rms}	R_1
12.5	8.0E-05	2.879	1.000	0.122	
25.0	4.0E-05	0.334	0.116	0.014	3.11
50.0	2.0E-05	0.084	0.029	0.004	1.99
100.0	1.0E-05	0.015	0.005	0.001	2.47
200.0	5.0E-06				

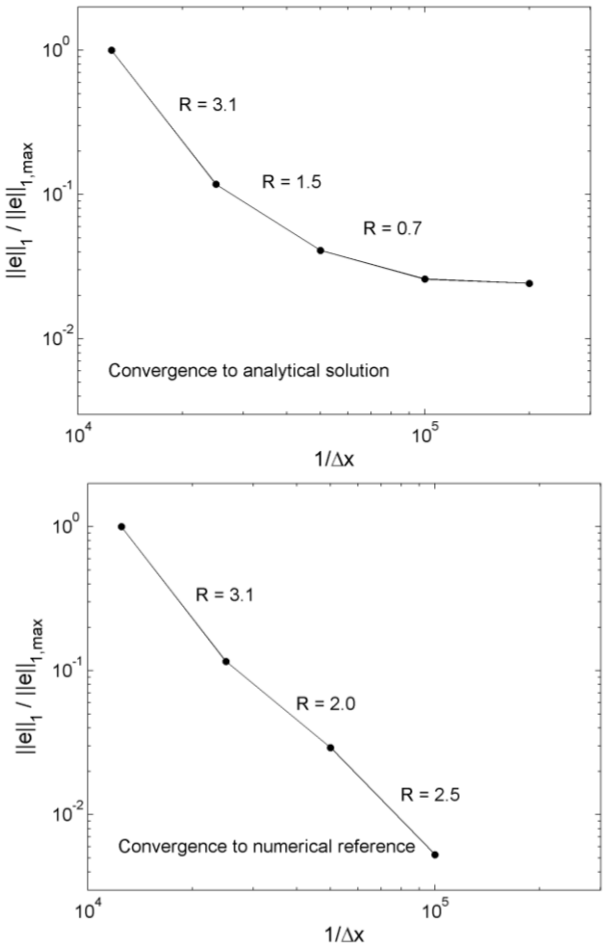

Figure 27: Solution convergence to analytical values in the WPC active region (top), and solution convergence to numerical reference (Δx = 0.5E-05) in the WPC active region (bottom). L_1 error norms calculated using fluid pressure.

5.5 Effects of Nonlinear Fluid Response in Acoustic WPC

Referring to the review of nonlinear effects in ultrasonic WPC provided in Section 1.4, it becomes evident that many of the applications of ultrasonic WPC are only sufficiently represented using a multi-dimensional numerical model. However, having now established the sufficient accuracy of the nonlinear wave propagation model and having verified the numerical implementation of the acoustic WPC model, some preliminary applications of the completed one-dimensional numerical model can be considered.

In previous works that have numerically investigated nonlinear ultrasonic WPC [12, 13, 14, 22, 59, 60] the conjugate beam is assumed to be a perfectly time-reversed and instantaneously amplified copy of incident beam. This assumption neglects the possible influences of nonlinearity on the fluid-conjugator interface,

and potential nonlinear effects in the conjugate beam related to the transient exponential growth of wave amplitudes. Using the developed numerical model, which accounts for the nonlinear coupling and the physical growth process, these two phenomena can numerically investigated.

5.5.1 Numerical Analysis of WPC Amplification Rates

In Section 5.2 it is shown that the WPC amplification rates has a constant exponential value. This growth rate is related to the conjugator properties, the pumping frequency, and the impedance match between the conjugator and the neighboring fluid. As a first approximation it seems entirely reasonable to neglect nonlinearity at the fluid-conjugator interface as the prominent nonlinear effects are cumulative over many wavelengths. Despite this, the sensitivity of the WPC process to factors such as domain length and defects in the conjugator is also quite high [77]. Thus the small influence of a local nonlinearity in the fluid response may be sufficient to alter overall behavior.

To investigate this possibility, the developed numerical model is used for scenarios corresponding to *even* and *odd* active region lengths as defined in Section 5.2. For all calculations an initial wave of 10 MHz is used with a pumping frequency of 20 MHz, and the active region length is either 20 (*even*) or 20.25 (*odd*) wavelengths. Physical properties of the fluid medium are set to match those of human fat tissue as reported in [64]: ρ_o = 915 kg/m^3, c_o = 1480 m/s, γ = 9.9. This is done to produce a greater nonlinear response, as the *B/A* parameter of fat tissue exceeds that of water. Acoustic properties of the active region are consistent with those from [52]: ρ_o = 9000 kg/m^3 and c_o = 4000 m/s. The numerical model uses WENO-Z5 spatial reconstruction and RK4 time integration with a CFL condition of 0.7. Spatial discretization is Δx = 8 μm for a resolution of 50 cells per wavelength in the active region and 18.75 cells in the fluid domain. This discrepancy is due to the use of a constant Δx despite the higher sound speed in the active region. Initial conditions in the active region are identical to those given in Figure 23. Sound speed modulation depth is specified differently for the *even* and *odd* scenarios according to the super-critical thresholds given by Equation

(5.11). For all additional physical parameters refer to Table 14.

Table 14: Summary of parameters for nonlinear WPC amplification rate calculations.

Parameter	*Value*	*Definition*
m	0.04, 0.06	Sound speed modulation depth
Ω	$40.0\ \pi\ 10^6$ (rad/s)	Modulation frequency
$\omega = \Omega/2$	$20.0\ \pi\ 10^6$ (rad/s)	Wave frequency (rad/s)
t_{max}	25 μs	Active region modulation duration
$k_\Omega L$	80π, 81π	Normalized active region length
L	0.80, 0.81 cm	Length of active region
c_o	4000 (m/s)	Active region natural sound speed
ρ_o	9000 (kg/m^3)	Active region density
$\tau_{l,r}$	0.04166667	Left acoustic impedance ratio
$c_{o,l,r}$	1500 (m/s)	Sound speed, left region
$\rho_{o,l,r}$	1000 (kg/m^3)	Density, left region

Calculation results for the *even* and *odd* cases are given in Figure 28 and Figure 29 respectively. These plots give the maximum pressure in the fluid region at the active region boundary as a function of time. Thus they can be used to gauge the wave amplitude growth in the active region. From Figure 28 and Figure 29 it is evident that the presence of nonlinearity in the fluid does not appreciably influence the WPC active region response. Specifically, in the regime of physically realizable pressures, $|P| < 8$ MPa, differences between the linear and nonlinear response are nearly negligible. From the normalized values given in the lower plots of Figure 28 and Figure 29, it can be seen that for both the *even* and *odd* active region lengths a fluid pressure of 6 MPa is required to produce a 1% difference between the linear and nonlinear calculations. At later times during the WPC amplification the differences between linear and nonlinear results become more substantial. For these extremely high fluid pressures at the conjugator boundary the fluid nonlinearity appears to increase the amplification rates over the expected linear response. When considering reported conjugate beam focal pressures are approximately 8 MPa [14], and that the corresponding pressures at the transducer interface would be substantially lower, the assumption of a linear coupling appears to be entirely justifiable.

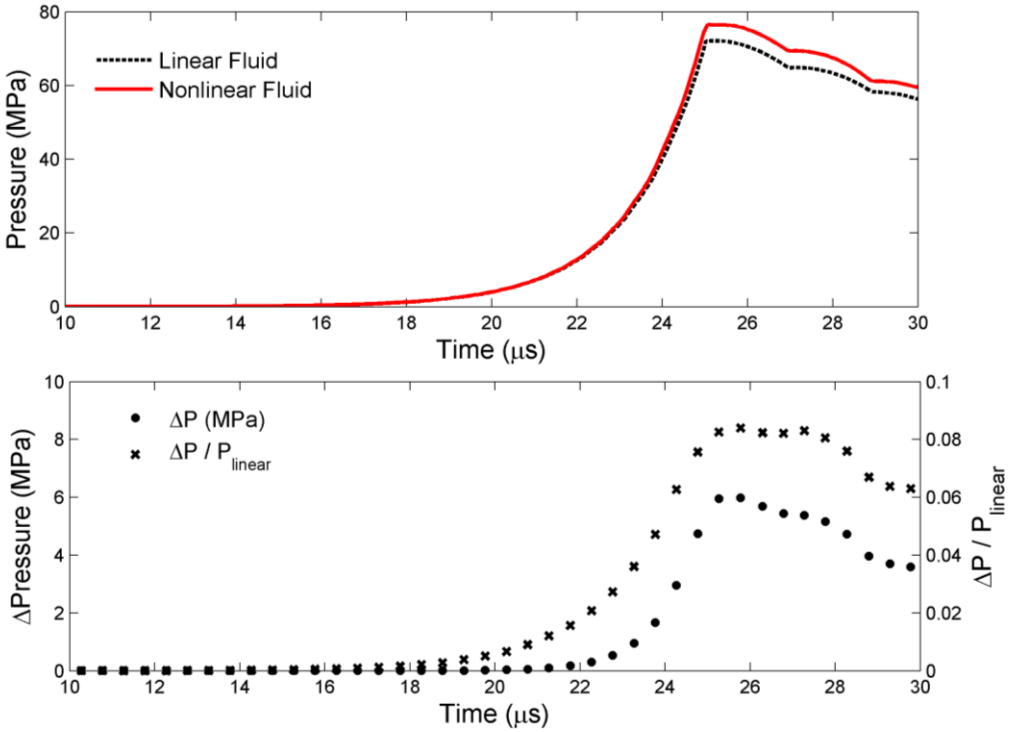

Figure 28: Pressure comparison of linear and nonlinear acoustic WPC, *even* length conjugator. Calculation with even active region length (kL = 80π), m = 0.04. Upper frame gives absolute values, lower frames gives relative values.

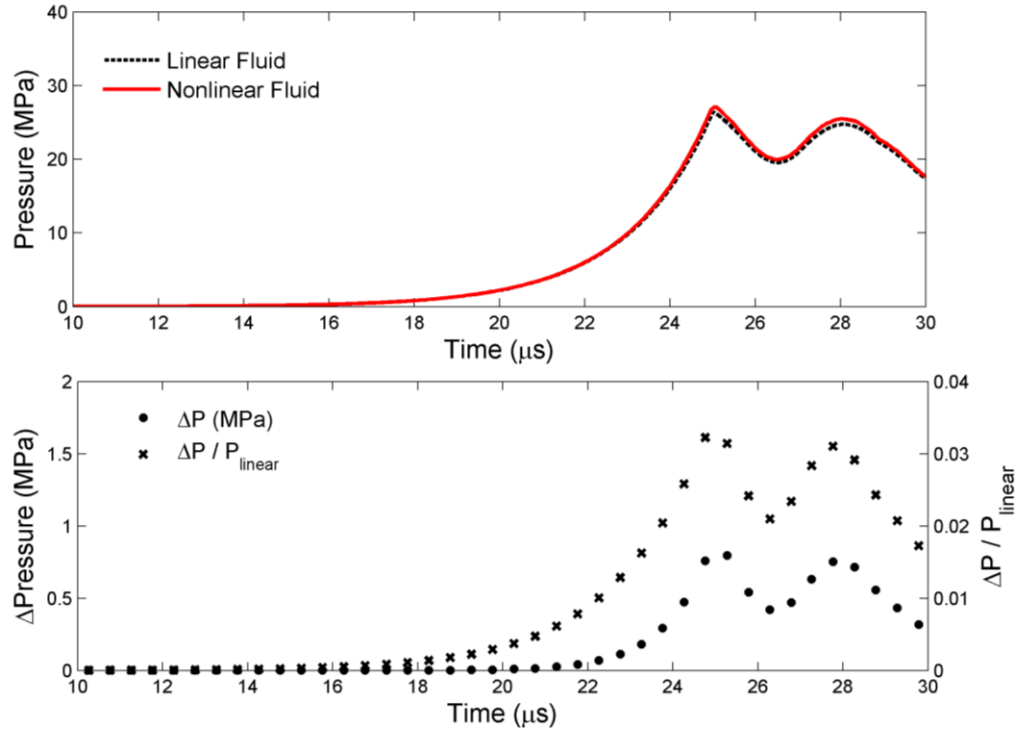

Figure 29: Pressure comparison of linear and nonlinear acoustic WPC, *odd* length conjugator. Calculation with odd active region length (kL = 81π), m = 0.06. Upper frame gives absolute values, lower frames gives relative values.

5.5.2 Numerical Analysis of Nonlinear Conjugate Sound Field

To evaluate possible nonlinear influences related to the exponential growth of conjugate wave amplitudes some additional calculations are performed of a physical scenario similar to that in Subsection 5.5.1. The only difference from the previously described setup is the use of full 2.0 cm active region length. Results from this calculation are compared at the transducer surface to a location 7 mm (approx. 50 wavelengths) downstream in the conjugate beam. Figure 30 plots these pressure histories with the surface gage given in the upper plot and the downstream gauge in the lower plot. To provide a benchmark result each frame also contains results from an equivalent calculation conducted using only the linear governing equations.

As expected the nonlinear fluid response at the transducer surface does not deviate significantly from the linear response for the pressure range considered ($|P| < 8$ MPa). When examining fluid pressure further downstream, deviation from the linear acoustic solution becomes visible for $|P| > 1.5$ MPa. The most evident result is the reduction in fluid pressure and a corresponding reduction in the conjugate wave amplitude growth. This reduction in peak pressure is a result of shockwave formation and shockwave related dissipation in the conjugate beam. This inability to produce equivalent increases in downstream pressure is consistent with a phenomenon known as acoustic saturation, and certainly warrants further investigation when the present numerical model is extended to multiple spatial dimensions.

Another interesting effect evident from Figure 30 is the non-symmetric nature of the pressure history. Specifically, the peak positive pressure values begin to exceed the peak negative pressure values. This results in a net positive pressure phase that exceeds the negative pressure phase. Asymmetrical waveforms are an expected result in focused nonlinear ultrasound beams but their occurrence is related to diffraction effects in the beam [14]. In the current simulation of a nonlinear plane wave, diffraction effects are not possible, so another explanation for the asymmetry must exist. By considering the continuous growth of the

conjugate wave amplitude it becomes evident that the increasing strength of each subsequent shock produces a corresponding increase in shock velocity. As the faster travelling shocks overtake the preceding waves the observed asymmetrical wave pattern is produced. This result has potential ramifications for predicting increases in the mean radiation pressure in a nonlinear conjugate beam, and serves as an excellent starting point for future investigations with multi-dimensional simulations.

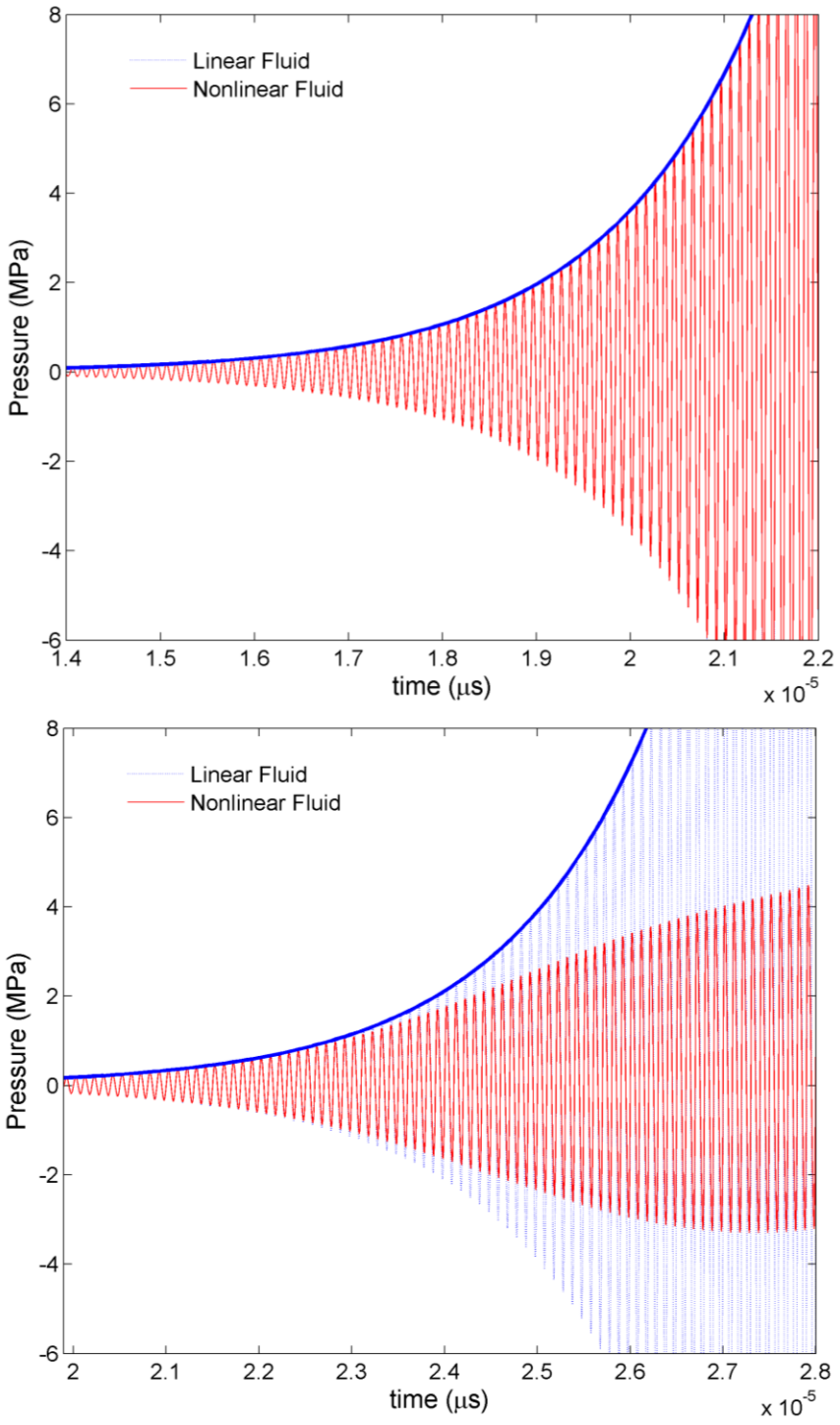

Figure 30: Acoustic saturation in acoustic WPC beams. Pressure history comparison is between gauges located at the WPC active region surface (upper) and located 50 wave lengths away (lower).

6 Summary and Conclusions

In this thesis the numerical modeling of nonlinear acoustic phenomena and ultrasonic Wave Phase Conjugation (WPC) are thoroughly investigated in the context of biomedical ultrasound applications. The primary objective of the current work is to develop a numerical model that can accurately represent the physical WPC process as described in Merlen et al. [53], and that can model the propagation of nonlinear waves including shockwave formation. In this regard, the primary objective of the current work is substantially completed.

The literature review presented in Sections 1.1, 1.2, 1.3, and 1.4 provides a cohesive reference for future works related to the simulation of high amplitude ultrasound beams produced by magnetostrictive WPC devices. Most importantly, the potential applications of this technology are discussed and a comprehensive summary of current experimental and numerical works on this topic is given.

The governing equations for the numerical model are developed in Chapter 2 and in Appendix A. These governing equations are consistent with well established second order wave equations – such as Kuznetsov's equation and the KZK equation – that are commonly used in the study of nonlinear acoustics. In Chapter 3 the numerical scheme that is applied to the governing equations is described in detail. The selected scheme uses high order Weighted Essentially Non-Oscillatory (WENO) techniques based on their history of application to nonlinear fluid phenomena. Presented in Chapter 3 is novel spectral analysis of the WENO schemes. This analysis shows that the resolution required with current WENO techniques is between six and eight points per wave when considering linear wave propagation. This analysis also shows that when modeling nonlinear wave propagation with a fundamental resolution of 25 points per wave, there is an underlying limit of four harmonics that can be represented.

In Chapter 4 a series of nonlinear plane wave calculations are presented to identify the functional limit of WENO schemes when applied to high amplitude ultrasonic wave propagation. From this calculation series, the seven cell stencil (r = 4) formulation using classic smoothness measure from Jiang and Shu [36]

(WENO-S7) is identified as most consistently producing accurate numerical results. When higher levels of resolution are used the five cell stencil (r = 3) formulation using current smoothness measures from Borges et al. [9] (WENO-Z5) is also shown to produce highly accurate results. With the WENO-S7 scheme a resolution of 25 cells per wavelength is sufficient when nonlinear distortions accumulate over distances of up to 100 wavelengths. In practical application this length scale is relevant to the focal length of an incident or conjugate ultrasound beam. Outside the focal region wave amplitudes are typically low and the wave propagates linearly, for which the WENO scheme is capable of accurate propagation over many hundreds of wavelengths.

Most importantly, the developed numerical model has successfully integrated a physical representation of magnetostrictive WPC within the nonlinear acoustic framework. In Chapter 5 this model was verified against known analytical solutions and has been shown to produce highly accurate results. Importantly, this development offers a novel combination of capabilities that can be used to conduct analysis on high amplitude wave effects in ultrasonic WPC. In Chapter 5 the model is applied to investigate the influence of fluid nonlinearity in WPC amplifications rates. The calculation results show the amplification rate is not sensitive to nonlinear acoustic response at the transducer surface. One additional calculation including the conjugate wave field is also presented in Chapter 5. Results from this calculation show interesting asymmetrical waveform distortion, which provides motivation for future numerical studies using a multi-dimensional model.

Based on the current findings it is recommended to continue development of the presently one-dimensional numerical model. Most importantly, the model should be developed for application to practical problems requiring two and three spatial dimensions. When adding this capability it is further recommended to consider use of the hybrid numerical scheme [67] that contains implicit compact methods for superior wave propagation capabilities and WENO methods for the accommodation of acoustic shock waves. Finally, it is recommended to incorporate a model for realistic acoustic attenuation processes, such as the one

described in [45]. These developments would overcome the main limitations of the current study and would allow for application of the model to a broader range of nonlinear acoustic problems occurring in biological tissues.

References

1 Abarbanel, S., Gottlieb, D., Carpenter, M. H. (1996). On the Removal of Boundary Errors Caused by Runge--Kutta Integration of Nonlinear Partial Differential Equations. *SIAM Journal on Scientific Computing*, 17(3), 777-782.

2 Atchley, A. A., Frizzell, L. A., Apfel, R. E., Holland, C. K., Madanshetty, S., Roy, R. A. (1988). Thresholds for cavitation produced in water by pulsed ultrasound. *Ultrasonics*, 26(5), 280-285.

3 Blackstock, D. T. (1966). Connection between the Fay and Fubini Solutions for Plane Sound Waves of Finite Amplitude. *The Journal of the Acoustical Society of America*, 39(6), 1019-1026.

4 Blackstock, D. T., Hamilton, M. F., Pierce, A. D. (2008) Progressive Waves in Lossless and Lossy Fluids. In Hamilton, M. F., Blackstock, D.T. (eds.), *Nonlinear Acoustics*, Acoustical Society of America.

5 Balsara D. S., Shu, C. W. (2000). Monotonicity Preserving Weighted Essentially Non-oscillatory Schemes with Increasingly High Order of Accuracy. *Journal of Computational Physics*, 160(2), 405-452.

6 Batten, P., Clarke, N., Lambert, C., Causon, D. M. (1997). On the Choice of Wavespeeds for the HLLC Riemann Solver. *SIAM Journal on Scientific Computing*, 18(6), 1553-1570.

7 Beyer, R. T. (1960). Parameter of Nonlinearity in Fluids. *The Journal of the Acoustical Society of America*, 32(6), 719-721.

8 Beyer, R.T. (2008). The Parameter B/A. In Hamilton, M. F., Blackstock, D.T. (eds.), *Nonlinear Acoustics*, Acoustical Society of America.

9 Borges, R., Carmona, M., Costa, B., Don, W. S. (2008). An improved weighted essentially non-oscillatory scheme for hyperbolic conservation laws. *Journal of Computational Physics*, 227(6), 3191-3211.

10 Brysev, A., Krutyansky, L., Pernod, P., Preobrazhensky, V. (2000). Acoustic microscope based on magneto-elastic wave phase conjugator. *Applied Physics Letters*, 76(21), 3133-3135.

11 Brysev, A., Bunkin, F., Klopotov, R., Krutyanskii, L., Preobrazhenskii, V. (2001). Focusing of a nonlinear phase-conjugate ultrasonic wave transmitted through a phase-inhomogeneous layer. *JETP Letters*, 73(8), 389-392.

12 Brysev, A., Bunkin, F., Hamilton, M., Klopotov, R., Krutyanskii, L., Yan, K. (2003). Parametric phase conjugation for the second harmonic of a nonlinear ultrasonic beam. *Acoustical Physics*, 49(1), 19-23.

13 Brysev, A., Krutyansky, L., Pernod, P., Preobrazhensky, V. (2004). Nonlinear ultrasonic phase-conjugate beams and their application in ultrasonic imaging. *Acoustical Physics*, 50(6), 623-640.

14 Brysev, A. P., Bunkin, F. V., Krutyansky, L. M., Yan, X., Hamilton, M. F. (2005). Focused nonlinear phase-conjugate waves generated by a solid parametric amplifier. *Journal of the Acoustical Society of America*, 118(6), 3733-3736.

15 Carstensen E. L., Bacon D. R. (2008). Biomedical Applications. In Hamilton, M. F., Blackstock, D.T. (eds.), *Nonlinear Acoustics*, Acoustical Society of America.

16 Chao, J., Haselbacher, A., Balachandar, S. (2009). A massively parallel multi-block hybrid compact-WENO scheme for compressible flows. *Journal of Computational Physics*, 228(19), 7473-7491.

17 Christov, I., Jordan, P. M., Christov, C. I. (2006). Nonlinear acoustic propagation in homentropic perfect gases: A numerical study. *Physics Letters A*, 353(4), 273-280.

18 Clement, G. T. (2004). Perspectives in clinical uses of high-intensity focused ultrasound. *Ultrasonics*, 42(10), 1087-1093.

19 Cleveland, R. O., Hamilton, M. F., Blackstock, D. T. (1996). Time-domain modeling of finite-amplitude sound in relaxing fluids. *The Journal of the Acoustical Society of America*, 99(6), 3312-3318.

20 Cobbold, R. S. (2007). Nonlinear Ultrasonics. In *Foundations of Biomedical Ultrasound*, Oxford University Press.

21 Cockburn, B., Shu, C. W. (1994). Nonlinearly Stable Compact Schemes for Shock Calculations. *SIAM Journal on Numerical Analysis*, 31(3): 607-627.

22 Cunningham, K. B., Hamilton, M. F., Brysev, A. P., Krutyansky, L. M. (2001). Time-reversed sound beams of finite amplitude. *The Journal of the Acoustical Society of America*, 109(6), 2668-2674.

23 Duck, F.A. (2002). Nonlinear acoustics in diagnostic ultrasound. *Ultrasound in Medicine & Biology*, 28(1), 1-18.

24 Duck, F. (2010). Tissue non-linearity. *Proceedings of the Institution of Mechanical Engineers, Part H: Journal of Engineering in Medicine*, 224(2), 155-170.

25 Enflo, B. O., Hedberg, C. M. (2002). Nonlinear Waves with Zero and Vanishing Diffusion. In *Theory of Nonlinear Acoustics in Fluids*, Kluwer Academic Publishers.

26 Enflo, B. O., Hedberg, C. M. (2002). Physical theory of nonlinear acoustics. In *Theory of Nonlinear Acoustics in Fluids*, Kluwer Academic Publishers.

27 Fink M. (2008). Time-reversal acoustics. *Journal of Physics: Conference Series*, 118(1), 012001.

28 Fogarty, T. R., LeVeque, R. J. (1999). High-resolution finite-volume methods for acoustic waves in periodic and random media. *The Journal of the Acoustical Society of America*, 106(1), 17-28.

29 Ginter, S., Liebler, M., Steiger, E., Dreyer, T., Riedlinger, R. E. (2002). Full-wave modeling of therapeutic ultrasound: Nonlinear ultrasound propagation in ideal fluids. *The Journal of the Acoustical Society of America*, 111(5), 2049-2059.

30 Hamilton, M. F., Morfey, C. L. (2008). Model Equations. In Hamilton, M. F., Blackstock, D. T., *Nonlinear Acoustics* (eds.), Acoustical Society of America.

31 Harten, A., Lax, P. D., Leer, B. V. (1983). On Upstream Differencing and Godunov-Type Schemes for Hyperbolic Conservation Laws. *SIAM Review*, 25(1), 35-61.

32 Harten A., Engquist, B., Osher, S., Chakravarthy, S. R. (1997). Uniformly High Order Accurate Essentially Non-oscillatory Schemes, III. *Journal of Computational Physics*, 131(1), 3-47.

33 Henrick, A. K., Aslam, T. D., Powers, J. M. (2005). Mapped weighted essentially non-oscillatory schemes: Achieving optimal order near critical points. *Journal of Computational Physics*, 207(2), 542-567.

34 Herbert, E., Balibar, S., Caupin, F. (2006). Cavitation pressure in water. *Physical Review E*, 74(4), 041603.

35 Hu F.Q., Hussaini, M. Y., Manthey, J. L. (1996). Low-Dissipation and Low-Dispersion Runge-Kutta Schemes for Computational Acoustics. *Journal of Computational Physics*, 124(1), 177-191.

36 Jiang G. S., Shu C. W. (1996). Efficient Implementation of Weighted ENO Schemes. *Journal of Computational Physics*, 126(1), 202-228.

37 Kennedy, J. E., ter Haar, G. R., Cranston, D. (2003). High intensity focused ultrasound: surgery of the future? *The British Journal of Radiology*, 76(909), 590-599.

38 Kennedy, J. E. (2005). High-intensity focused ultrasound in the treatment of solid tumours. *Nature Reviews Cancer*, 5(4), 321-327.

39 Khelil, S. B., Merlen, A., Preobrazhensky, V., Pernod, P. (2001). Numerical simulation of acoustic wave phase conjugation in active media. *The Journal of the Acoustical Society of America*, 109(1), 75-83.

40 Kinsler, L. E., Frey, A. R., Coppens, A. B., Sanders, J. V. (2000). Radiation and Reception of Acoustic Waves. In *Fundamentals of Acoustics*, Wiley.

41 Krutyansky, L., Pernod, P., Brysev, A., Bunkin, F. V., Preobrazhensky, V. (2002). Supercritical parametric wave phase conjugation as an instrument for narrowband analysis in ultrasonic harmonic imaging. *Ultrasonics, Ferroelectrics and Frequency Control, IEEE Transactions*, 49(4), 409-414.

42 Kuznetsov, V. P. (1971). Equations of Nonlinear Acoustics. *Soviet Physics Acoustics*, 16, 467-470.

43 Laney, C. B. (1998). *Computational Gasdynamics*, Cambridge University Press.

44 Law, W. K., Frizzell, L. A., Dunn, F. (1985). Determination of the nonlinearity parameter B/A of biological media. *Ultrasound in Medicine & Biology*, 11(2), 307-318.

45 Liebler, M., Ginter, S., Dreyer, T., Riedlinger, R. E. (2004). Full wave modeling of therapeutic ultrasound: Efficient time-domain implementation of the frequency power-law attenuation. *The Journal of the Acoustical Society of America*, 116(5), 2742-2750.

46 Lele, S. K. (1992). Compact finite difference schemes with spectral-like resolution. *Journal of Computational Physics* 103(1), 16-42.

47 LeVeque, R. J. (1997). Wave Propagation Algorithms for Multidimensional Hyperbolic Systems. *Journal of Computational Physics* 131(2), 327-353.

48 Liu, X.D., Osher, S., Chan, T. (1994). Weighted Essentially Non-oscillatory Schemes. *Journal of Computational Physics*, 115(1), 200-212.

49 Lombard, B., Piraux, J. (2004). Numerical treatment of two-dimensional interfaces for acoustic and elastic waves. *Journal of Computational Physics*, 195(1), 90-116.

50 Makarov, S., Ochmann, M. (1997). Nonlinear and Thermoviscous Phenomena in Acoustics, Part II. *Acta Acustica united with Acustica*, 83(2), 197-222.

51 Matar, O. B., Preobrazhensky, V., Pernod, P. (2005). Two-dimensional axisymmetric numerical simulation of supercritical phase conjugation of ultrasound in active solid media. *The Journal of the Acoustical Society of America*, 118(5), 2880-2890.

52 Merlen, A., Zhang, Q. (2006). Theory and simulation of wave phase conjugation. *Ultrasonics*, 44(1), e1475-e1478.

53 Merlen A., Zhang, Q., Voinovich, P., Timofeev, E. (2009). Duality of the supercritical solutions in magnetoacoustic wave phase conjugation. *Wave Motion*, 46(4), 255-268.

54 Nitta, N., Shiina, T. (2005). Breast Tissue Assessments Based on High Order Mechanical Properties. In E. Ueno, T. Shiina, M. Kubota, K. Sawai (Eds.), *Research and Development in Breast Ultrasound*, 50-54, Springer.

55 Piraux, J., Lombard, B. (2001). A New Interface Method for Hyperbolic Problems with Discontinuous Coefficients: One-Dimensional Acoustic Example. *Journal of Computational Physics*, 168(1), 227-248.

56 Prieur, F., Holm, S. (2011). Nonlinear acoustic wave equations with fractional loss operators. *Journal of the Acoustical Society of America*, 130(3): 1125-1132.

57 Pirozzoli, S. (2002). Conservative Hybrid Compact-WENO Schemes for Shock-Turbulence Interaction. *Journal of Computational Physics*, 178(1), 81-117.

58 Pirozzoli, S. (2006). On the spectral properties of shock-capturing schemes. *Journal of Computational Physics*, 219(2), 489-497.

59 Preobrazhenskii, V. L. (2006). Parametrically phase-conjugate waves: applications in nonlinear acoustic imaging and diagnostics. *Physics-Uspekhi*, 49(1), 98.

60 Preobrazhenskii, S. V., V. L. Preobrazhenskiĭ, Pernod, P., Bou Matar, O. (2008). Testing for inhomogeneity of the nonlinear parameter in an acoustic medium by ultrasonic phase conjugation. *Acoustical Physics*, 54(1), 15-19.

61 Pylnov, Y., P. Pernod, Preobrazhensky, V. (2001). Acoustic imaging by second harmonic of phase-conjugate wave in inhomogeneous medium. Applied Physics Letters, 78(4), 553-555.

62 Ren, Y. X., Liu, M. E., Zhang, H. (2003). A characteristic-wise hybrid compact-WENO scheme for solving hyperbolic conservation laws. *Journal of Computational Physics*, 192(2), 365-386.

63 Roe, P. L. (1981). Approximate Riemann solvers, parameter vectors, and difference schemes. *Journal of Computational Physics*, 43(2), 357-372.

64 Sehgal, C. M., Bahn, R. C., Greenleaf, J. F. (1984). Measurement of the acoustic nonlinearity parameter B/A in human tissues by a thermodynamic method. *The Journal of the Acoustical Society of America*, 76(4), 1023-1029.

65 Shen, Y., Yang, G. (2006). Hybrid finite compact-WENO schemes for shock calculation. *International Journal for Numerical Methods in Fluids* 53(4), 531-560.

66 Shen, Y., Zha, G., Gables, C. (2010). Improved Seventh-Order WENO Scheme. Paper presented at the *48th AIAA Aerospace Sciences Meeting Including the New Horizons Forum and Aerospace Exposition*, Orlando, Florida.

67 Shen, Y., Zha, G. (2011). Generalized finite compact difference scheme for shock/complex flowfield interaction. *Journal of Computational Physics* 230(12), 4419-4436.

68 Shi, J., Hu, C., Shu, C.-W. (2002). A Technique of Treating Negative Weights in WENO Schemes. *Journal of Computational Physics*, 175(1), 108-127.

69 Shu, C. W., Osher, S. (1988). Efficient implementation of essentially non-oscillatory shock-capturing schemes. *Journal of Computational Physics*, 77(2), 439-471.

70 Shu C. W., Cockburn, B., Johnson, C., Tadmor, E. (1998). Essentially non-oscillatory and weighted essentially non-oscillatory schemes for hyperbolic conservation laws. *Lecture Notes in Mathematics*, 1697, 325-432.

71 Shu, C. W., Osher, S. (1989). Efficient implementation of essentially non-oscillatory shock-capturing schemes, II. *Journal of Computational Physics*, 83(1), 32-78.

72 Taraldsen, G. (2001). A generalized Westervelt equation for nonlinear medical ultrasound. *The Journal of the Acoustical Society of America* 109(4), 1329-1333.

73 Tanter, Thomas, J.-L., Coulouvrat, F., Fink, M. (2000). Acoustic time reversal experiments in nonlinear regime. *AIP Conference Proceedings*, 524(1), 137-140.

74 Titarev, V.A., Toro, E. F. (2004). Finite-volume WENO schemes for three-dimensional conservation laws. *Journal of Computational Physics* 201(1), 238-260.

75 Toro, E.F., Spruce, M., Speares, W. (1994). Restoration of the contact surface in the HLL-Riemann solver. *Shock Waves*, 4(1), 25-34.

76 Voinovich, P. Merlen, A. (2005). Two-dimensional numerical simulation of acoustic wave phase conjugation in magnetostrictive elastic media. *The Journal of the Acoustical Society of America*, 118(6), 3491-3498.

77 Voinovich, P. (2010). On the gain sensitivity of reversed acoustic signal at parametric resonance conditions to small variations in wavelength. *Technical Physics Letters*, 36(5), 420-421.

78 Walsh, T., Torres, M. (2007). Finite element methods for nonlinear acoustics in fluids. *Journal of Computational Acoustics*, 15(03), 353-375.

79 White, F. M. (2003). *Fluid Mechanics, Fifth Edition*, McGraw Hill.

80 Zabbolotskaya, E. A, Khokhlov, R. V. (1969). “Quasi-Plane Waves in the Nonlinear Acoustics of Confined Beams”. *Soviet Physics Acoustics*, 15, 35-40.

Appendix A: Derivation of the Nonlinear Acoustic Equations

Consider an arbitrary volume, *V*, bounded by a control surface, *S*, where at any point on the surface the normal direction can be defined by the unit vector, $\vec{n}$. Then the conservation of mass and momentum equations are:

$$\frac{\partial}{\partial t}\oint_V \rho dV = -\oint_S \rho\vec{v}\cdot\vec{n}dS \qquad \text{A1.1}$$

$$\frac{\partial}{\partial t}\oint_V \rho\vec{v}dV = -\oint_S (\rho\vec{v}(\vec{v}\cdot\vec{n}) + p\vec{n})dS \qquad \text{A1.2}$$

where t is the time variable, ρ is the fluid density, $\vec{v}$ is the Cartesian velocity vector, and p is the fluid pressure. The purpose of this appendix is to translate these fundamental equations into conservative form second order wave equations.

Conservation of Mass

From $\rho = \rho' + \rho_o$, the conservation of mass equation can be readily simplified by removing the ρ_o term from the left hand side differential term to obtain:

$$\frac{\partial}{\partial t}\oint_V \rho' dV = -\oint_S (\rho_o + \rho')\vec{v}\cdot\vec{n}dS \qquad \text{A1.3}$$

which is the conservative integral form equation for the acoustic perturbed density. As will become evident in subsequent stages of this derivation it is also convenient to have the differential form of the mass conservation equation available. The divergence theorem is applied to the surface integral to obtain:

$$\oint_S (\rho_o + \rho')\vec{v}\cdot\vec{n}\,dS = \oint_V \nabla\cdot(\rho_o + \rho')\vec{v}\,dV \qquad \text{A1.4}$$

which gives:

$$\frac{\partial}{\partial t}\oint_V \rho' dV = -\oint_V \nabla\cdot(\rho_o + \rho')\vec{v}\,dV \qquad \text{A1.5}$$

As the volume integral equality must be true for any arbitrary space the differential operators must also be true throughout the domain; therefore:

$$\frac{\partial \rho'}{\partial t} = -\nabla \cdot (\rho_o + \rho')\vec{v} \qquad \text{A1.6}$$

gives the conservative differential form of the acoustic density equation.

Conservation of Momentum

For generality the conservation of momentum equations are presented in vector notation. The basic procedure of this derivation is to first expand all differential operators to include only individual variables of ρ, p, or $\vec{v}$. From here it will be shown that many of these expanded terms cancel, leaving a relatively simple conservative form equation stated in acoustic variables.

First consider the expansion of variables on the left hand side (LHS) of the momentum integral equation:

$$\begin{aligned} LHS &= \frac{\partial}{\partial t}\oint_V \rho\vec{v}\, dV \\ &= \oint_V \left(\rho\frac{\partial}{\partial t}\vec{v} + \vec{v}\frac{\partial}{\partial t}\rho\right) dV \end{aligned} \qquad \text{A1.7}$$

The time differential term containing ρ is replaced using the continuity equation to obtain:

$$\oint_V \left(\rho\frac{\partial}{\partial t}\vec{v} + \vec{v}\frac{\partial}{\partial t}\rho\right) dV = \oint_V \rho\frac{\partial}{\partial t}\vec{v} - \vec{v}\nabla \cdot (\rho\vec{v})\, dV \qquad \text{A1.8}$$

Now, to illustrate simplification of the term, $\vec{v}\nabla \cdot (\rho\vec{v})$, consider the two-dimensional case, where:

$$\begin{aligned} \vec{v}\nabla \cdot (\rho\vec{v}) &= \vec{v}\left(\frac{\partial}{\partial x}(\rho v_x) + \frac{\partial}{\partial y}(\rho v_y)\right) \\ &= \vec{v}\left(\rho\frac{\partial}{\partial x}v_x + v_x\frac{\partial}{\partial x}\rho + \rho\frac{\partial}{\partial y}v_y + v_y\frac{\partial}{\partial y}\rho\right) \\ &= \rho\vec{v}\nabla \cdot \vec{v} + \vec{v}(\vec{v} \cdot \nabla\rho) \end{aligned} \qquad \text{A1.9}$$

With this operation the compete the expanded *LHS* is:

$$LHS = \frac{\partial}{\partial t}\oint_V \rho\vec{v}dV = \oint_V \rho\frac{\partial}{\partial t}\vec{v} - \vec{v}\rho\nabla\cdot\vec{v} - \vec{v}(\vec{v}\cdot\nabla\rho) \qquad \text{A1.10}$$

Now consider the expansion of variables on the right hand side (RHS) of the momentum integral equation:

$$RHS = -\oint_S (\rho\vec{v}(\vec{v}\cdot\vec{n}) + p\vec{n})dS \qquad \text{A1.11}$$

As will become evident the derivation is most readily completed by working with differential form equations. Applying divergence identities obtains:

$$\oint_S p\vec{n}dS = \oint_V \nabla p dV \qquad \text{A1.12}$$

and by considering each velocity component in the *RHS* vector equation as a scalar field, denoted as v_k, it the convective momentum term can be expanded as:

$$\begin{aligned}\oint_S \rho v_k(\vec{v}\cdot\vec{n})dS &= \oint_V (\rho v_k\nabla\cdot\vec{v} + \vec{v}\cdot\nabla\rho v_k)dV \\ &= \oint_V (\rho v_k\nabla\cdot\vec{v} + \vec{v}\cdot\rho\nabla v_k + \vec{v}\cdot v_k\nabla\rho)dV \\ &= \oint_V (\rho v_k\nabla\cdot\vec{v} + \rho\vec{v}\cdot\nabla v_k + v_k\vec{v}\cdot\nabla\rho)dV\end{aligned} \qquad \text{A1.13}$$

Expressed again in a vector representation this equation becomes:

$$\oint_S \rho\vec{v}(\vec{v}\cdot\vec{n})dS = \oint_V \left(\rho\vec{v}\nabla\cdot\vec{v} + \rho\vec{v}\cdot\nabla\vec{v} + \vec{v}(\vec{v}\cdot\nabla\rho)\right)dV \qquad \text{A1.14}$$

To summarize the expanded *RHS* of the momentum equation is:

$$RHS = -\oint_V (\rho\vec{v}\nabla\cdot\vec{v} + \rho\vec{v}\cdot\nabla\vec{v} + \vec{v}(\vec{v}\cdot\nabla\rho) + \nabla P)dV \qquad \text{A1.15}$$

Now consider combining the LHS and RHS terms of the momentum integral equation:

$$\oint_V \rho\frac{\partial}{\partial t}\vec{v} - \rho\vec{v}\nabla\cdot\vec{v} - \vec{v}(\vec{v}\cdot\nabla\rho)\,dV = -\oint_V (\rho\vec{v}\nabla\cdot\vec{v} + \rho\vec{v}\cdot\nabla\vec{v} + \vec{v}(\vec{v}\cdot\nabla\rho) + \nabla p)dV \quad \text{A1.16}$$

Noting that $\vec{v}\{\rho\nabla\cdot\vec{v}\}$ and $\rho\vec{v}\{\nabla\cdot\vec{v}\}$ are common to both sides and can be eliminated, the simplified momentum integral is:

$$\oint_V \rho\frac{\partial}{\partial t}\vec{v}\,dV = -\oint_V (\rho\vec{v}\cdot\nabla\vec{v} + \nabla p)\,dV \quad \text{A1.17}$$

In the above expression the acoustic variable of interest, $\vec{v}$, is not isolated. Removing the volume integrals that are common to both sides allows for normalizing by ρ^{-1} to provide:

$$\frac{\partial}{\partial t}\vec{v} = -\vec{v}\cdot\nabla\vec{v} - \frac{1}{\rho}\nabla p \quad \text{A1.18}$$

where $\partial\vec{v}/\partial t$ is now isolated, but additional manipulations are needed to achieve a conservative form. First consider the term, $\vec{u}\cdot\nabla\vec{u}$, which can be expressed as:

$$\vec{v}\cdot\nabla\vec{v} = \nabla\left(\frac{1}{2}U^2\right), \qquad U^2 = |\vec{v}|^2 \quad \text{A1.19}$$

This transformation is based on a common vector identity [79], and includes the assumption of an irrotational flow. It is this assumption and simplification that allow the momentum equation to reach a fully conservative form. For a two-dimensional flow field this condition is expressed as:

$$\frac{\partial v_x}{\partial y} = \frac{\partial v_y}{\partial x} \quad \text{A1.20}$$

Now consider $\rho^{-1}\nabla p$; the ρ^{-1} term is expanded using Taylor series and p' is represented using the 2nd order Tait-Kirkwood Equation of State:

$$\frac{1}{\rho} = \frac{1}{\rho_o + \rho'} = \frac{1}{\rho_o} - \frac{\rho'}{\rho_o^2} + O(\rho'^2) + \cdots \tag{A1.21}$$

$$p' = c_o^2 \rho' + c_o^2 \frac{\gamma - 1}{2\rho_o} \rho'^2 \tag{A1.22}$$

$$\frac{1}{\rho} \nabla p = \frac{1}{\rho_o} \left(1 - \frac{\rho'}{\rho_o}\right) \nabla \left(p_o + c_o^2 \rho' + c_o^2 \frac{\gamma - 1}{2\rho_o} \rho'^2\right) \tag{A1.23}$$

The constant, p_o, can be removed from the gradient operator, and the remaining terms are multiplied to obtain:

$$\begin{aligned} \frac{1}{\rho} \nabla p \quad &= \frac{1}{\rho_o} \left(1 - \frac{\rho'}{\rho_o}\right) \nabla \left(c_o^2 \rho' + c_o^2 \frac{\gamma - 1}{2\rho_o} \rho'^2\right) \\ &= \nabla \left(c_o^2 \frac{\rho'}{\rho_o} + c_o^2 \frac{\gamma - 1}{2} \frac{\rho'^2}{\rho_o^2}\right) - \frac{\rho'}{\rho_o} \nabla \left(c_o^2 \frac{\rho'}{\rho_o}\right) + O(\rho'^3) \end{aligned} \tag{A1.24}$$

and the two separate gradient terms can be combined by noting that:

$$\frac{\rho'}{\rho_o} \nabla \left(c_o^2 \frac{\rho'}{\rho_o}\right) = \frac{1}{2} c_o^2 \nabla \left(\frac{\rho'}{\rho_o}\right)^2 \tag{A1.25}$$

then the expression for the pressure gradient then becomes:

$$\frac{1}{\rho} \nabla P = \nabla \left(c_o^2 \frac{\rho'}{\rho_o} + c_o^2 \frac{\gamma - 2}{2} \left(\frac{\rho'}{\rho_o}\right)^2\right) \tag{A1.26}$$

The differential momentum equation can now be expressed in a fully conservative form as:

$$\frac{\partial}{\partial t} \vec{v} = -\nabla \left(\frac{1}{2} U^2 + c_o^2 \frac{\rho'}{\rho_o} + c_o^2 \frac{\gamma - 2}{2} \left(\frac{\rho'}{\rho_o}\right)^2\right) \tag{A1.27}$$

Integrating over the control volume, *V,* and by applying the divergence theorem to the *RHS*, the conservative form integral equation for acoustic fluid velocity is:

$$\frac{\partial}{\partial t} \oint_V \vec{v} \, dV = -\oint_S \frac{1}{2} U^2 + c_o^2 \frac{\rho'}{\rho_o} + c_o^2 \frac{\gamma - 2}{2} \left(\frac{\rho'}{\rho_o}\right)^2 dS \tag{A1.28}$$

Appendix B: One Dimensional Governing Equations

This appendix provides a concise summary of the simplified one-dimension governing equations. Throughout this appendix the variable definitions are consistent with those used in Chapter 2.

Governing Equations

$$\frac{\partial}{\partial t}\oint_V \boldsymbol{U} dV = -\oint_s \boldsymbol{F} dS \tag{A2.1a}$$

$$\boldsymbol{U} = \begin{bmatrix} \rho' \\ v_x \end{bmatrix} \tag{A2.1b}$$

$$\boldsymbol{F} = \begin{bmatrix} \rho_o v_x \\ c_o^2\left(\frac{\rho'}{\rho_o}\right) \end{bmatrix}_{linear} \tag{A2.1c}$$

$$\boldsymbol{F} = \begin{bmatrix} (\rho_o + \rho')v_x \\ \frac{1}{2}v_x^2 + c_o^2\left(\frac{\rho'}{\rho_o}\right) + c_o^2\frac{(\gamma-2)}{2}\left(\frac{\rho'}{\rho_o}\right)^2 \end{bmatrix}_{nonlinear} \tag{A2.1d}$$

Flux Jacobians

$$A_{i,j} = \frac{\partial F_i}{\partial U_j} \tag{A2.2a}$$

$$\boldsymbol{A} = \begin{bmatrix} 0 & \rho_o \\ \frac{c_o^2}{\rho_o} & 0 \end{bmatrix}_{linear} \tag{A2.2b}$$

$$\boldsymbol{A} = \begin{bmatrix} v_x & \rho_o + \rho' \\ \frac{c_o^2}{\rho_o}\left(1 + (\gamma - 2)\frac{\rho'}{\rho_o}\right) & v_x \end{bmatrix}_{nonlinear} \tag{A2.2c}$$

System Eigenvalues

<u>*Linear System*:</u> $\lambda^- = -c_o$, $\lambda^+ = c_o$ (A2.3a)

<u>*Nonlinear System*:</u> $\lambda^- = v_x - c^*$, $\lambda^+ = v_x + c^*$ (A2.3b)

$$c^* = c_o\sqrt{1 + (\gamma - 1)\frac{\rho'}{\rho_o} + (\gamma - 2)\left(\frac{\rho'}{\rho_o}\right)^2} \tag{A2.3c}$$

System Eigenvectors

$$\boldsymbol{L} = \begin{bmatrix} \boldsymbol{l}_{\lambda^-} \\ \boldsymbol{l}_{\lambda^+} \end{bmatrix} \tag{A2.4a}$$

$$\boldsymbol{L} = \frac{1}{2} \begin{bmatrix} 1 & -\dfrac{\rho_o}{c_o} \\ 1 & \dfrac{\rho_o}{c_o} \end{bmatrix}_{linear} \tag{A2.4b}$$

$$\boldsymbol{L} = \frac{1}{2} \begin{bmatrix} 1 & -\dfrac{\rho^{'} + \rho_o}{c^*} \\ 1 & \dfrac{\rho^{'} + \rho_o}{c^*} \end{bmatrix}_{nonlinear} \tag{A2.4c}$$

$$\boldsymbol{R} = \begin{bmatrix} \boldsymbol{r}_{\lambda^-} \\ \boldsymbol{r}_{\lambda^+} \end{bmatrix}^T \tag{A2.5a}$$

$$\boldsymbol{R} = \begin{bmatrix} 1 & 1 \\ -\dfrac{c_o}{\rho_o} & \dfrac{c_o}{\rho_o} \end{bmatrix}_{linear} \tag{A2.5b}$$

$$\boldsymbol{R} = \begin{bmatrix} 1 & 1 \\ \dfrac{-c^*}{\rho_o + \rho'} & \dfrac{c^*}{\rho_o + \rho'} \end{bmatrix}_{nonlinear} \tag{A2.5c}$$

Appendix C: Derivation of Model Equations for Acoustic WPC

To illustrate the underlying differences in between the governing equations of the analytical and numerical models the following derivation is presented In this derivation the governing linear acoustic fluid equations are used to obtain an equivalent set of elastodynamic equations. Starting from the linearized fluid equations:

$$\frac{\partial \rho'}{\partial t} + \rho_o \frac{\partial v}{\partial x} = 0 \qquad \text{A3.1}$$

$$\frac{\partial v}{\partial t} + \frac{c^2}{\rho_o} \frac{\partial \rho'}{\partial x} = 0 \qquad \text{A3.2}$$

the variable ρ' is changed to θ using the linear relations, $p' = c^2\rho'$, and the definition, $\theta = p'/\rho_o c$:

$$\frac{\partial}{\partial t}\left(\frac{1}{c}\frac{p'}{\rho_o c}\right) + \frac{\partial}{\partial x}(v) = 0$$

$$\frac{\partial}{\partial t}\left(\frac{1}{c}\theta\right) + \frac{\partial}{\partial x}(v) = 0 \qquad \text{A3.3}$$

and:

$$\frac{\partial v}{\partial t} + \frac{\partial}{\partial x}\left(c\frac{p'}{\rho_o c}\right) = 0$$

$$\frac{\partial v}{\partial t} + c\frac{\partial \theta}{\partial x} = 0 \qquad \text{A3.4}$$

Applying the chain rule to Equation (A5.3) gives:

$$\frac{1}{c}\frac{\partial \theta}{\partial t} + \theta\frac{\partial}{\partial t}\left(\frac{1}{c}\right) + \frac{\partial v}{\partial x} = 0$$

$$\frac{1}{c}\frac{\partial \theta}{\partial t} + \frac{-\theta}{c^2}\frac{\partial c}{\partial t} + \frac{\partial v}{\partial x} = 0$$

$$\frac{\partial \theta}{\partial t} + c\frac{\partial}{\partial x}(v) = \frac{\theta}{c}\frac{\partial c}{\partial t} \qquad \text{A3.5}$$

At this stage the modified fluid Equations (A5.4) and (A5.5) exactly match the elastodynamic governing equations (Equation (5.1) and (5.2) in Chapter 5) that the analytical solution is derived from. For this reason, small differences between the numerical results and analytical solution are thought to originate from an approximation that is used for the $\left(\frac{\theta}{c}\frac{\partial c}{\partial t}\right)$ term in the analytical solution. To illustrate this discrepancy the exact form of $\left(\frac{\theta}{c}\frac{\partial c}{\partial t}\right)$ can be expanded according from the exact expression for sound speed oscillation:

$$c = c_o\sqrt{1 + m\cos(\Omega t + \phi)}$$

$$\frac{\partial c}{\partial t} = \frac{\partial\left(c_o\sqrt{1 + m\cos(\Omega t + \phi)}\right)}{\partial(1 + m\cos(\Omega t + \phi))} \cdot \frac{\partial(1 + m\cos(\Omega t + \phi))}{\partial t}$$

$$\frac{\partial c}{\partial t} = \frac{c_o}{2\sqrt{1 + m\cos(\Omega t + \phi)}} \cdot (-m\Omega\sin(\Omega t + \phi))$$

and allowing $\phi = \pi$:

$$\frac{\theta}{c}\frac{\partial c}{\partial t} = \frac{\theta}{c}\frac{c_o^2}{2c}\, m\Omega\sin(\Omega t) \qquad \text{A3.6}$$

where c_o is the sound speed for the unperturbed state, and c is the magnetically perturbed sound speed. Now considering the governing equation for θ, the source term can be exactly represented as:

$$\frac{\partial\theta}{\partial t} + c\frac{\partial}{\partial x}(v) = \frac{\theta}{c}\frac{\partial c}{\partial t} = \left(\frac{c_o^2}{c^2}\right)m\frac{\Omega\theta}{2}\sin(\Omega t) \qquad \text{A3.7}$$

This equation exactly represents the WPC process when the sound speed modulation defined by Equation (5.3 a) is applied to the linear acoustic governing equations. Differing from this is Equation (5.4) that is used in the analytical solution, where it appears the approximation $(c_o/c)^2 \cong 1$ is used. It is this approximation that may contribute to differences between the analytical and numerical solutions, which persist even for very high numerical resolutions.